PROTEIN ADSORPTION TO POLYMER BLEND FILMS

By

BONNIE O. LEUNG, B.Sc., M.Sc.

A Thesis

Submitted to the School of Graduate Studies

in Partial Fulfillment of the Requirements

for the Degree of

Doctor of Philosophy

McMaster University

DOCTOR OF PHILOSOPHY (2010) McMaster University
(Chemistry and Chemical Biology) Hamilton, ON

TITLE: Protein Adsorption to Polymer Blend Films

AUTHOR: Bonnie O. Leung, B.Sc., M.Sc. (University of Calgary)

SUPERVISOR: Professor Adam P. Hitchcock

NUMBER OF PAGES: 158, xxviii

ABSTRACT

The first step following implantation of biomaterials is adsorption of proteins to the surface. Subsequent steps in the biological reaction to the implant depend on the details of the initial protein layer. Thus, characterization of the interactions of proteins with the surfaces of candidate biomaterials may be helpful in understanding and optimizing biocompatibility.

Spatially resolved near-edge X-ray absorption fine structure (NEXAFS) spectra obtained via an X-ray photoemission electron microscope (X-PEEM) is used to study the spatial distribution of adsorbed proteins on chemically heterogeneous surfaces. X-PEEM is surface sensitive and can probe the top 10 nm of the surface with a lateral spatial resolution of ~ 80 nm.

Polystyrene (PS) was blended with a variety of polymers including the biodegradable polylactide (PLA), biocompatible polyethylene oxide (PEO), and poly(methyl methacrylate)-b-polyacrylic acid (PMMA-PAA) which is negatively charged under neutral aqueous conditions. Human serum albumin (HSA) adsorption to these surfaces was examined with respect to surface rugosity and ionic strength (PS-PLA blends), protein repellency (PS-PEO blends), and electrostatic interactions (PS/PMMA-PAA blends).

It was found that X-PEEM has excellent capabilities for simultaneously interrogating both the adsorbed protein and surface of the polymeric films, obtaining both the topography and chemistry at the surface with high sensitivity.

ACKNOWLEDGEMENTS

I would like to express my sincerest thanks to my advisor, Prof. Adam Hitchcock, for giving me this project, and for encouraging me to propose creative and innovative systems for X-PEEM analysis. Thank you for your guidance, continual feedback and excellent suggestions. It has helped to make this project both successful and highly enjoyable.

My graduate experience would not have been the same without my group members: Ebi Najafi, Karen Lam, Adam Leontowich, Sam Kalira, Hua Jiang, Dr. Jian Wang, Dr. Zulima Martin, Dr. Daniel Hernandez-Cruz, and Dr. Glyn Cooper. Thank you for all your help and wonderful discussions.

I sincerely acknowledge Prof. John L. Brash, Prof. Harald Stöver, and Prof. Gillian Goward for serving on my committee, and for giving me fantastic advice and constructive comments over the last three years. Many thanks go to Prof. John L. Brash and Rena Cornelius for help with ^{125}I radiolabeling experiments; Dr. Steve Kornic for help with ^{1}H NMR experiments; and Dr. Andreas Scholl and Dr. Andrew Doran at the Advanced Light Source for help with X-PEEM.

To all the dearest friends that I met at McMaster (Jason, Jennilee, Erik, Dave, Lindsey, Heather and Mike), thank you for three years of unbelievable fun, interesting and creative scientific debates, and the huge amounts of laughing.

Finally, this work is dedicated to my sister, a constant foundation of encouragement and support.

TABLE OF CONTENTS

CHAPTER 1: GENERAL INTRODUCTION

CHAPTER 2: METHODS

CHAPTER 8: SUMMARY AND FUTURE WORK

LIST OF FIGURES

Chapter 1

Chapter 2

Chapter 3

Chapter 7

Chapter 8

LIST OF TABLES

Chapter 6

Chapter 7

LIST OF ABBREVIATIONS AND SYMBOLS

1-D	One dimensional
Å	Angstrom
A_0	Area exposed to beam
A.D.	Anno domini
AEY	Auger electron yield
AFM	Atomic force microscopy
ALS	Advanced Light Source
AOI	Area of interest
b	Block
BSA	Bovine serum albumin
c	Speed of light
°C	Degree Celcius
C-AFM	Contact mode atomic force microscopy
CCD	Charged Coupled Device
CH_2Cl_2	Dichloromethane
CLS	Canadian Light Source
cm	Centimetre
ConA	Concavalin A
δ	Polydispersity
Da	Dalton

DDI	Distilled deionized
DSC	Differential scanning calorimetry
E	Energy
ECM	Extracellular matrix
EELS	Electron energy loss spectroscopy
ESR	Electron spin resonance
eV	Electron volt
EXAFS	Extended X-ray absorption fine structure
ϕ	Volume fraction
Fg	Human fibrinogen
FDA	Food and Drug Administration
FTIR	Fourier transformed infrared
FWHM	Full width at half maximum
γ	Gamma
G	Grams
G	Gibbs free energy
G_{el}	Electrical Gibbs free energy
GeV	Giga electron volts
H	Enthalpy
h	Hour
HCl	Hydrochloric acid
HSA	Human Serum Albumin

Hz	Hertz
I_0	Incident intensity
I_1	Transmitted intensity
ID	Insertion device
IP	Ionization potential
IR	Infrared
K	Thousand
keV	kilo electron volt
kDa	Kilodalton
LcH	Lectin
linac	Linear accelerator
M	Million
M_0	Atomic number
MB	Megabite
MeV	Mega electron volts
mg	Miligram
min	Minute
mL	Mililitre
mM	Milimolar
MW	Molecular weight
η	Viscosity
NaOH	Sodium hydroxide

NC-AFM	Non-contact mode atomic force microscopy
NEXAFS	Near-edge X-ray absorption fine structure
nm	Nanometer
NSERC	National Sciences and Engineering Council of Canada
n_v	Volume density
OWLS	Optical wave guide lightmode spectroscopy
ρ	Atomic area density
PAA	Polyacrylic acid
PAS	Photoacoustic spectroscopy
PBS	Phosphate buffered saline
PEG	Polyethylene glycol
PEO	Polyethylene oxide
PET	Polyethylene terephthalate
PETA	Pentaerythritol triacrylate
PLA	Polylactide
PMMA	Poly(methyl methacrylate)
PMMA-PAA	poly(methyl methacrylate)-block-polyacrylic acid
PS	Polystyrene
PSA	Poly(sebacic anhydride)
PSf	Polysulfone
QCM	Quartz crystal microbalance
σ	interfacial tension

$\sigma_x(h\nu)$	X-ray absorption cross section
S	Entropy
SAM	Self assembled monolayer
SDS-PAGE	sodium dodecyl sulfate polyacrylamide gel electrophoresis
SEM	Scanning electron microscope
Si	Silicon
SPR	Surface plasmon resonance
SR	Synchrotron radiation
SPEM	Scanning photoemission microscopy
SPM	Scanning probe microscopy
STM	Scanning tunneling microscope
STXM	Scanning transmission X-ray microscope
SUB-6	RWWKIWVIRWWR-NH_2
SVD	Singular value decomposition
T	Temperature
TEM	Transmission electron microscope
TEY	Total electron yield
T_g	Glass transition temperature
TGA	Thermal gravimetric analysis
TM	Trade mark
TOF-SIMS	Time of flight secondary ion mass spectrometry
μ	Linear absorption coefficient

μm	Micron
UV	Ultraviolet
UV-VIS	Ultraviolet-visible
v	Velocity
WWII	World war II
XAS	X-ray absorption spectroscopy
X-PEEM	X-ray photoemission electron microscope
XPS	X-ray photoelectron spectroscopy
ζ	Zeta potential

CHAPTER 1: GENERAL INTRODUCTION

1.1 Introduction to Biomaterials

Biomaterials have been defined as any substance (synthetic or natural in origin) other than a drug, which can be used for any period of time, as a whole or as part of a system which treats, augments, or replaces any tissue, organ, or function of the body [1]. Each year, several hundred million medical devices are implanted in humans. However, biocompatibility remains a critical problem, since the body reacts similarly to all implanted materials by forming a 50-200 μm thick collagen bag around the implant, possibly interrupting the function of the device [2]. One hypothesis in the literature suggests that current biomaterials turn off the normal healing process [2]. Since the first step in wound healing occurs with the adsorption of a layer of proteins, understanding the mechanisms of protein adsorption may provide insight into biocompatibility and further enhancement of medical materials.

1.1.1 A Historical Perspective

Prior to 1950, the word “biomaterials” did not exist, yet rudimentary implants have been used since the dawn of civilization [3]. Perhaps the earliest biomaterial may have been the suture, used over 32,000 years ago [4]. The composition of early sutures ranged from the use of linen by early Egyptians, catgut by Europeans in the Middle Ages, to metallic sutures used by the early Greeks [4].

Dental implants have also been fabricated by early cultures. The Mayan used nacre from sea shells as teeth in 600 A.D. and a European corpse dated to 200 A.D. was found with an iron dental implant [5,6]. In both examples, the implants revealed proper bone integration, which is an impressive feat for these civilizations.

The wide-spread use of polymeric materials for medical purposes did not occur until after World War II, when plastics emerged as a commercially available material, rather than a wartime-restricted commodity [3]. Between the 1940s – 1960s some of the most important medical implants were fabricated including hip and knee prostheses, dental implants, the artificial kidney and heart, breast implants, vascular grafts, pacemakers and stents [3].

One of the most important implants developed in the 1940s was perhaps the intraocular lens by Sir Harold Ridley. Contrary to the viewpoint during that time period which believed that foreign objects would be rejected by the human body, Sir Ridley observed that plastic shards imbedded in the eyes of WWII aviators healed without adverse reaction [7]. This observation may possibly be the first documented finding of a biocompatible material [3]. The plastic shards were composed of poly(methyl methacrylate) (PMMA) and Sir Ridley began to use this polymer to fabricate intraocular lenses as replacements for cloudy or blinding cataracts. His first successful surgery was performed on November 29, 1949. Currently, over 9,000,000 lenses are implanted in humans each year [7].

Since the 1960s, a new biomaterials era has emerged, with biomaterials specifically created to control biological reactions [3]. This development parallels the

achievements of modern biology, since the principles of protein adsorption, healing and foreign-body reaction, cell attachment, growth factors and gene expression became well-understood [3]. Furthermore, novel ideas from materials science including phase separation, self assembled monolayers (SAMs) and surface sensitive techniques fuelled biomaterials development [3].

Some of the biomaterials developed include silicones, polyurethanes, Teflon™, biodegradable poly(lactic-glycolic acid), and hydroxyapatite and bioglass™ used for bone healing [3]. Perhaps one of the most important materials developed is the hydrogel (soft, water-swollen, clear elastic gels), which revolutionized the soft contact lens industry [3]. The most common hydrogel is poly(ethylene glycol) (PEG, or higher molecular weight poly(ethylene oxide) (PEO)) which is a polymer that widely reduces protein adsorption and increases biocompatibility. These materials provide the basis for future biomaterials development.

1.1.2 Biocompatibility and the Foreign body Response

Most biological reactions occur at interfaces, for example, protein interactions with cell membranes, extracellular matrix (ECM) interactions with the cell, or mineral interactions with bone [2]. It has been proposed that surfaces provide a greater accessibility for reactions with the low energy mobility barrier in the plane of the surface facilitating complex reactions [2]. For biomedical devices, the biological reactions that occur between a protein or cell with the implanted synthetic surface may give some indication of the biocompatibility of the implant.

However, the word “biocompatible” is currently poorly defined. Biocompatibility has been linked to a low immune response to implanted materials, or to specific properties of the materials themselves [2]. In 2003, Williams defined biocompatibility for long-term implants as “the ability of the device to perform its intended function, with the desired degree of incorporation in the host, without eliciting any undesirable local or systemic effects in that host [8].” One example of an undesirable effect is the foreign body response.

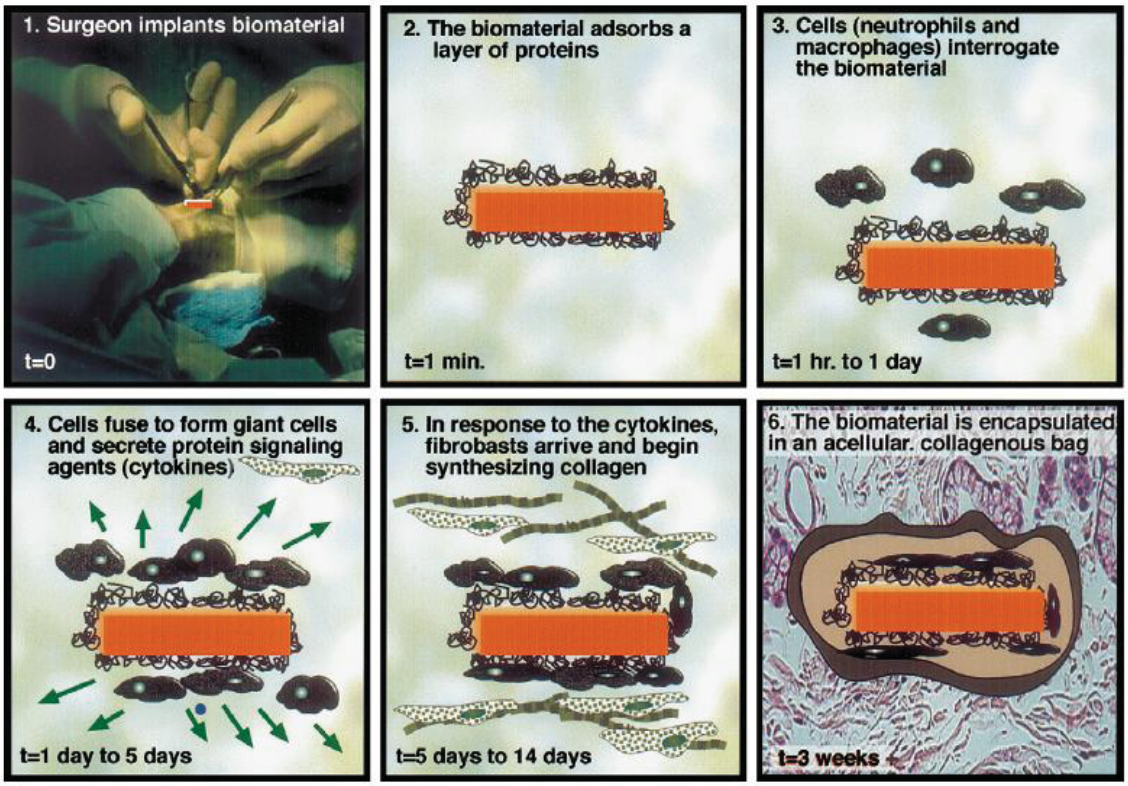

Figure 1.1: The foreign body response. 1. A biomaterial is implanted; 2. A layer of proteins immediately adsorb; 3. Neutrophils and macrophage try to ingest the biomaterial; 4. If the material is too large, the cells fuse and release signaling agents; 5. Fibroblasts arrive and begin synthesizing collagen; and 6. After 3 weeks, a collagen bag encapsulates the biomaterial [2]. Reprinted from Castner, D. T., Ratner, B. D. Surface Science, 500, 28-60, 2002, with permission from Elsevier.

After a biomaterial is implanted, a monolayer of proteins immediately adsorbs to the surface within a second (Figure 1.1) [2]. Protein adsorption is the initial event in the biological cascade, and cells such as neutrophils or macrophages that arrive at the surface within a day via diffusive, convective or active mechanisms see primarily adsorbed protein. Since cells can respond specifically to the adsorbed protein layer, it is possible that subsequent biological reactions to the implant may be controlled at this step.

Next, the cells interact with the proteins on the implant surface as they attempt to remove the invading material. If the surface is indigestible, the macrophages fuse together into giant cells and try to engulf the object. If the biomaterial is too large to ingest, chemical messengers (cytokines) signal to fibroblasts to start the synthesis of collagen, which is used to encase or wall-off the implant. One major disadvantage is that the presence of this collagen sac may impede the performance of the medical device [2].

1.1.3 Protein Adsorption to Surfaces

The shape and surface of a biomaterial can influence the foreign body response. Flat, smooth surfaces typically exhibit a foreign body response in which 1-2 layers of macrophages form around the implant while rough surfaces show a foreign body response in which a combination of macrophages and foreign-body giant cells are formed [3]. The basis of this difference in immune response arises from the adsorption of adhesion proteins to the surface which can interact with integrin receptors on cell surfaces. Thus, these adsorbed proteins play a key role in mediating the biological response seen upon implantation of a biomaterial.

When a biomaterial is implanted in vivo, protein adsorption to the surface of the biomaterial transforms the interface between the implant and body. For example, a water drop placed on a polystyrene Petri dish beads up since the surface of the dish is hydrophobic. However, if a drop of protein solution was added to the surface and then extensively rinsed, the water droplet completely spreads out over the adsorbed protein surface [3]. Similar to the water droplet, cells or other biocomponents that encounter the surface "see" mainly the adsorbed protein not the polystyrene dish [3]. Nonetheless, this is a very complex process since the composition of the adsorbed proteins varies depending on different surfaces [3].

Kinetically, all proteins adsorb rapidly to surfaces, and these proteins mediate the interaction of subsequent cells that may ultimately lead to an immune response. Thus, the intrinsic properties of both the surface and the adsorbed proteins determine the biological response. The relevant spatial scale involved in the adsorption chemistry studied in this thesis is difficult to specify precisely. It may be anywhere from several nm up to a hundred nm, depending on the system. In addition to variability of the porosity and rugosity of the polymer blend surface, the adsorption will depend on the size and shape of the protein, as well as the details of the electrical double layer in the solution above the polymer surface. The specific issue of possible dependence on the thickness of the polymer blend film could be examined by spin coating different thickness of polymer to the Si support and examining whether protein adsorption was affected by substrate thickness.

1.2 Driving Forces for Protein Adsorption

Both kinetics and thermodynamics may play roles in proten adsorption. Protein adsorption is thermodynamically allowed when $\Delta G_{ads} = \Delta H_{ads} - T\Delta S_{ads} < 0$, where G, H, S and T are the Gibbs free energy, enthalpy, entropy and temperature, respectively. According to Malmsten, there are four main driving forces for protein adsorption [9]:

1.2.1. Hydrophobic Interactions

The hydrophobic effect stems from the insolubility of hydrocarbons in water and is a basic driving force for the formation of lipids into bilayers [3]. In fact, hydrocarbons are less soluble in water due to the self-association of water [10].

The structure of ice obtained from X-ray and neutron diffraction is an approximate tetrahedral configuration with ~27.6 pm between each oxygen atom [10]. The nearest non-hydrogen bonded oxygen atom is ~45 pm away, resulting in a more porous structure which is the main reason why less dense ice floats on water [10].

At 4 °C, X-ray diffraction of liquid water reveals the average distance between oxygen atoms to be 28.2 pm and the oxygen atoms are even farther apart compared to ice, even though liquid water is denser [11]. The peak distribution function derived from X-ray diffraction shows 4.4 nearest neighbor molecules, which indicates short-range local order and an approximate tetrahedral structure. At separations above 80 pm, water molecules are randomized even at 4 °C [11].

Hydrophobic substances readily dissolve in many non polar solvents but only sparingly in water [10]. The hydrophobic effect stems from the strong attractive forces between water molecules which are disrupted when any solute is dissolved in water.

When an ionic or polar molecule is added to water, it can form strong bonds to water, lowering the ΔG, which compensates for the disruption of pure water. Thus, ionic and polar molecules easily dissolve [10]. However, non polar molecules do not have such compensation.

Protein molecules are highly inhomogeneous, with both polar and non-polar patches. For globular proteins in water, the non-polar residues are generally found in the interior of the protein and are shielded from contact with water [9]. However, some of the non-polar parts are exposed to water. For small proteins with a mass below 15000 Da, the non-polar areas of the protein contribute approximately 40-50% of the surface exposed to water [9]. For larger proteins, the non-polar areas are slightly lower [9].

It is often observed that a greater amount of protein adsorbs onto neutral hydrophobic surfaces [12]. This has led to the hypothesis that the main driving force for protein adsorption to surfaces is dehydration of a hydrophobic surface or dehydration of water from protein functional groups. In terms of protein adsorption to surfaces, the hydrophobic interaction is defined as the strong attractive force between non-polar species interacting in aqueous solution [13]. This occurs since the hydrogen bonding network (or structured water) is greater surrounding nonpolar molecules incapable of hydrogen bonding with water, and when two non-polar surfaces surrounded by structured water come into contact, the structured water is eliminated, resulting in a large entropic gain [13].

Surprisingly, temperature does not play a large role in the hydrophobic effect [3]. Increasing the temperature results in an expanded self-associated water network which

allows more space for hydrophobic solutes which increases ΔS (and makes –TΔS more negative) while non-bonding repulsive contacts between water molecules increase with the increase in temperature which causes ΔH to become more positive [3]. Thus, the entropic and enthalpic contributions with respect to temperature are nearly equal and balance each other.

1.2.2. Electrostatic Interactions

In aqueous solution, proteins are usually charged, arising from the association/ dissociation of protons from acidic or basic amino acids. The surface may also be charged (ie. carboxylated or aminated polymers) or neutral (ie. polyethylene oxide or Teflon^{TM}). Often, the surfaces of formally neutral polymers become charged in ionic media such as buffers. This potential may be measured as a zeta potential, ζ. A comprehensive review of zeta potentials for common polymers has been compiled by Kirby et al [14]. However, there is difficulty obtaining accurate measurements of zeta potentials since results are often reported using large differences in the concentration of the counter ion. The zeta potential is affected by pH, counter ion concentration, counter ion type and valency, ionic strength, ionic and nonionic surfactants [14]. The zeta potential for polystyrene, poly(methyl methacrylate) and polylactide in the presence of buffer are all ζ ~ -10 – -30 mV [15]. It is important to note that most of our experiments are carried out in deionized distilled water and that the zeta potential for most of the polymers studied in this thesis are comparable and would have a similar potential at the surface regardless of polymer type. In buffer, some counter-ions surround the protein and

the substrate surface with the remaining ions diffuse through the solution [9]. The electrical double layer comprises both the charge on the surface and its compensating surrounding charge [9].

When a protein approaches the surface, their electrical double layers begin to overlap with a resulting change in the electrical Gibbs free energy ($\Delta G_{el,\ ads}$) equal to the difference between the electrical Gibbs free energy (G_{el}) before and after adsorption. The most favorable outcome is charge neutralization. Remaining net charges in the contact zone between the adsorbed protein and the surface form an unfavorable electrostatic potential [9].

In fact, it is possible for a protein to adjust its own charge for optimal adsorption to a surface. For example, an investigation of α-lactalalbumin in free solution, adsorbed to a positively or negatively charged polystyrene surface at an ionic strength of 0.05M revealed significant differences in the shape of the proton titration curves for sampled pHs of 3 – 7 [9]. At pH 4.0, α-lactalalbumin on the positively charged surface had a net charge of 0 while the protein adsorbed to the negatively charged surface had a charge of +10 [9].

Furthermore, indirect incorporation of buffer electrolyte may also play a role in the charge neutralization. Direct evidence has been obtained by tracing the inclusion of radiolabelled ions such as $^{22}Na^{+}$ and $^{133}Ba^{2+}$ into human serum albumin (HSA) via electron spin resonance (ESR) [16]. The incorporation of ions into a protein has been postulated to explain why proteins are repelled from a like-charged surface, since it is

highly unfavorable for a protein to integrate enough oppositely charged counter ions to neutralize the surface and protein charge [17].

1.2.3. Protein Structural Arrangements

Proteins adsorbed to solid surfaces can undergo conformational changes since proteins have relatively low structural stability and can unfold to bond with the surface [3]. However, globular proteins generally do not completely unfold and their adsorption dimensions are similar to the native structure in solution, even if conformational changes occur upon adsorption [18].

When a protein adsorbs to a surface, aqueous water is removed from one side of the protein and the non-polar areas of the protein can become exposed to the surface without contact with water [9]. Subsequently, the hydrogen-bonded α-helix or β-sheet structure of the protein may become destabilized and the rotational mobility of the peptide backbone may increase. Thus, the changes in the secondary structure of the protein may result in an increase in conformational entropy.

1.2.4. London-dispersion Interactions

London dispersion forces originate from interactions between fixed and/or induced dipoles. The London dispersion forces between a molecule and a surface under water are attractive under most conditions. However, obtaining and isolating individual protein interactions with a surface is not experimentally feasible [19]. Theoretically, the London dispersion interaction energy is treated in a simple model by pair-wise

summation of London dispersion energies between all molecules of the interacting bodies. Since the attractive force occurs between a protein and a surface, the Gibbs free energy of adsorption increases linearly with increasing dimensions of the protein molecule and drops off exponentially with increasing separation between the protein and surface [9]. Obtaining more accurate values is hampered by the irregular structure of the protein, which is currently theoretically modeled as a sphere.

1.2.5 Characteristics of an Adsorption Process

In summary, far away from the surface, proteins exist in their native conformation, surrounded by solvent. Any movement of the protein occurs via convection or diffusion [9]. At approximately 10 nm from the surface, protein movement is affected by interfacial forces, such as the hydrophobic effect [9]. At approximately 1 nm from the surface, the protein encounters electrostatic interactions and London dispersion forces occur in the sub nanometer range [9]. Lastly, Born repulsion prevents atoms of the protein and surface from fusing. After the protein adsorbs to the surface it may 1) reversibly detach or 2) undergo conformational changes to form multiple bonding [9].

1.3 Human Serum Albumin (HSA)

Human serum albumin (HSA) is the only protein used in this thesis for adsorption studies because HSA is the most abundant protein in plasma, and is suitable for modeling protein interactions to blood contact materials. Furthermore, since HSA is easily prepared

in large quantities, it may be the most studied protein second only to insulin [20] and thus its structure, amino-acid sequence and many solution properties are well-known.

HSA is a globular protein and a carrier of fatty acids, although it has no enzymatic or hormonal activity [21]. HSA, with a molecular weight of 66.5 kDa, consists of 585 amino acids in a single polypeptide chain with 17 disulfide cysteine bridges and one free cysteine thiol [22]. The crystal structure of HSA is heart shaped, with three homologous domains. Each domain is made up of two subdomains A and B with 4 and 6 α-helices, respectively (Figure 1.2a) [23]. The crystal structure shows HSA to have dimensions of 3 x 8 x 8 nm [24]. However, reports of the solution structure of HSA have been inconsistent. At neutral pH HSA is reported to be a prolate ellipsoid with dimensions of 4 x 4 x 14 nm, based largely on hydrodynamic experiments [25,26,27], and low-angle X-ray scattering [28]. However, Ferrer et al. [29] suggested that the albumin structure in solution at neutral pH is similar to the crystal structure and that the proposed prolate ellipsoid structure is incorrect.

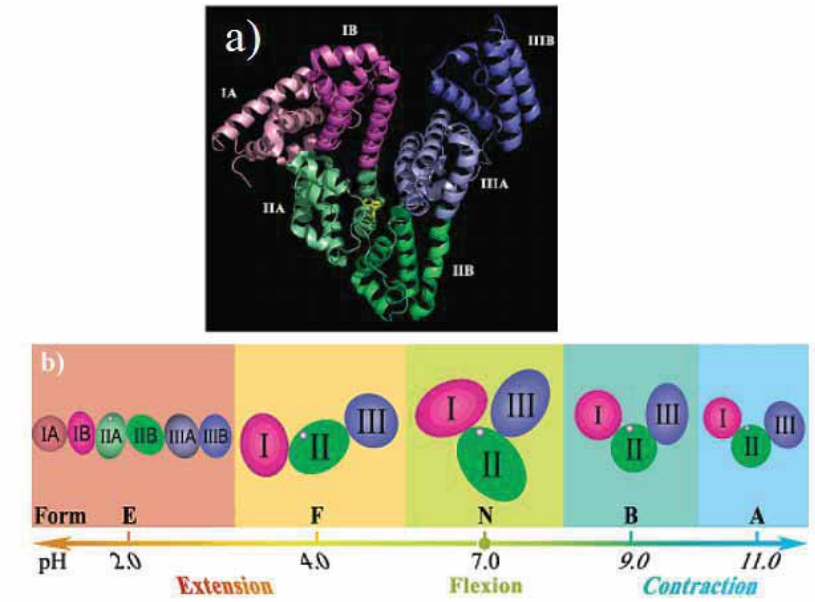

Figure 1.2: a) Structure of HSA with domains 1, II and III in purple, green and blue, respectively. b) Conformational transitions of HSA as a function of pH [31]. Reprinted from Qiu, W., et al. J. Phys. Chem B, 2006, 110, 10540-10549 with permission from ACS publications.

In aqueous solution, HSA exists in five pH-dependent conformations: E, F, N, B, and A (Figure 1.2b) [30]. At neutral pH, HSA exists in its most common norm (N) state. This isomer exhibits a tertiary structure with mostly α-helices [31]. Below the isoelectric point (4.7-5.4), HSA exists in an expanded fast migrating (F) form and below pH 2.7, HSA becomes completely extended (E). In the E form, the α-helix content is even more reduced with increasing β-sheet formation and the interdomain and inter-subdomain contacts are disrupted [31]. Even at this low pH, dynamic light scattering showed no protein aggregation [30]. Above pH 8.0, HSA changes to the basic (B) form and above pH 10.0, the structure transitions to an aged (A) form. For the B form, there is a slight reduction of α-helical content and an increase in β-sheet formation.

1.4 Techniques for Studying Protein Adsorption

Prior to the 1990s, bulk analytical techniques were mainly used to study biomedical surfaces since many of the early biomaterials such as silicones, metallic surfaces or polyurethanes were mostly homogeneous [2].

These bulk techniques include optical spectroscopies such as infrared spectroscopy, which can give information on the conformation (α-helices, β-sheets, turns, and random coil structures) of an adsorbed protein by analyzing the amide IR bands [9]. Similarly, circular dichroism may also provide information on the conformation of adsorbed protein [9]. Radiolabelled protein and quartz crystal microbalance (QCM) provides excellent analytical sensitivity on the amount of adsorbed protein on a surface. Ellipsometry, reflectometry and other optical wave guide spectroscopies are particularly sensitive for studying interfaces, while XPS and mass spectrometry techniques provide surface sensitivity [9].

Increasingly, spatially well-defined materials such as lithographic patterning, spun-cast films, or microcapsules for drug delivery have been prepared as potential biosensors or biomaterials. However, the distribution of the chemical components of the substrate or selective adsorption of bio-components to the surface is not always at a size scale which can be monitored by traditional microscopy or chemical analysis techniques. For example, Fourier transform infrared spectroscopy (FTIR) [32], surface plasmon resonance (SPR) [33,34,35], ellipsometry [36], quartz crystal microbalance (QCM) [37], and radiolabeling [38] provide good analytical sensitivity with limited spatial resolution, while atomic force microscopy (AFM) [39] and transmission electron microscopy (TEM)

[40] offer sub-nm spatial resolution but limited chemical recognition. Table 1.1 contrasts and compares some typical microscopy techniques used for studying protein adsorption.

Table 1.1: Common microscopy methods for characterizing protein adsorption to surfaces.

Method	**Principle**	**Depth** (nm)	**Lateral Resolution** (nm)	**Quanti-tative**	**Ref**
AFM	Measure attractive and repulsive forces between tip and surface	0.5	0.3	x	41
Fluorescence (near field)	Label emits light when excited	5	20	✓	42
CLSM	Optical microscopy that acquires in-focus images at different depths	2000	200	✓	43
SPR	Optical method for measuring the refractive index of very thin layers of material adsorbed on a metal	0.5	100 x 1000	✓	44
SEM	Secondary emitted electrons from a focused beam	0.5	10	x	45
TEM	Interactions between a beam of electrons and the sample	<100	0.1	x	40
TOF-SIMS	Ion bombardment releases secondary ions	<1000	100	✓	46
XPS	X-rays cause emission of electrons with known kinetic energy	<25	1000	✓	47
STXM	Focused X-ray beam transmitted through sample	1-200	40	✓	50
X-PEEM	Detect emitted secondary electrons with CCD	10	80	✓	50

Synchrotron-based spectromicroscopy techniques such as X-ray photoemission electron microscopy (X-PEEM) [48,49] and scanning transmission X-ray microscopy (STXM) [50,51,52,53], which are both based on near-edge X-ray absorption fine structure (NEXAFS) spectroscopy, afford a suitable balance of spatial resolution and chemical sensitivity. At the C 1s edge, quantitative chemical characterization can be

achieved with detection limits in the part per thousand range with good spatial resolution (80 nm X-PEEM, 30 nm STXM). The Hitchcock research group has been involved in optimizing and developing STXM and PEEM microscopes for protein adsorption studies to novel surfaces for over a decade [54-55, 58-61].

1.5 X-ray Spectromicroscopy Studies of Protein Adsorption

Previously, Cynthia Morin (2000-2004) [54] optimized a polystyrene-poly(methyl methacrylate) (PS-PMMA) blend surface [58], forming hydrophobic and "hydrophilic" domains for the study of human fibrinogen (Fg) adsorption to the surface [60], while Li Li (2002-2006) [55] studied HSA adsorption to the PS-PMMA surface as a function of concentration [61], exposure time and pH [59].

1.5.1 Optimization of a PS-PMMA blend surface

Since PS and PMMA are immiscible polymers, their blends phase segregate in the bulk [56] and at the surface [57]. The resulting system of PS-rich and PMMA-rich domains serve as a suitable model for a polymeric biomaterial with regions having different surface polarities and hydrophobicities, which may drive selective protein adsorption.

In 2001, X-PEEM imaging of a high molecular weight PS/PMMA 30/70 (PS = 1.07M, PMMA = 300K) film annealed at 160 °C (2h-18h) gave slightly different results compared to STXM [58]. X-PEEM (Figure 1.3a), which samples the top 10 nm of the film, showed the surface to be composed of PMMA domains (green) embedded within

the PS matrix (red) while STXM, which operates in transmission mode, clearly showed layers of PMMA domains at different depths (dark green and light green) within the PS matrix (Figure 1.3b). Even after annealing, the PMMA domains and PS matrix do not extend through the full thickness of the ~100 nm film, which adds greater complexity to the STXM analysis. Thus, for the study of protein interactions with the PS/PMMA surface, X-PEEM is a much more suitable and sensitive technique. In later STXM studies with micron-scale phase segregating polymer blends, the films were made with thicknesses in the 20-40 nm range. In such cases the individual components do in fact span the full film thickness [59].

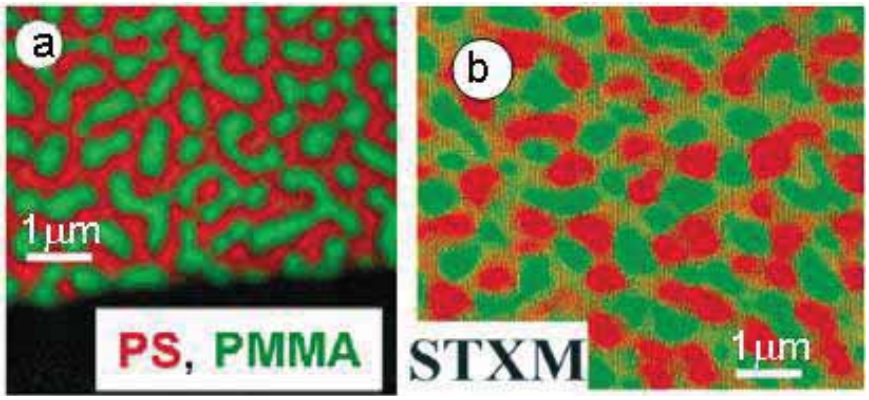

Figure 1.3: Comparison of (a) X-PEEM, (b) STXM imaging for PS/PMMA 30:70 w/w [58]. Reprinted from Cynthia Morin et al. J. Electron Spec., 2001, 121, 203-224, with permission from Elsevier.

Quantitative analysis obtained by fitting the experimental average NEXAFS spectrum with PS and PMMA reference spectra revealed the surface to be composed of 62(5)/38(5) area/area for the PS/PMMA 30/70 film. Strikingly, although the surface was dominated by PS, PMMA was the major component (70 w/w) in the starting solution. This system thus reveals significant differences between the surface and the bulk. STXM

imaging through the entire film thickness showed that a larger amount of PMMA was present below the 10 nm depth, and in the bulk PMMA likely forms the continuous phase.

1.5.2 Fibrinogen (Fg) Adsorption to PS-PMMA

Fg (0.05 mg/mL) was adsorbed from phosphate buffer (10 mM) to PS/PMMA. Figure 1.4a shows the absolute qualitative mapping of this system with PS, PMMA and Fg color coded in red, green and blue, respectively [60]. The PS continuous phase is strongly pink, arising from the combination of "red" PS and "blue" Fg. In contrast, the domains of PMMA are almost pure green. Thus there is a greater thickness of Fg adsorbed on the PS domains. The quantitative analysis of region-selected spectra support these qualitative observations with 19(5)% and 9(5)% Fg detected on the PS-rich and PMMA-rich regions, respectively.

In comparison, the absolute qualitative mapping of Fg adsorbed from 0.05 mg/mL from doubly distilled deionized (DDI) water to PS/PMMA showed the PS domains to be essentially red (Figure 1.4b). The quantitative analysis showed 0(5)% Fg adsorbed to PS and 19(5)% adsorbed to PMMA, essentially a reversal compared to the buffered system. As the qualitative maps show, in each case, the protein prefers to adsorb to the interface between the PS and PMMA domains. These results were supported by ^{125}I radiolabelling data of Fg adsorption to pure PS, pure PMMA and the PS/PMMA blend. For the buffer system, at almost all Fg concentrations sampled (0.0 – 1.0 mg/mL Fg), adsorption to PS was about 2-fold greater than on PMMA. For adsorption from DDI water, very similar

adsorption isotherms were seen over the range of 0.0 – 0.5 mg/mL and almost no preference was observed [60].

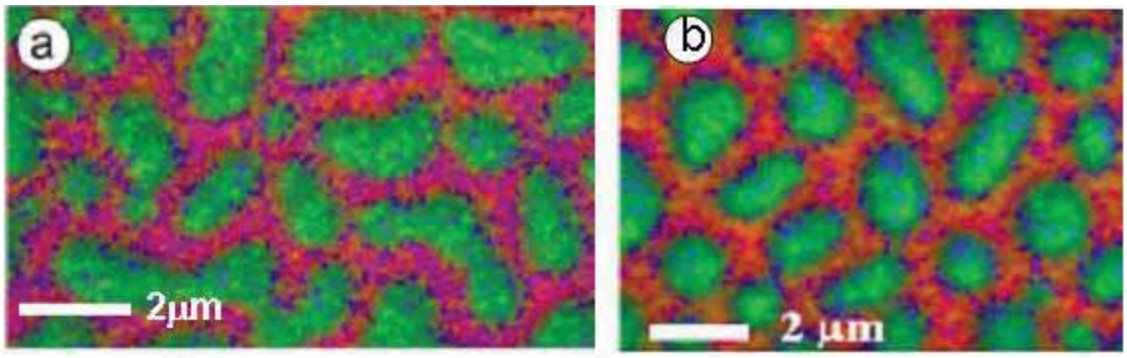

Figure 1.4: Color coded rescaled component maps of 0.05 mg/mL Fg adsorbed to PS/PMMA from (a) buffer and (b) water. PS = red, PMMA = green, Fg = blue [60]. Reprinted from Cynthia Morin et al. J. Electron Spec., 2004, 137-140, 785-794, with permission from Elsevier.

1.5.3 HSA adsorption to PS-PMMA

The surface of a 30:70 PS/PMMA blend was exposed to HSA at concentrations of 0.005, 0.01 and 0.05 mg/mL for 20 min from DDI water [61]. The absolute X-PEEM color-coded images are presented in Figure 1.5a-c. At low HSA concentrations (0.005 mg/mL), the PS and PMMA domains are red and green, respectively; however, at higher HSA concentrations (0.05 mg/mL), the PS and PMMA regions are pink and teal, signifying that more HSA adsorbs to the surface as the protein concentration increases.

The quantitative results clearly show that adsorption increases from interface (2.5-2.8 nm of adsorbed HSA) > PS (2.1-2.6 nm of adsorbed HSA) > PMMA (1.3-2.1 nm of adsorbed HSA). This trend is slightly different compared to the one observed for Fg adsorption to PS/PMMA, where Fg prefers the less hydrophobic surface of PMMA when adsorbed from DDI. Since the physiological ionic strength of plasma is ~150 mM [62],

we suggest the preference of Fg for PMMA under zero ionic strength may result from adsorption via a non-native protein conformation, where the more polar amino acid residues may preferentially adsorb to the polar PMMA domains.

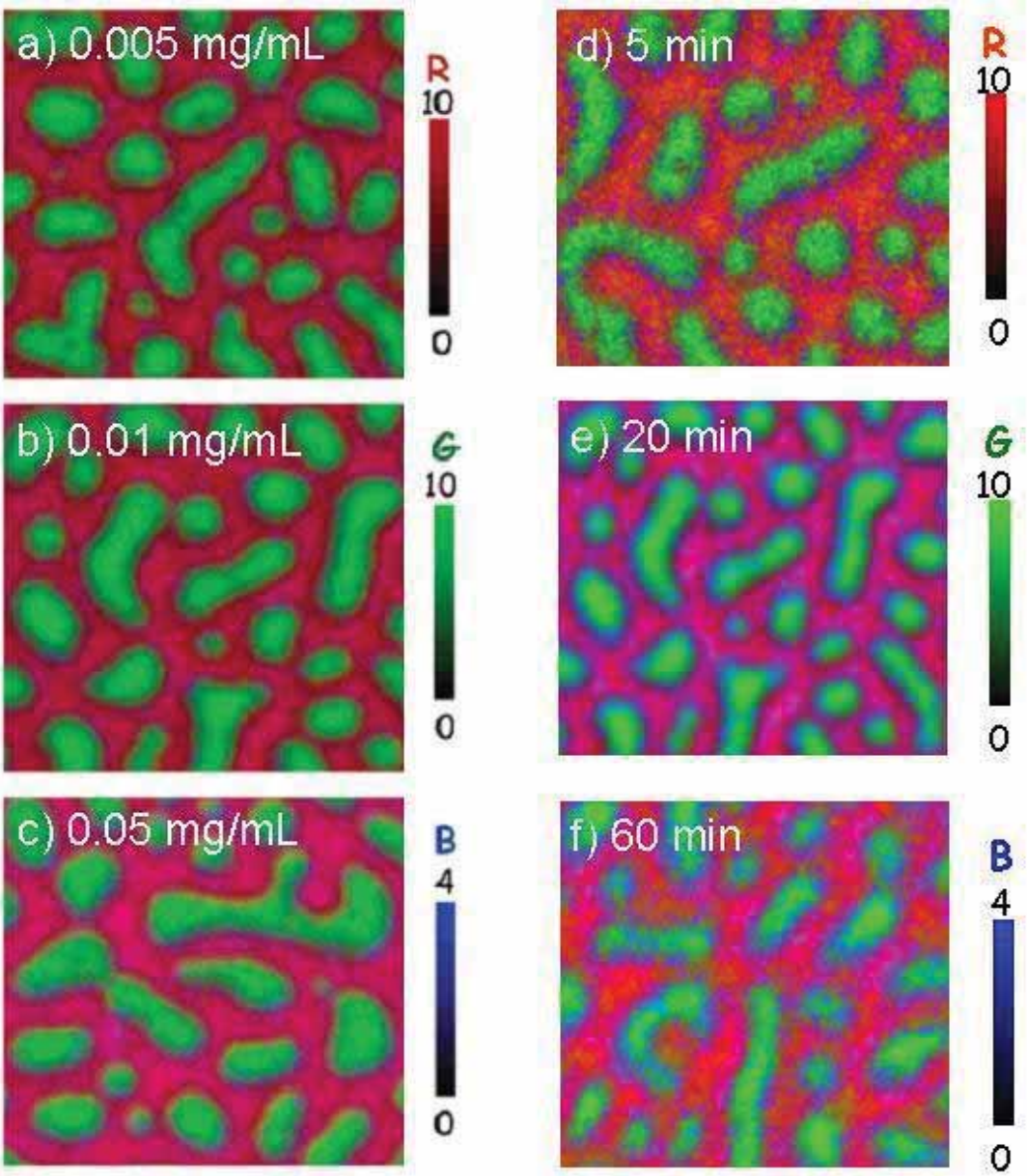

Figure 1.5: X-PEEM color coded composite maps of HSA adsorbed to PS/PMMA films with HSA concentrations of: (a) 0.005 mg/mL, (b) 0.01 mg/mL, (c) 0.05 mg/mL; and 0.05 mg/mL HSA adsorbed to PS/PMMA for: (d) 5 min, (e) 20 min, (f) 60 min. PS = red, PMMA = green, HSA = blue [61]. Reprinted from Li, L., et al. J. Phys. Chem B, 2006, 110, 16763-16773 with permission from ACS publications.

HSA adsorption to PS/PMMA was also studied with respect to exposure time. HSA (at 0.01 mg/mL concentration) was adsorbed to PS/PMMA for 5, 20 and 60 min. The rescaled color-coded maps show that HSA adsorption to the surface is varied, depending on exposure times. With a 5 min exposure, the PS and PMMA domains are more red and green, respectively, and become pinker and more teal as time increases to 20 and 60 min exposures (Figure 1.5d-e).

Clearly, this study showed that at low HSA concentration and short exposure times, HSA prefers the interdomain regions between PS and PMMA. At longer exposure times, there is evidence of redistribution of protein towards mainly the PMMA region and to some extent, the PS region. Since HSA is a globular protein with both exposed hydrophobic and hydrophilic domains, it is suggested that the hydrophobic areas bind more tightly to PS (contact angle of 97±5°) and the hydrophilic regions prefer PMMA (contact angle 76±5° [63]). Moreover, since the PS matrix is favored initially over PMMA, hydrophobic interactions are certainly involved in the adsorption process.

Furthermore, 0.05 mg/mL HSA was adsorbed to the PS/PMMA surface at pH 2.0, 4.0, 7.0, 8.6 and 10.0 [59]. Figure 1.6 shows the rescaled color-coded maps of HSA adsorbed to PS/PMMA with PS, PMMA and HSA shown in red, green and blue, respectively. The wide variation in color reveals differences in the adsorption distribution with respect to pH and protein conformation. The blue color corresponding to HSA is consistently strongest at the PS/PMMA interface regardless of pH. At extremely alkaline pH, similar amounts of HSA are adsorbed to the PS and PMMA domains. However, at

pH 4, close to the isoelectric point, there is a preference for PMMA over PS, while at pH 8.6 there is a preference for PS over PMMA.

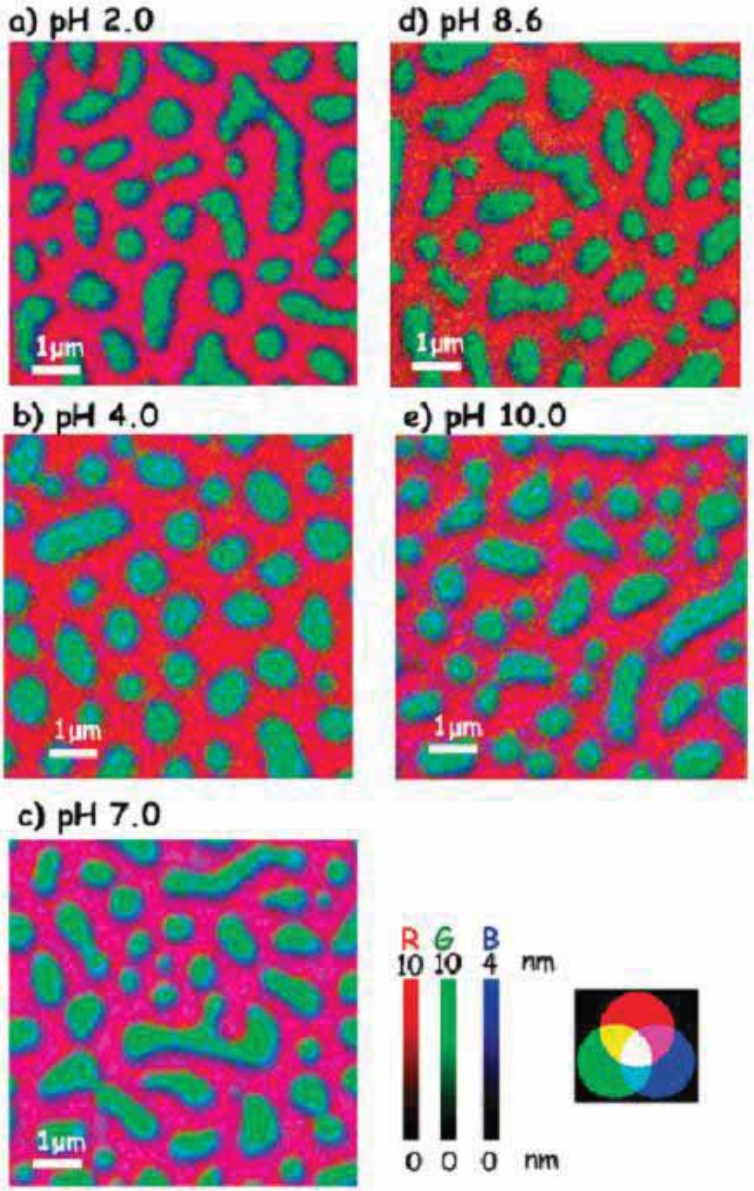

Figure 1.6: Rescaled color coded images of HSA adsorbed to PS/PMMA at the C 1s edge at five different pH. PS = red, PMMA = green and HSA = blue [59]. Reprinted from Li, L., et al. J. Phys. Chem B, 2008, 112, 2150-2158 with permission from ACS publications.

Since the HSA conformation varies depending on pH, it is possible to qualitatively interpret the amount of protein adsorbed to different areas of the surface derived from the X-PEEM data in terms of the relative amounts of hydrophobic and hydrophilic regions present at the protein surface at different pH. For instance, at pH 8.6, as the conformation of HSA contracts, more hydrophobic residues may be present at the surface, thus resulting in an adsorption preference for hydrophobic PS. In contrast, as the conformation of HSA expands at pH 4, possibly more hydrophilic residues are present, giving rise to a greater amount of protein adsorbed to the polar PMMA region.

1.6 Objectives

While Morin and Li did an outstanding job of optimizing the PS-PMMA substrate, followed by detailed Fg and HSA protein adsorption studies, there are other more biologically-relevant systems in the vast biomaterials area that are of interest. There are two main goals for my Ph.D thesis:

1. Develop and optimize novel candidate biomaterial polymeric blends, particularly those more closely connected to current medical usage.

2. Study protein adsorption to these new surfaces to obtain insights into biocompatibility.

In this thesis, I explore blends of PS with the biodegradable polymer polylactide (PLA), which is a polymer FDA-approved for biodegradable sutures. This blend system was optimized to obtain micron-sized phase segregation, which is a suitable platform to

study the effect of ionic strength and surface rugosity on protein adsorption (chapters 4&5).

Furthermore, since only hydrophobic polymers were examined previously, I blended PS with polyethylene oxide (PEO) a hydrophilic polymer commonly used to increase the biocompatibility of biomaterials and to decrease protein adsorption. However, since this system is hydrophilic, the PEO polymer strands must be crosslinked to prevent dissolution upon protein adsorption. I studied the effect of the crosslinker pentaerythritol triacrylate (PETA) on protein adsorption (chapter 6) followed by HSA adsorption at varying concentrations (0.05 – 0.005 mg/mL) to blends of PS-PEO to examine the adsorption to hydrophobic vs. hydrophilic surfaces (chapter 7).

Finally, since the previous systems examined were composed of neutral polymers, I developed and optimized PS blended with poly(methyl methacrylate)-b-polyacrylic acid (PMMA-PAA) to examine the electrostatic effect, since polyacrylic acid is negatively charged at neutral pH. In this study, I investigated negatively charged protein vs. positively charged peptide adsorption to the surface and the effect of pH, which varies the charges of both the HSA protein and the surface (chapter 8).

CHAPTER 2: METHODS

2.1 X-ray Spectromicroscopy

2.1.1 X-rays from Synchrotron Sources

In the 1950s, the first particle accelerators were built for high-energy physics research for the study of particle physics via electron-positron collisions [64]. As the charged particles were accelerated, an unwanted energy loss was observed. This radiation by-product was named *synchrotron radiation* (SR). By the 1960s, scientists realized that synchrotron radiation contained several unique properties, which could not be generated by conventional sources [64].

The first experiments conducted with synchrotron radiation were performed in a parasitic mode, tapping off radiation from high-energy physics accelerators [64]. As the importance and versatility of synchrotron radiation was recognized, many facilities were shared or rededicated to the synchrotron radiation community. These facilities, known as first generation sources, used bending magnets to force electrons into a curved path to generate synchrotron radiation [64]. However, these rings were not fully optimized for maximum beam brightness.

Second generation sources were built exclusively for synchrotron radiation research in the mid 1970s, still using primarily bending magnets [64]. These facilities operated in the MeV – low-GeV range. However, the introduction of insertion devices (also known as wigglers and undulators) into storage rings further improved the spectral

properties of synchrotron radiation, and resulted in the development of third generation storage rings in the late 1980s (operating at the GeV range) [64].

Presently, over sixty synchrotron facilities are in operation or are being built around the world, including Canada's first synchrotron facility, the Canadian Light Source in Saskatoon [65]. Synchrotron radiation is electromagnetic energy, ranging from infrared to hard X-rays, released as electrons traveling at near light speeds undergo acceleration through a curved trajectory at fixed speed. The radiation from a synchrotron facility contains approximately five orders of magnitude more flux (photons/s/mrad/unit bandwidth) and ten orders of magnitude higher brightness (photons/s/unit solid angle/unit source area/unit bandwidth) than traditional UV lamps or X-ray tubes [64]. Only lasers operating in the IR and visible region have higher flux and brightness parameters than SR; in the vacuum UV, soft and hard X-ray regions, SR is the premier light source.

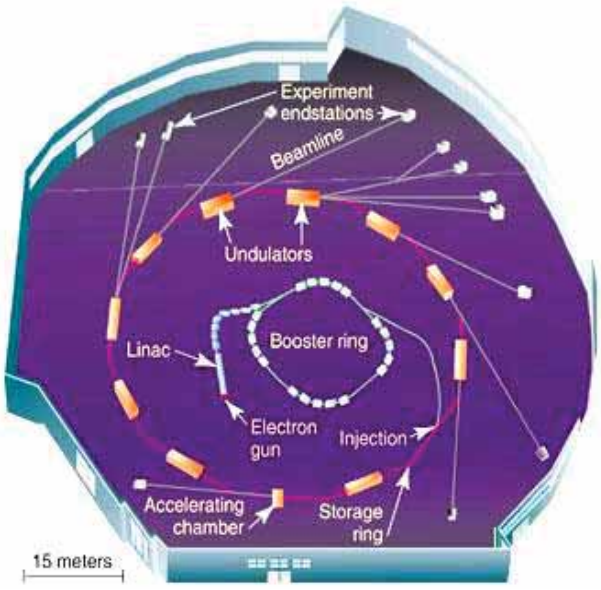

Figure 2.1: Schematic of the Advanced Light Source synchrotron facility [66].Reprinted with permission from the ALS users office.

There are four main components to a synchrotron facility: electron gun, linear accelerator, booster, and storage ring (Figure 2.1). An electron gun is used to create a stream of electrons. Just before the electrons reach the linear accelerator (linac), a klystron or a microwave amplifier interacts with the electrons, breaking the continuous stream into bunches of electrons [67]. These electrons are transferred into the linac where their velocity is increased to near light speeds. The electrons are transferred to a booster ring where the speed of the electrons is increased in a true synchrotron device. After the booster has accelerated the electrons their speed is given by:

$$E = \gamma m_0 c^2 \qquad \text{(eq 1)}$$

where E is the total energy, $\gamma = 1/\sqrt{(1-v/c^2)}$, m_0 is the mass, v is the velocity and c is the speed of light.

For example, the Advanced Light Source (ALS) is a 1.9 GeV device. After boosting, the electrons in the storage ring have a speed which is 99.999994% of the speed of light. Finally, the electrons are injected into the storage ring where they circulate emitting SR, with lifetimes ranging from a few hours to a few days. The most advanced 3rd generation SR facilities are operated in so-called ‘top-off’ mode, whereby there is a regular injection of a very small additional current (typically 0.1-2 mA, at 1-2 minute intervals). In this mode the user sees a nearly constant light output which is ideal for experimentation, not just because it is convenient, but also because the accelerator and beamline optics operate with much greater stability, and this reduces systematic noise. For the first 2.5 years of this thesis the ALS was operated with re-injection every 6-8 hours, while the ALS has operated in top-off mode since Feb 2009.

Typically SR storage rings are filled with ~10^{10} electrons that are circling at essentially the speed of light under vacuum. The ring usually contains four main types of equipment [68]. 1) The bending magnets force the electrons into a curved trajectory and synchrotron radiation is released tangential to the curve. 2) Insertion devices (IDs) supply a very large increase in the beam intensity and brightness, relative to bending magnet emission. There are two classes of IDs, **wigglers** which shift the continuous spectrum to higher X-ray energy and can increase hard X-ray flux by several orders of magnitude, and **undulators**, which emit a quasi-discrete spectrum where, in the undulator peaks there is typically 100-fold increase in beam intensity and 10^6 – 10^8 increased brightness. Wigglers and undulators, which are located in straight sections of the ring between the bend magnets, contain complex high field magnet structures that cause the electron beam to undulate (many small excursions) or wiggle (relatively few large excursions). It is the reinforcement of the SR emission process at successive accelerations along the ID that modifies the emission spectral properties [68]. 3) The energy lost in the SR emission process is replenished by electromagnetic fields oscillating at radio frequency (rf cavities) [64]. 4) Vacuum pumps maintain the vacuum within the ring itself [68].

2.1.2 The Photoelectric Effect

An X-ray beam can excite an absorbing atom in a sample when the energy of the incident beam is greater than the binding energy of the core electron. Excitation of a 1s (K-shell) or 2p ($L_{2,3}$ sub-shell) electron, etc., can be used for X-ray absorption

spectroscopy (XAS). When a core electron absorbs energy it is excited into higher unoccupied orbitals or into the continuum as a photoelectron.

The core levels of each element in the periodic table have specific binding energies between 50 eV and 80 keV [69]. Therefore, by tuning the energy of the incident X-ray beam to the appropriate value, element specific investigations can be made. After excitation or ionization of the core electron, the core hole that is created is refilled by an electron from a less tightly bound orbital, thereby either emitting an X-ray fluorescent photon in a radiative decay process, or by emitting one or more Auger electron in a non-radiative decay process (Figure 2.2).

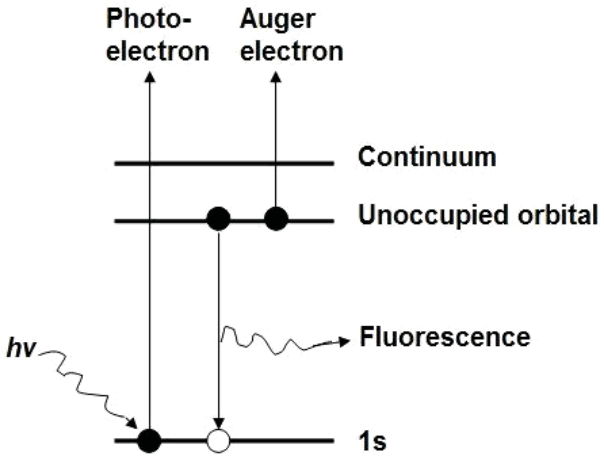

Figure 2.2: The photoabsorption process.

2.1.3 X-ray Absorption Spectroscopy (XAS)

The first X-ray absorption spectrum was collected in 1913 by Maurice de Broglie, who was experimenting with a rotating clockwork mechanism for detecting single crystal X-ray diffraction. As the crystal was rotated, he recorded the angles between the incident beam and the diffraction planes (ie. all X-ray energies) on a photographic plate and

discovered two sharp lines corresponding to the 1s (K-shell) X-ray absorption bands of Ag and Br in the photographic emulsion [70].

X-ray absorption spectroscopy is the measurement of changes in the linear absorption coefficient μ(E) as a function of energy (E). For transmission experiments, the absorption is described as:

$$I_1=I_0e^{-\mu(E)t} \qquad \text{(eq 2)}$$

where I_1 is the intensity of the beam transmitted through the sample, I_0 is the incident X-ray intensity, t is the sample thickness (cm), and μ(E) is the linear absorption coefficient.

Plotting the change in absorption ($\log I_0/I = \mu(E)t$ (transmission) or $Ie/I_0 \propto \mu(E)$ (total electron yield)) as a function of energy (eV) results in an XAS spectrum similar to the one shown in Figure 2.3 [71]. The spectrum is classified into three sections. The region where the incident energy of the X-rays is lower than the ionization threshold is known as the pre-edge region [71]. As the incident energy of the X-ray equals the binding energy, the core electron is excited to higher unoccupied valence orbitals and results in a sharp rise known as the absorption edge which corresponds to the 1s → np (intense and allowed) transition [72]. The region between 10 eV below the edge and 30 eV above the edge is the near-edge X-ray absorption fine structure (NEXAFS) region. Since this region consists mainly of excitations of the core electron into higher unoccupied orbitals (or conduction band states in a solid state picture), the NEXAFS region is a direct probe of the electronic structure of the molecule, rich in information on oxidation state and geometry [72].

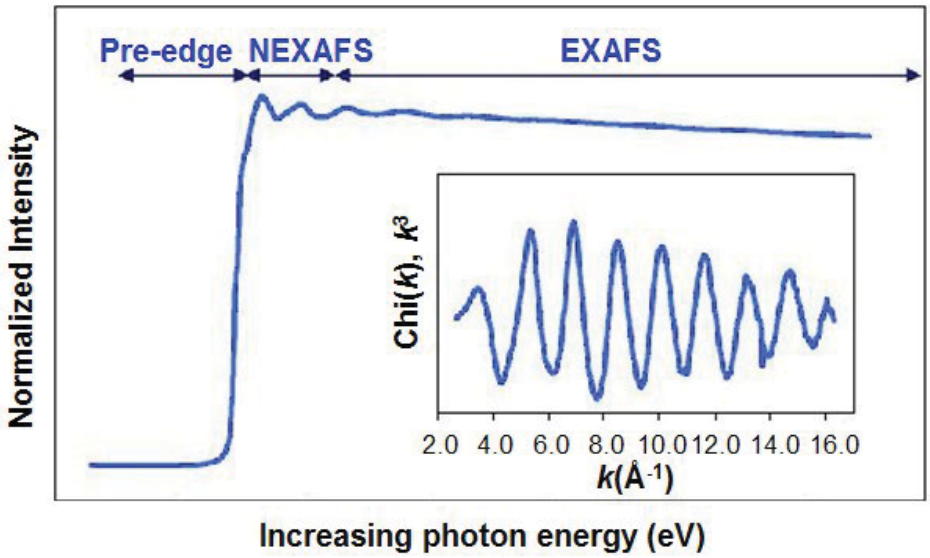

Figure 2.3: A typical X-ray absorption spectrum. Inset shows the k^3-weighted extracted EXAFS oscillation.

The region 30 to 1000 eV above the edge is the extended X-ray absorption fine structure (EXAFS) region [71]. The core electron has been ejected as a photoelectron from the atom and encounters neighboring atoms. The photoelectron is scattered back towards the originating atom, forming an interference pattern with the outgoing wave. From this interference pattern, structural information such as bond distances and coordination numbers of near atom neighbors can be obtained [71].

2.1.4 Electron Yield Detection for NEXAFS spectroscopy

Synchrotron-based NEXAFS spectroscopy is particularly well-suited for studying a single adsorbed or chemisorbed monolayer on a surface. Typically ~10^9 photons are required to detect a monolayer of 10^{15} molecules/cm^2 [73]. Given that the region of the surface sampled by the total electron yield technique (~10nm) is much less than the

photon penetration depth (~0.5 – 1 μm, for the photon energies used), the number of photons absorbed by a monolayer of adsorbed protein can be derived from the Beer-Lambert law $I = I_o e^{(-\sigma\rho t)}$ to be:

$$N_{abs} = I_0 A_0 (1-e^{-\sigma_x \rho t}) \approx I_0 A_0 \sigma_x \rho t \qquad \text{(eq 3)}$$

where I_0 [photons/(s cm^2)] is the incident photon flux density, A_0 [cm^2] is the area exposed to the beam, ρ [atoms/cm^2] is the areal density, σ [cm^2/atom] is the photon-energy dependent X-ray absorption cross-section, and t [cm] is the thickness of the protein layer. The number of created core holes,, and thus number of photoelectrons, Auger electrons and X-ray fluorescence photons produced are each proportional to the X-ray absorption cross-section [73]. However, measuring photoelectron yield alone is not a viable means of obtaining a NEXAFS spectrum since all the transitions below the ionization potential (IP), which are the bound state excitations, would not be recorded (Figure 2.4). Thus, only core hole annihilation processes such as Auger electrons or fluorescence should be used to obtain NEXAFS spectra [73]. For low-Z atoms, the 1s Auger decay is much more probable than fluorescence decay and dominates the secondary de-excitation process. For the C, N, O 1s edges used in this work, the Auger electron yield is more than two orders of magnitude higher than the fluorescence yield [73].

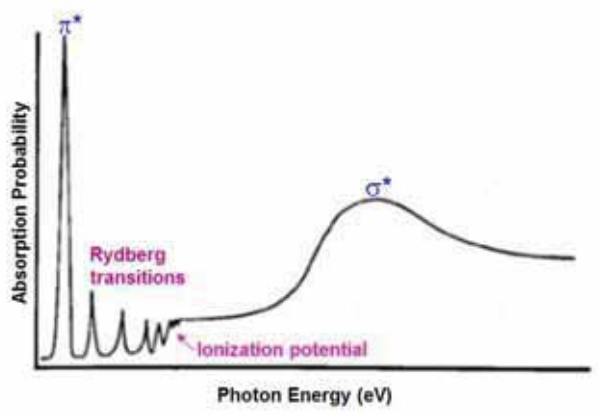

Figure 2.4: (left) Absorption probability from a typical diatomic molecule.

As the photon energy increases from below the absorption threshold ($h\nu < E_b$) to just above the absorption threshold ($h\nu > E_b$), an Auger peak is observed in the photoemission spectrum [73]. At this energy, the photoelectron cannot leave the sample because the kinetic energy is not high enough to exceed the work function. As the photon energy increases even further, then the photoelectron peak emerges. Since the Auger electron peak remains at a fixed kinetic energy, a window selected around the Auger electron peak in the electron energy analyzer can be used to obtain a NEXAFS spectrum via Auger electron yield (AEY) [73].

A NEXAFS spectrum can also be obtained from total electron yield (TEY) detection where all the electrons are collected for each photon energy step. The TEY signal is composed mostly of low energy electrons with kinetic energy below 20 eV, also known as the "inelastic tail" [73]. A percentage of this tail is composed of the inelastically scattered Auger electrons from the monolayer and gives rise to the NEXAFS spectrum [73].

Suppose we have a monolayer (A) adsorbed to a substrate (B). Then the depth that the photons can penetrate into the substrate composed of B atoms is limited by the photon mean free path ($\mu_x(h\nu)$):

$$\mu_x(h\nu) = n_v\sigma_x(h\nu) \qquad \text{(eq. 4)}$$

where n_v is the volume density and $\sigma_x(h\nu)$ is the X-ray absorption cross section [73]. From known tabulated results [74], the photon mean free path in many solids is typically 1 μm per keV of photon energy.

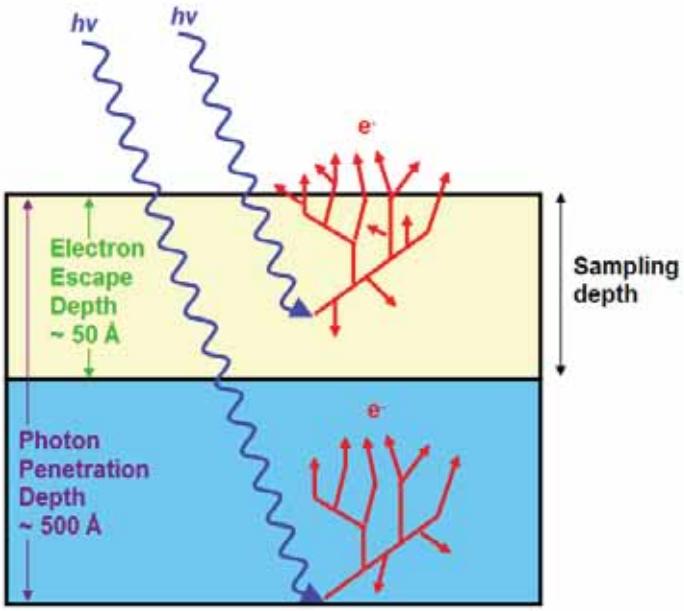

Figure 2.5: X-ray penetration depth and electron escape depth for total electron yield (TEY) detection.

After penetration in the substrate (B) and absorption of X-rays, the resulting photoelectrons and Auger electrons traveling toward the surface are scattered inelastically by electron-electron, electron-plasmon and electron-photon interactions [73]. These inelastically scattered electrons start a cascade of secondary electrons (Figure 2.5). This

leads to TEY being a surface sensitive detection technique since only the electrons with sufficient energy to overcome the surface potential barrier will be able to escape [73]. For samples measured at the carbon K-edge with the 10-12 keV/mm extraction fields and microscope column transmission properties of PEEM-2, the integrated sampling depth for a polystyrene thin film has been measured to be approximately 10 nm [75]. A similar sampling depth was reported by Gilbert et al for a different (Elmitec) PEEM from a metal sample at the Mn $L_{2,3}$ edge [76]. This suggests that the X-PEEM technique in the soft X-ray region samples the outer 5-20 nm of most samples. For this work I have used a 10 nm sampling depth as part of the quantization procedure. This is a reasonable assumption since electron propagation and band gaps are similar for most of the polymers I have studied.

2.1.5 Chemical Sensitivity of NEXAFS Spectroscopy

NEXAFS spectroscopy probes the empty unoccupied electronic states near the ionization threshold of a compound, which provides information on the molecular bonding and chemical structure [48]. C 1s NEXAFS spectroscopy is very sensitive to the functional groups incorporated within a molecule or (bio)polymer.

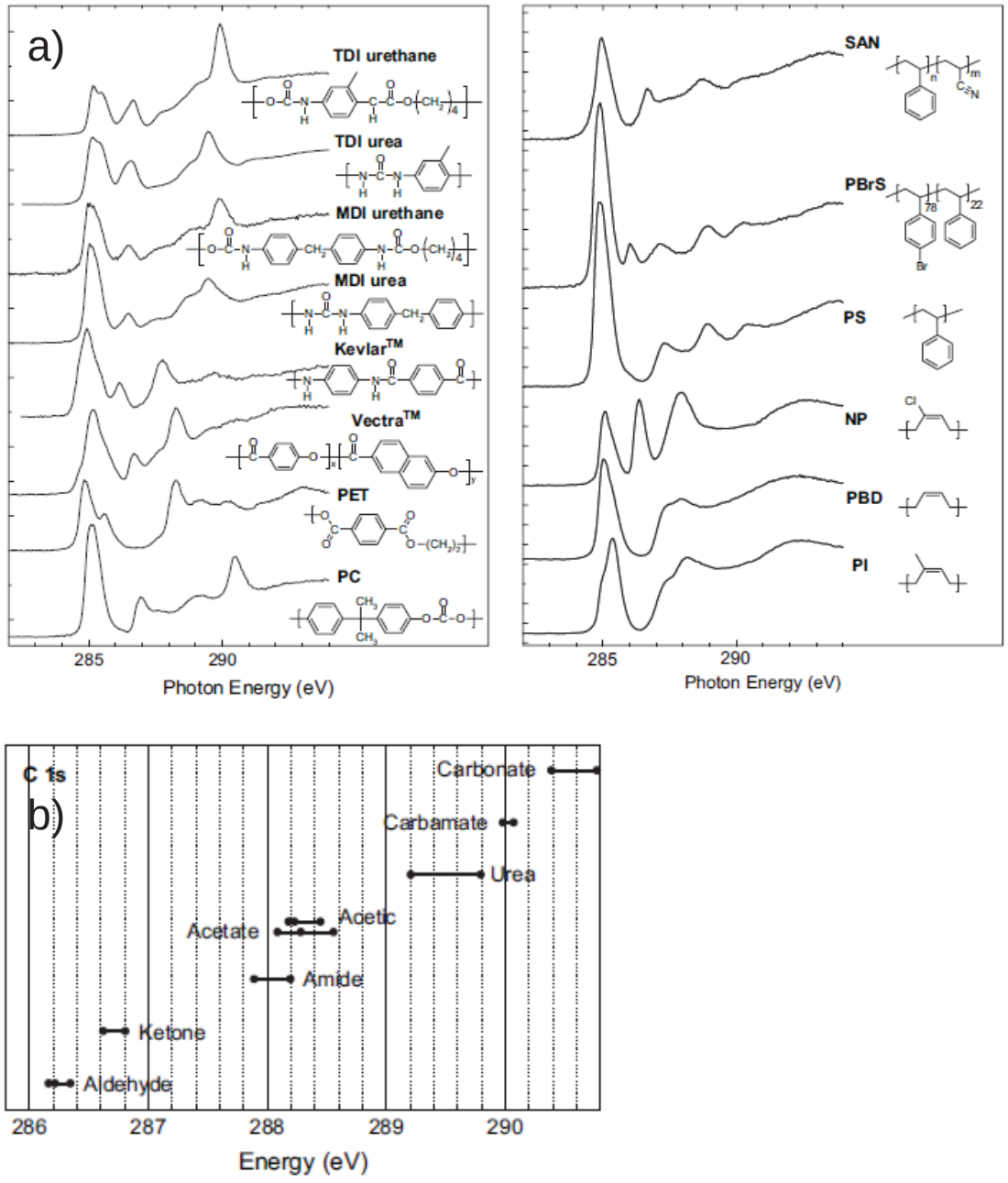

Figure 2.6: a) C 1s NEXAFS spectra and chemical structure of several polymers. b) Plot of the energy of the C 1s $\rightarrow \pi^*$ transition in various types of carbonyl containing functional groups [77].

Figure 2.6a showcases the rich variations in NEXAFS spectra of different polymers containing a variety of functional groups [50]. Molecules with C=C double bonds such as polystyrene (PS) exhibit a characteristic transition around 285 eV corresponding to the C1s → $\pi^*_{C=C}$ transition while carbonyl-rich molecules such as polyethylene terephthalate (PET) reveals an additional feature at 288.5 eV which arises from the C1s → $\pi^*_{C=O}$ transition. In fact, the phenomenological correlation diagram (Figure 2.6b) shows that the $\pi^*_{C=O}$ transitions seen in C 1s NEXAFS spectroscopy depend strongly on the charge withdrawing and electronegativity of the functional groups found in the material [50].

Figure 2.7 shows the NEXAFS spectra of all the polymers and molecules studied in this thesis: polystyrene (PS), polylactide (PLA), polyethylene oxide (PEO), UV-initiated crosslinker pentaerythritol triacrylate (PETA), block copolymer of poly(methyl methacrylate)-b-polyacrylic acid (PMMA-PAA), human serum albumin (HSA) and a cationic antimicrobial peptide, SUB-6.

PS is characterized by a C 1s → $\pi^*_{C=C}$ transition at 285.15(3) eV. PLA and PMMA-PAA exhibit strong C 1s → $\pi^*_{C=O}$ transitions at ~288.53(3) while HSA reveals a transition at 288.20(6) eV. The carbonyl transition for HSA is at a slightly lower energy than that in PLA since the amide functional group (R-CONH) is a less electronegative environment than the ester group (R-COOR′). The C 1s spectrum of SUB-6 also exhibits a strong C 1s → $\pi^*_{C=O}$ at 288.20(3) eV, and it has an additional C 1s → $\pi^*_{C=N}$ transition at 289.37(3) eV and significant intensity in the 286 – 287 eV region from the C 1s(C-R) → $\pi^*_{C=C}$ transitions.

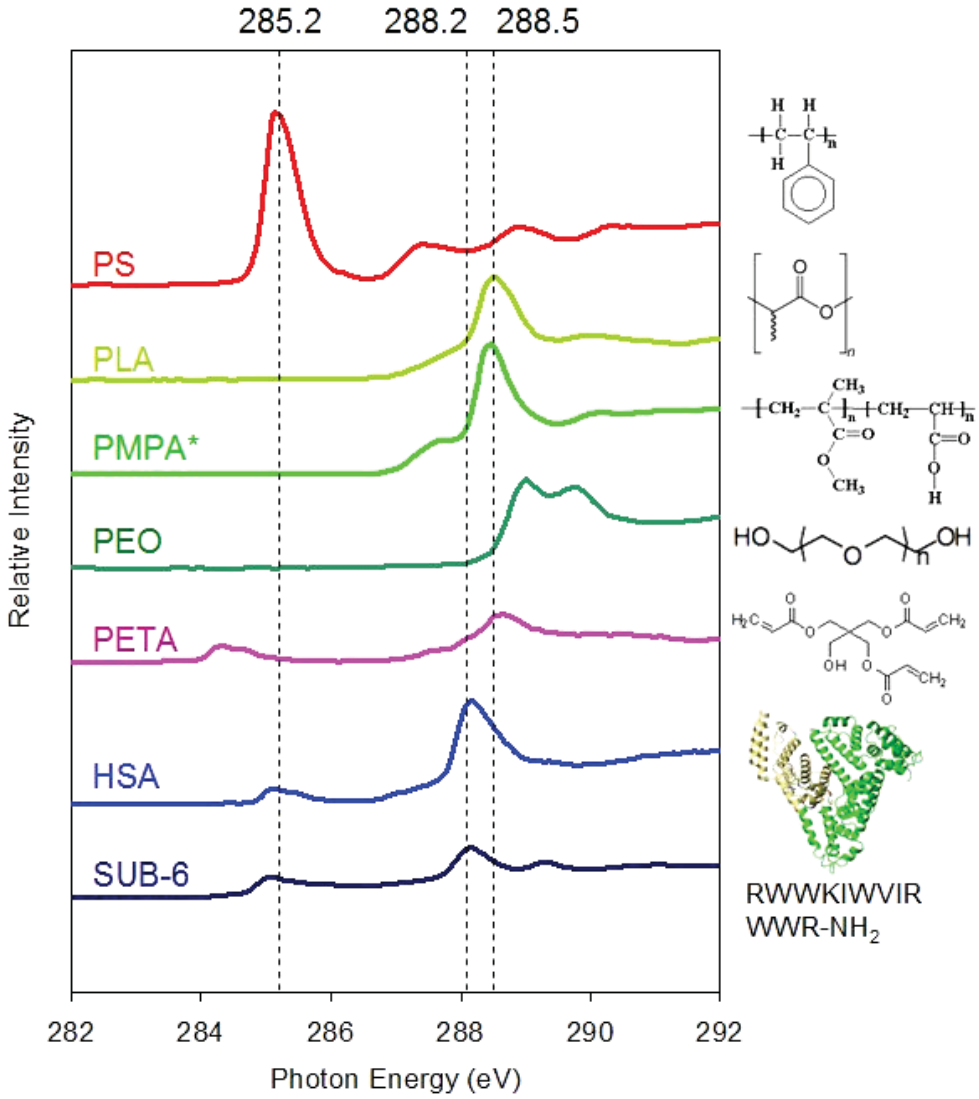

Figure 2.7: C1s NEXAFS spectra and chemical structures of the polymers, protein, peptide, and crosslinkers studied in this thesis. *This is the PMMA spectrum, used in place of PMMA-PAA since the NEXAFS spectra of the two are virtually identical.

In contrast, the PEO spectrum is dominated by C 1s → σ^*_{C-H} and C 1s → σ^*_{C-O} transitions at 289.0 and 289.8 eV [78]. PETA is characterized by two main transitions at 284.45 and 288.6 eV corresponding to C 1s → $\pi^*_{C=C}$ and C 1s → $\pi^*_{C=O}$ transitions. The C=C π^* transition at 284.45 eV is 0.7 eV lower than the transition obtained for

polystyrene which reflects conjugation of double bonds in the PETA structure. Thus, blends of PS with PLA, PEO or PMMA-PAA and HSA/SUB-6 adsorption can be easily distinguished via NEXAFS chemical contrast.

2.1.6 X-ray Photoemission Electron Microscopy

Spatially resolved NEXAFS spectroscopy can be obtained via TEY using an X-ray photoemission electron microscope (X-PEEM) (Figure 2.8). For X-PEEM, the surface is illuminated by X-rays and within the microscope field of view, the spatial distribution of the electrons that escape the surface is strongly magnified, transported through a suitable electrostatic or magnetic lens system, and recorded photographically or with a video camera [79]. The schematics of the X-PEEM optics are shown in Figure 2.9.

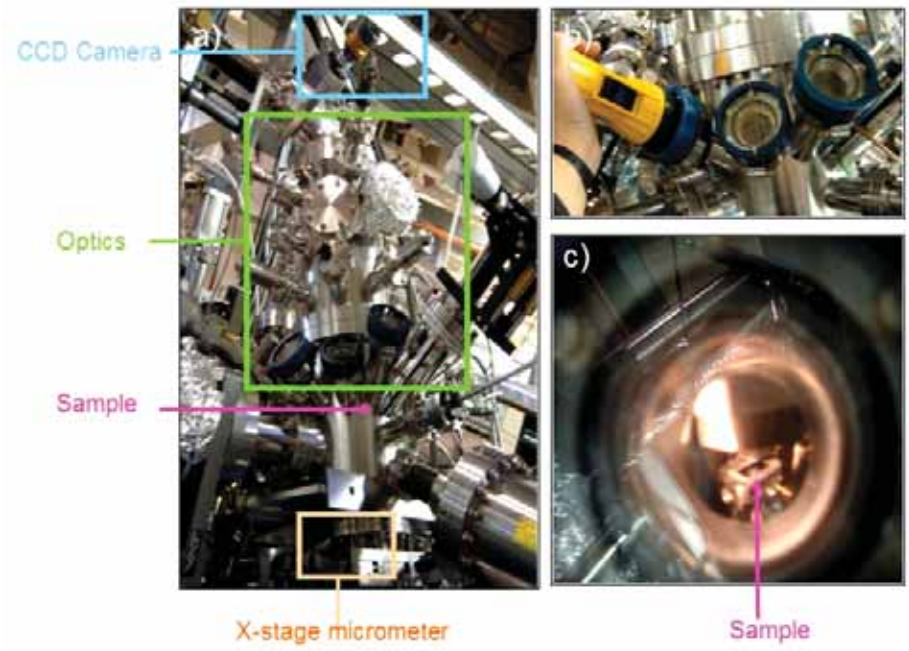

Figure 2.8: a) Photo of the X-PEEM2 microscope at the Advanced Light Source. b) Window into the X-PEEM manipulator. c) Sample position within the microscope.

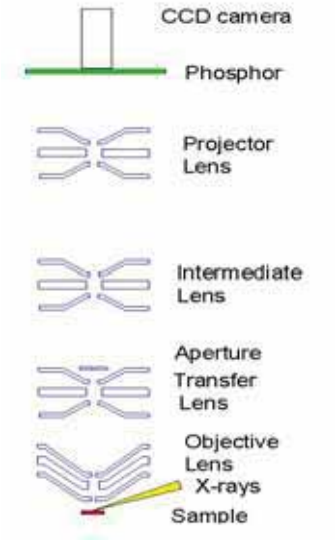

Figure 2.9: Schematic of the X-PEEM optics.

The first lens, or the objective lens, is composed of 3-4 electrostatic lenses [80]. To achieve high magnification, a 10-20 kV/mm electrostatic field is applied between the sample and the microscope, with a maximum of 30 kV/mm, however most samples show field emission above 20 kV/mm [81]. One major disadvantage of this optics set up is that the sample surface must be aligned perfectly normal to the optics to ensure that the accelerating field is cylindrically symmetric, otherwise, images are distorted [79]. An advantage of this set up is that accelerating the electrons reduces the angular spread, which decreases the changes in the electron trajectories induced by optical imperfections of the lens [79].

If the electrons emitted from the same place on the surface have different kinetic energies, chromatic aberrations of the microscope lenses cause the electron trajectories to fan out and blur the resulting image [79]. Similarly, electrons emitted at different angles follow slightly different trajectories through the microscope optics due to spherical aberration. To reduce image smearing from both spherical and chromatic aberrations, a contrast aperture is located near the back of the objective lens which allows only electrons with a well defined kinetic energy and angular range to pass. While a small aperture size improves the lateral spatial resolution, it reduces the total signal such that longer acquisition times are required to achieve a similar signal-to-noise ratio. Since the

incident photon flux is the same for both large and small contrast apertures in the PEEM column, use of the higher spatial resolution small contrast apertures typically leads to increased radiation damage [79]. For our experiments, we use the largest aperture available (50 μm), short dwell times (1s or less) and shuttering between images to obtain data with the lowest achievable radiation damage, even at the expense of spatial resolution and spectral density.

The remainder of the optics consists of a transfer lens, which produces a 1:1 image and two intermediate and projector lenses, which magnifies the image onto a phosphor screen [79]. The screen converts the electrons into a light image which is captured by a charge coupled device (CCD) camera.

For all of the X-PEEM work reported in this thesis, I used the PEEM-2 microscope located at bending magnet beamline 7.3.1 at the Advanced Light Source (ALS) in Berkeley, CA (Figure 2.10). A spherical grating monochromator supplies radiation from 175-1300 eV [81]. The vertical size of the X-ray source is approximately 30 μm, while the horizontal size of the source is about 300 μm full width at half maximum (FWHM) and a 10:1 horizontal demagnification is used to obtain a 30x30 μm field of view [81]. A mask upstream from the monochromator can be used to select left circularly (above plane), linear (in plane), or right circularly (below plane) polarized light. Typically, for our X-PEEM experiments we use right circularly polarized light, which provides slightly better energy resolution than linear or left circularly polarized light since some areas of the monochromator have contamination problems.

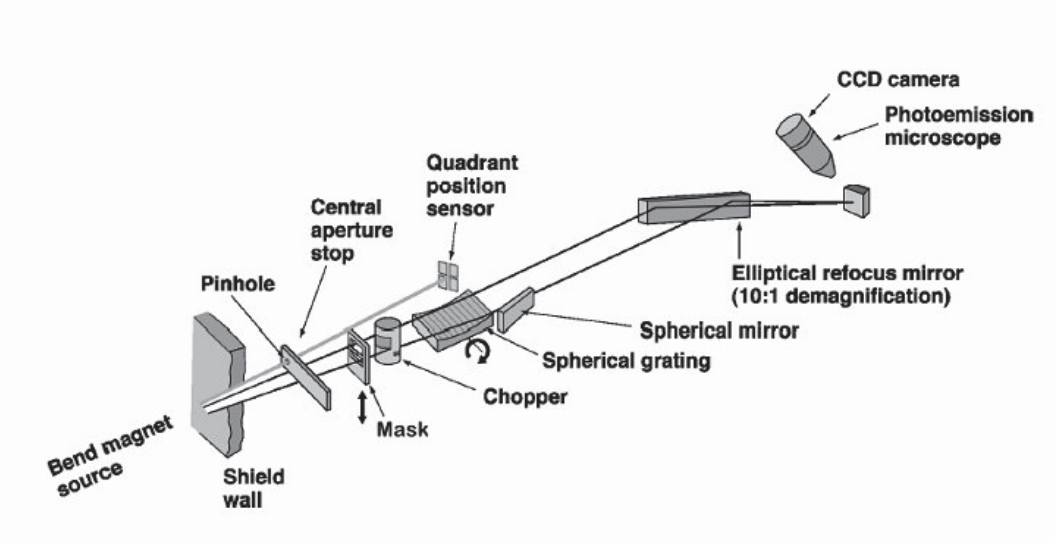

Figure 2.10: Beamline 7.3.1 set up at the Advanced Light Source.

A 100 nm-thick titanium filter is inserted before the exit slit for C 1s and N 1s experiments. The Ti filter removes second order light and thus spectral contributions from O 1s absorption, which occurs at ~260-275 eV in the apparent first order spectrum. For O 1s experiments, the Ti filter must be removed since the Ti 2p absorption edge occurs at 450 eV, below the O 1s edge (~540 eV).

2.1.7 Data Acquisition

One begins by inserting a sample, via a load-lock, into the PEEM manipulator, positioning it at the focal point of the PEEM column, aligning the tilt of the manipulator to achieve an exactly orthogonal orientation relative to the microscope axis, and then adjusting lens currents to achieve the desired magnification and best focus. At this point, an area of interest is selected, and images at a full field of view (typically 30x30 μm) are

recorded using photon energies with the strongest chemical contrast. For example, for PS-PLA thin films, an image is taken at 285.15 eV, where the domains of PS exhibit the greatest brightness (Figure 2.11). Typically, the dwell time of these images are approximately 2-5 s long to obtain a high signal to noise ratio.

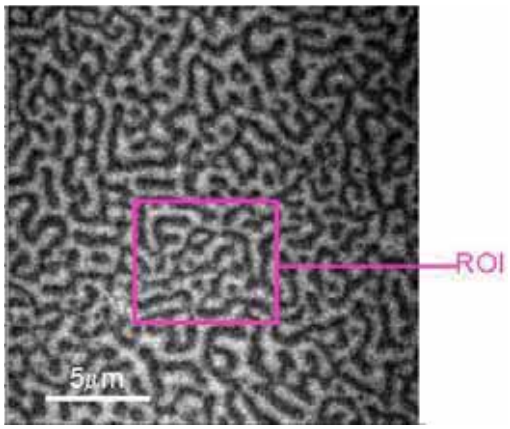

Figure 2.11: (left) Image (30 x 30 μm) of a PS-PLA 40:60 film annealed 6 h at 70 °C. Bright areas correspond to pixels high in PS content. Pink box denotes the area of interest selected.

Next, an area of interest (AOI) rectangle is defined within the 30x30 μm image. This rectangle determines the area where a stack is recorded. A stack is composed of images collected in the same AOI at varying photon energies. For the C 1s edge, typically 22 images are collected ranging from 282 – 292 eV with a 1-2 second duration (Figure 2.12). A fast shutter (0.1s) blocks the X-rays during the photon energy step to minimize radiation damage. Although a stack can be collected at the full field of view (30x30 μm), this resulting stack is very large (~100MB). Thus, smaller stacks of ~ 5x5 μm are collected instead, although the full field of view is illuminated (and damaged) during the stack collection.

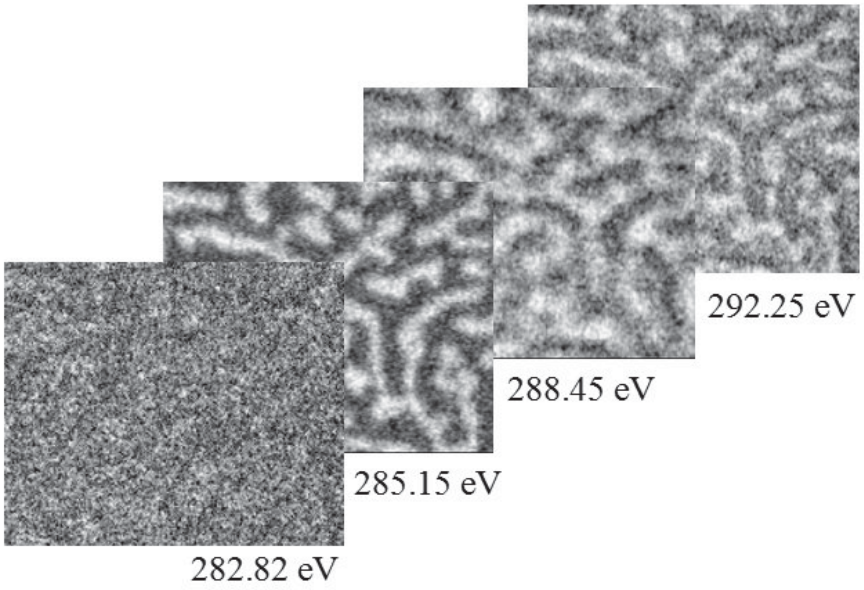

Figure 2.12: Forming a stack: images are taken at several photon energies and combined.

For this first stack, the intensity is averaged for each image collected at the different energies to obtain a 1-dimension NEXAFS spectrum (ie. graph of average intensity vs. photon energy). This spectrum is useful for obtaining the energy calibration. Since the X-PEEM energy scale changes depending on the type of polarized light or the position of the sample relative to the "exit slit", the instrumental energy scale was usually in error. Thus the experimental spectra were calibrated by assigning the C 1s $\rightarrow \pi^*_{C=C}$ transition of PS to 285.15 eV.

The sample stage is mounted on two x and y micrometers (Figure 2.8), and to move the sample position for the next image/stack pair, the sample is physically moved 200 μm away from a damaged area. This procedure is repeated to obtain 5-8 stacks at the C 1s edge.

Since protein is the only species in this thesis which contains nitrogen, the N 1s edge is the most sensitive edge for mapping protein. However, the phase segregated polymer does not show any chemical contrast since neither PS nor PLA contains nitrogen. Thus, combining C 1s and N 1s stacks collected in the same area allows for detection of both the substrate as well as the adsorbing protein (see chapter 4).

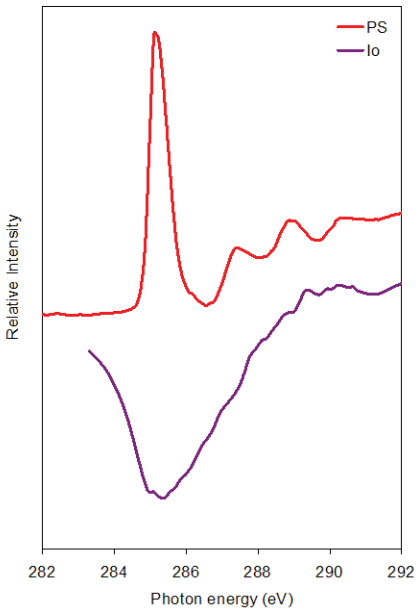

Figure 2.13: C 1s spectrum of PS (red) compared to the I_0 (purple) obtained from a clean HF-etched silicon chip.

Finally, C 1s and N 1s stacks were obtained from a piece of clean, HF-etched silicon to obtain an external I_0. The I_0 spectrum typically exhibits a dip in the C 1s spectrum around ~285 eV which arises from carbon contamination of the beamline optical components (e.g. gratings) (Figure 2.13) [82]. Division of the stack by the I_0 removes both the substrate and carbon dip contribution from the collected stack. In addition, a correction is made for the spectroscopic response of the phosphor which converts X-rays to visible light. The detection is a bolometric effect so that the detection sensitivity varies linearly with photon energy.

2.1.8 Data Processing

A flowchart summarizing the data processing steps is shown in Figure 2.14. All data processing was performed with the aXis2000 software package [83].

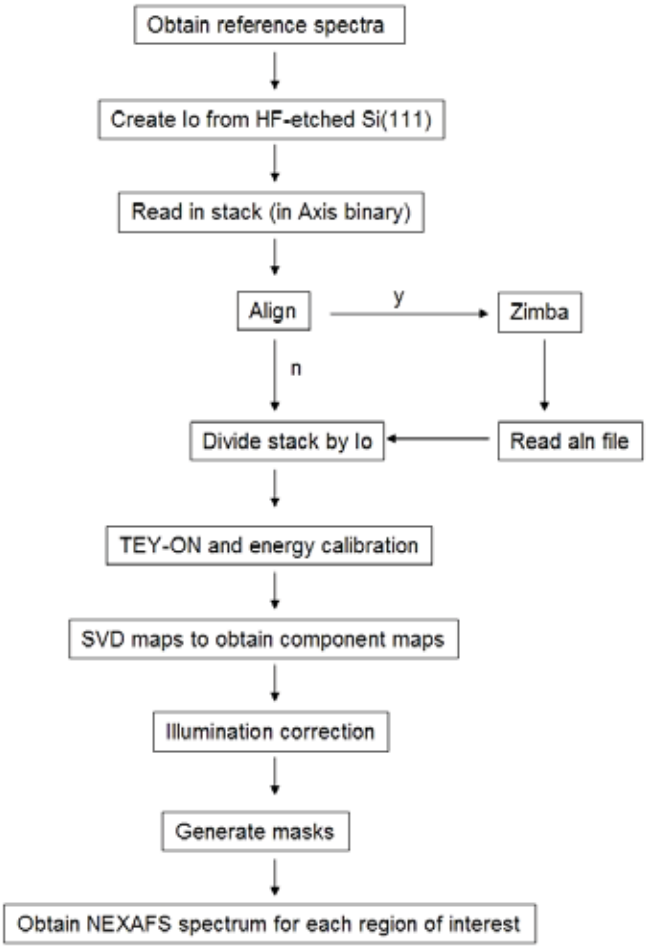

Figure 2.14: Flow chart for X-PEEM2 data analysis.

Step 1: Ensure that all reference NEXAFS spectra have been collected and normalized to the theoretical intensity expected for 1 nm at bulk density.

Step 2: For the C1s stack collected for the clean HF-etched silicon chip, the data from the X-PEEM microscope is read into the aXis2000 program. Depending on the field of view,

usually 20 nm/pixels are defined with a bin of 2. Extract the average NEXAFS spectrum from the stack. This spectrum is then corrected for the photoabsorption cross section of silicon and the bolometric response of the detector. This is saved as the I_0 spectrum.

Step 3: A data stack (ie. HSA/PS-PLA) from the ALS is converted in aXis2000, with 20 nm/pixels and a bin of 2. This stack is read into the Zimba program of aXis2000 and is automatically aligned. The amount of shifting of each pixel during alignment is saved as an ".aln" file.

Step 4: The converted stack and alignment shifts are read into the aXis stack processing widget. The stack is then divided by the I_0 spectrum obtained from Step 2. The "total electron yield" button must be clicked for the X-PEEM data. And at this point, the energy scale can be calibrated by assigning the C 1s $\rightarrow \pi^*_{C=C}$ transition of PS to 285.15 eV.

Step 5: Each pixel of the stack is fit to reference spectra (e.g. PS, PLA and HSA) using singular value decomposition (SVD) to obtain component maps for each species. (Figure 2.15).

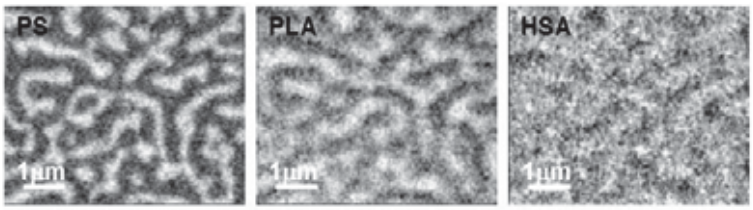

Figure 2.15: Component maps of PS, PLA and HSA. The areas that are high in intensity correspond to that particular component.

Step 6: Often the illumination of the stack obtained from X-PEEM is skewed. To fix this problem, the three component maps and the residual are summed together and then

heavily smoothed to obtain an image without spatial features but retains the illumination (Figure 2.16). Then each component map is divided by the skewed illumination image.

Step 7: A color-coded composite image to visualize spatial correlations is generated using red, green or blue for each component. These maps can be displayed in two ways: (1) **absolute**, which preserves the thickness information and (2) **rescaled**, where the intensity of each component is mapped to the full 0-256 color range, which is useful for localizing each component (Figure 2.17).

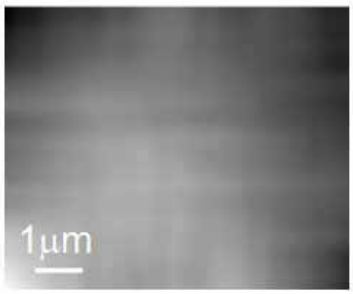

Figure 2.16: Illumination correction image.

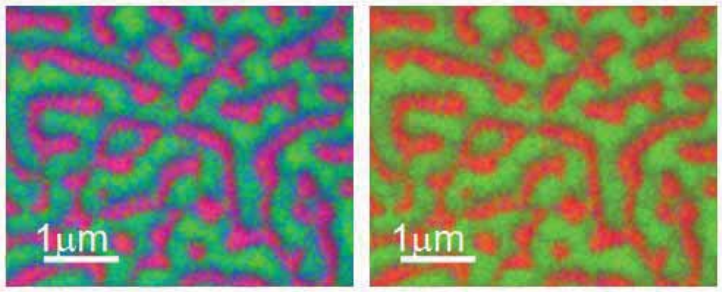

Figure 2.17: Rescaled and absolute images of PS-PLA 40:60 films annealed 6h at 70 °C.

Step 8: A threshold mask is applied to each component map to obtain region of interest (ROI) pixels corresponding to the two polymer regions or the interface (Figure 2.18). In this thesis, the interface is defined as the boundary between the two blend components where intermixing of the two polymers is greatest. At the interface, there may also be some changes in topography (ie, step height in PS-PMMA ~ 4nm, PS-PLA ~ 35-90 nm). As defined by the masking process, this “interface” region occupies a 100-200 nm band at the phase boundary.

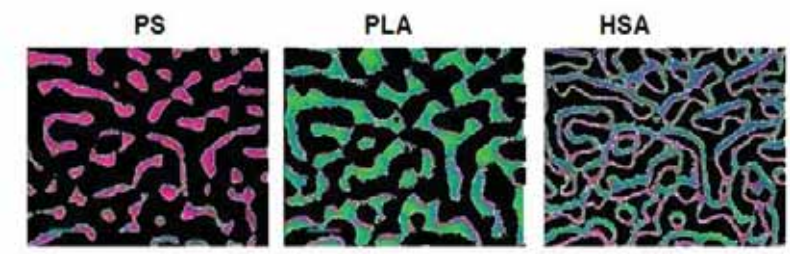

Figure 2.18: Region of interest masks obtained for the PS region, PLA reigon, and interface region.

Step 9: The stack is read into aXis binary and the entire stack divided by the illumination image. Next the masked ROI images are read in to aXis binary to generate 1-dimensional NEXAFS spectra that correspond to PS-rich, PLA-rich or interface regions (Figure 2.19).

Step 10: These 1-D NEXAFS spectra often have pre-edges that are not at zero, which may cause fitting errors. The pre-edges of all the extracted NEXAFS spectra and the reference spectra are set to zero prior to fitting. Next, the extracted NEXAFS spectra corresponding to PS-rich, PLA-rich or interface areas are fitted with the reference spectra to obtain quantitative results (Figure 2.19b).

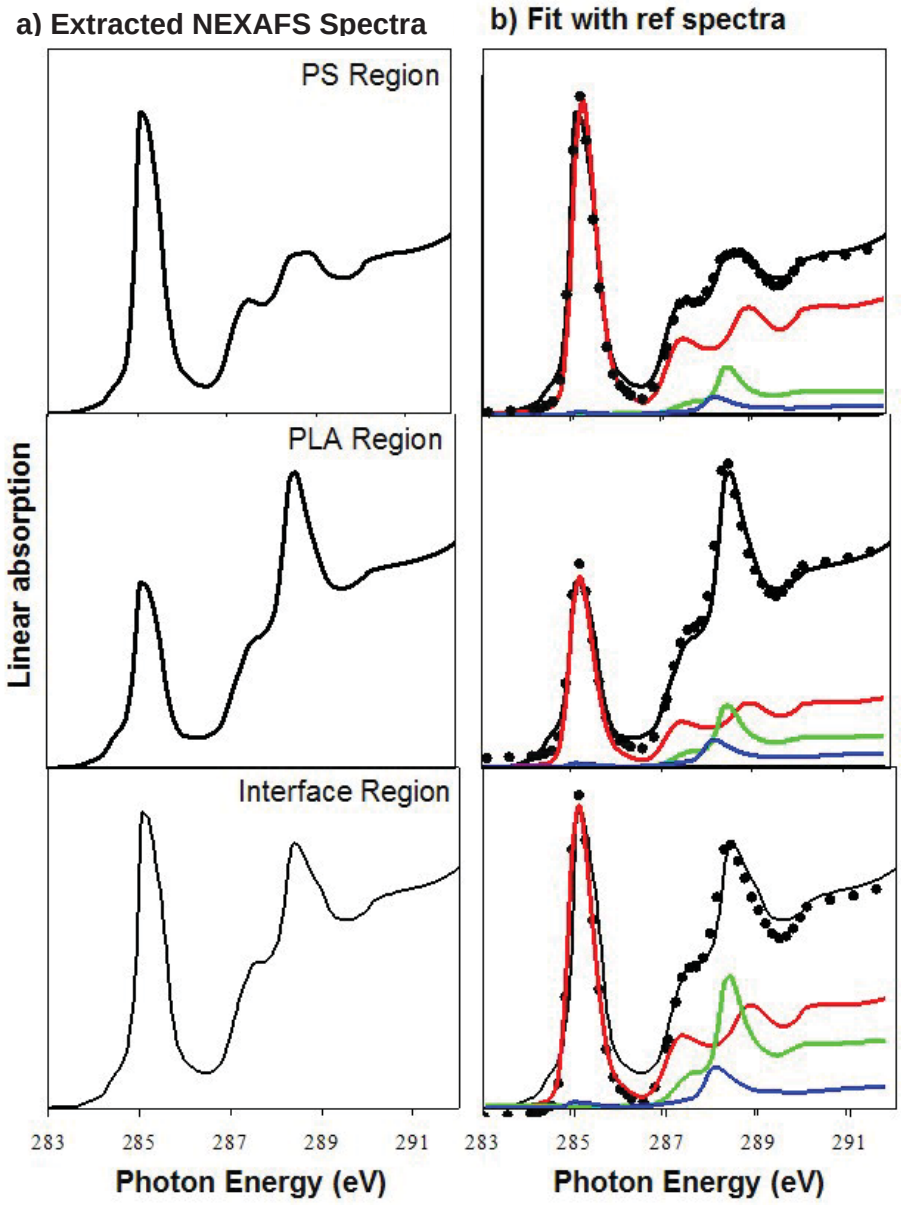

Figure 2.19: a) Extracted NEXAFS spectra from the PS-rich, PLA-rich and interface regions. b) Quantitative results obtained from fitting of the PS, PLA and HSA reference spectra to the extracted NEXAFS spectra from each of the three regions. Solid line – extracted spectrum, dots – fit, PS is red, PLA is green and HSA is blue.

Step 11: Steps 3-10 are repeated for all other C 1s stacks and then the quantitative results are averaged to obtain higher statistical precision and an estimate of the uncertainty. For

N 1s stacks, reference spectra and I_0 must be generated for the first stack, but then steps 3-10 can be repeated for all other N 1s stacks.

2.2 Atomic Force Microscopy (AFM)

The research group of Binnig at IBM Zurich Research Laboratory developed the scanning tunneling microscope (STM) in 1980-1981 [84]. This was the first microscope in the scanning probe microscopy (SPM) family which allowed atomic scale imaging. While the STM technique is limited to conducting samples, this type of microscopy led to the development of other tip-to-sample interrogation techniques including the most commonly used SPM imaging system, the atomic force microscope (AFM) in 1986 [84]. One major advantage of AFM is that it can be used to probe both insulating and conducting materials. AFM is sensitive to the attractive and repulsive forces between the tip and the surface, which result in measurable changes in the position of the cantilever [84].

Figure 2.20 shows the schematic of a typical AFM. A sharp tip attached to a flexible cantilever is used to scan over the surface of a sample. A piezoelectric scanner moves the sample with sub-nanometer movements in three dimensions when a voltage is applied [84]. The tip is brought into contact with the surface and then raster scanned. The surface topography causes the cantilever to deflect, and by using a laser light reflected off the back of the cantilever onto a position-sensitive photodiode detector, a line-by-line image of the deflection is obtained [84].

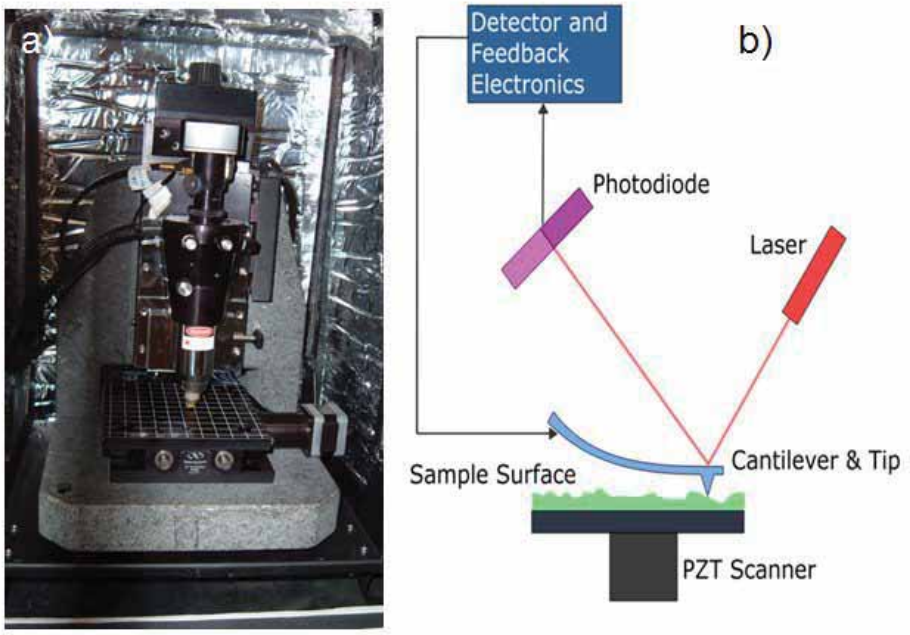

Figure 2.20: left) Photo of the Quesant 250 AFM in ABB-332. right) Schematic of a typical AFM.

There are several AFM modes of operation. The most common method is contact mode (C-AFM), where the AFM tip is in constant repulsive contact with the surface [84]. In constant-height mode contact mode, the deflection of the cantilever is recorded during raster scanning with an open feedback loop, thus, the deflection is proportional to changes in the surface topography. In this mode, the tip deflection is caused by repulsive forces between overlapping electron orbitals of the tip atoms with the surface atoms [84].

The AFM can also operate under non-contact mode (NC-AFM). In NC-AFM, the oscillating tip is never in contact with the surface, with the gap between the tip and surface ~ 10-100 Å and an oscillation amplitude ~ 50 Å [84]. In NC-AFM, the cantilever is sinusoidally excited close to its main resonant frequency. Thus, only long-range attractive forces change the amplitude, frequency or phase of the cantilever. These

changes are monitored by the feedback loop and give rise to topographical or chemical sensitive phase images [84].

In this thesis, all AFM images were collected with a Quesant Q-scope 250 (Quesant Instruments, Ambios Technology, Santa Cruz, CA), operated in non-contact mode. Standard non-contact silicon cantilevers from Quesant were used. Phase and height mode images were collected simultaneously at a scan rate of 1.8-2.0 hertz under ambient conditions.

2.3 ^{125}I Radiolabeling

A label may be any substance which can be uniquely identified by simple, direct methods from the background substrate, with the most common label being a radioactive isotope [85]. The nucleus of any atom holds both protons and neutrons with the number of protons determining the atomic number. However, the number of neutrons can change, which gives rise to variations of atomic mass. Isotopes consist of atoms with the same number of protons, but different neutrons [85].

The nucleus of many isotopes is unstable and can spontaneously decay to more stable states, releasing energy, particles, or non-particulate electromagnetic vibrations. For example, ^{125}I decays as γ-rays (35 keV) and X-rays (4 or 28 keV) [86]. The rate of decay is measured by the half-life, or the time it takes for 50% of the radioisotope to decay, and for ^{125}I, it is 60 days.

The addition of iodine to certain amino acid residues has been known since the 1940s [87]. Under mild conditions, the amino acids tyrosine, cysteine and histidine are

reactive with iodine, although under harsh conditions, tryptophan and methionine can also react with iodine [87]. The most common method of preparing ^{125}I radiolabeled protein is by the chloramine-T method [87]. Dilute solutions of protein at pH 7.0 spontaneously react with I_2. Sodium metabisulfite is added immediately after 15 seconds to quench the reaction. Iodinated protein deteriorates rapidly and should be used within 24h of synthesis [87].

For our radiolabelling experiments, we use the "Iodogen" technique where a sparingly soluble oxidizing agent such as 1,3,4,6-tetrachloro-3a,6a-diphenyl-glycouril is evaporated to the reaction vessel wall via methylene chloride [85]. Then the protein and ^{125}I (ICN Biomedicals) is added. The reaction is terminated upon removal from the reaction vessel and does not require a reducing agent. The radiolabelling experiments conducted in this thesis were performed by Rena Cornelius. The author of this thesis was not present during the experiments since she was not properly trained to handle radioactive materials. For more details on the ^{125}I radiolabelling procedure, please see reference [88].

The detection and quantification of a radioactive isotope is typically obtained via a scintillation counter [85]. When ionizing radiation (such as a γ-ray) strikes the scintillator, it emits a flash of light directly proportional to the energy of the radiation [85]. The light is detected by a photomultiplier tube which converts the energy to electrical pulses. The electrical pulse can be used to count the isotope with minimum interference from the background [85].

2.4 Sample Preparation

2.4.1 Materials

Polystyrene (MW = 104K, δ 1.05), polylactide (MW 30K, δ 1.33), and poly(methyl methacrylate) –b– polyacrylic acid (MW = 41–b–10 K, δ 1.2) were obtained from Polymer Source Inc. (δ is polydispersity defined as a measure of the distribution of molecular mass in a given polymer sample). Polyethylene oxide (MW 600K) and pentaerythritol triacrylate were purchased from Sigma Aldrich. All polymers and PETA were used as received.

The polydispersity of PEO was not stated on the sample from Sigma Aldrich. We are in the process of determining polydispersity. For high MW polymer strands, the polydispersity should not impact the films since they are ultimately crosslinked. The presence of lower MW polymer strands may reduce protein adsorption by having greater flexibility and thus extending more loops into solution to prevent protein adsorption.

Human serum albumin (HSA) was purchased from Behringwerke AG, Marburg, Germany, and found to be homogeneous as judged by sodium dodecyl sulphate polyacrylamide gel electrophoresis (SDS-PAGE). Protein solutions were prepared from DDI water or buffer, and the pH was adjusted with HCl or NaOH for pH studies. The SUB-6 peptide (RWWKIWVIRWWR-NH_2), a gift from Professor R. Hancock (UBC) was prepared with 9-fluorenylmethyl carbamate solid-phase synthesis and purified using high-performance liquid chromatography and mass spectrometry. The impurity level in the SUB-6 sample is unknown.

2.4.2 Substrate Preparation

The silicon (111) substrate was purchased from Wafer World Inc. The substrate comes as a large 10cm x 10cm disk and must be cut with a diamond knife to 8mm x 8mm squares for X-PEEM analysis (Figure 2.21). During the cutting procedure, some silicon dust can get onto the surface, which causes charging effects in the X-PEEM. Thus minimizing the dust by blowing compressed air on the surface prior and after cutting with the diamond knife is a key step in preparing a clean substrate.

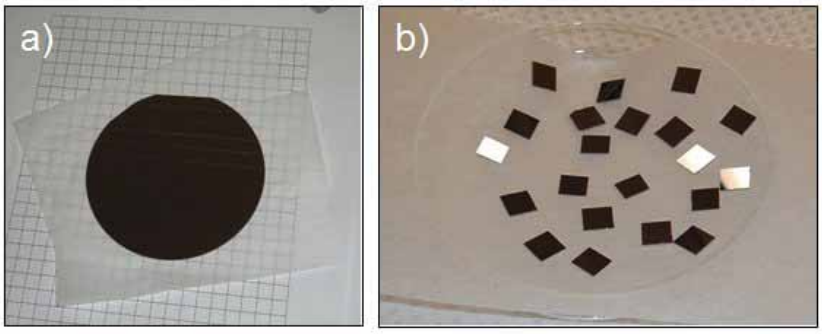

Figure 2.21: (left) Cutting a 10 cm x 10 cm silicon (111) wafer into 0.8 x 0.8 cm chips.

However, organic material from the compressed air causes a noticeable contamination in the NEXAFS spectrum at the C 1s edge. Thus the silicon chips must be cleaned by sonication with trichloroethylene, acetone and methanol, followed by extensive rinsing with doubly deionized water (DDI). Furthermore, each silicon chip must be further examined under the microscope after drying to ensure that there are no dust particles left on the surface.

Polystyrene and either PLA, PEO (with PETA), or PMMA-PAA, (or PEO and PETA – see chapter 5) were dissolved in dichloromethane at varying mass ratios at

different wt% and spun cast at 4000 rpm for 4 s onto the cleaned silicon chips. For the PEO-containing samples, the chips were exposed to a 365 nm UV lamp under flowing nitrogen for 40 min to crosslink the PEO (Figure 2.22 a-b). The UV reactor consists of five RPR Rayonet photochemical reaction lamps positioned ~ 5 cm above the samples. The samples were vacuum annealed at a pressure of ~10^{-4} torr at varying temperatures (Figure 2.22c).

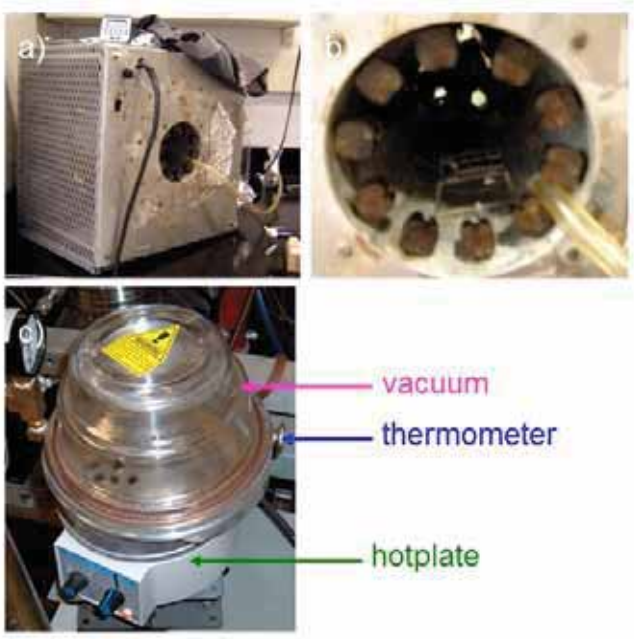

Figure 2.22: a) Dr. Stöver's UV lamp. b) Sample positioned under the UV tubes. A N_2 line is used to cool the sample during crosslinking. c) Photo of the vacuum annealer in ABB-332.

2.4.3 Protein Adsorption

The substrate was placed in a 50 mL beaker and covered with 5 mL of protein or peptide solution. After 20 minutes, the solutions were diluted with at least 50 mL of DDI water (or buffer), vigorously rinsed and the substrate was carefully dried by touching the

edge of the Si wafer with lens paper. The thickness of the spun cast films were measured with AFM via non-contact mode along a scratch made by tweezers.

Most of the protein adsorption experiments performed in this thesis was from DDI water rather than buffer. While it is recognized that buffer is an important component for mimicking in vivo conditions and maintaining the native conformation of the protein, the high salt content from buffer often salts out of the sample and for X-PEEM, can cause charging effects. HSA is one of the few proteins that can be dissolved in DDI water without protein aggregation.

CHAPTER 3: PHASE SEGREGATON IN POLYSTYRENE-POLYLACTIDE BLENDS

The following chapter presents the X-PEEM and AFM characterization of polystyrene-polylactide blend films with respect to mass ratios, polymer weight concentrations and temperature annealing. It was found that for most of the films sampled, PLA segregated to the substrate-air interface. However, phase segregation improved upon annealing. Furthermore, annealing above the glass transition temperature of PLA resulted in a phase inversion where PLA became the continuous phase with PS discrete domains.

Copyright

Author contribution

The author of this thesis contributed to this publication in the following ways: all sample preparation, all acquisition of the AFM data, all X-PEEM data collection, all X-PEEM data analysis, and the first draft of the manuscript. Andreas Scholl provided help with the sample transfer.

Macromolecules **2009**, *42*, 1679−1684

Phase Segregation in Polystyrene−Polylactide Blends

Bonnie O. Leung,[†] Adam P. Hitchcock,*[,†] John L. Brash,[‡] Andreas Scholl,[§] and Andrew Doran[§]

BIMR, McMaster University, Hamilton, ON, Canada L8S 4M1; School of Biomedical Engineering, McMaster University, Hamilton, ON, Canada L8S 4M1; and Advanced Light Source, Berkeley Laboratory, Berkeley, California 94720

Received September 25, 2008; Revised Manuscript Received January 13, 2009

ABSTRACT: Spun-cast films of polystyrene (PS) blended with polylactide (PLA) were visualized and characterized using atomic force microscopy (AFM) and synchrotron-based X-ray photoemission electron microscopy (X-PEEM). The composition of the two polymers in these systems was determined by quantitative chemical analysis of near-edge X-ray absorption signals recorded with X-PEEM. The surface morphology depends on the ratio of the two components, the total polymer concentration, and the temperature of vacuum annealing. For most of the blends examined, PS is the continuous phase with PLA existing in discrete domains or segregated to the air−polymer interface. Phase segregation was improved with further annealing. A phase inversion occurred when films of a 40:60 PS:PLA blend (0.7 wt % loading) were annealed above the glass transition temperature (T_g) of PLA.

1. Introduction

Polylactide (PLA) or poly(lactic acid) is studied extensively since it is valuable in biomedical and pharmaceutical applications due to its biodegradable and biocompatible nature.[1−3] However, the brittleness of PLA impedes its development for large-scale commercial use.[4] Thus, PLA has been blended with a variety of materials such as natural fibers,[5,6] plasticizers,[7] and synthetic, nonbiodedgradable polymers to enhance physical properties such as elasticity[8] and tensile strength.[9] In particular, PLA combined with polystyrene (PS) has been investigated as a potential bioblend with proposed applications in materials packaging and tissue engineering.[10]

PS−PLA block copolymers have recently been found to exhibit a rich variety of nanopatterns such as cylinders[11−13] and cocontinuous structures[14] which form during phase segregation of PS and PLA and arise from the immiscibility of the two polymers.[15] Selective removal of either component gives rise to ordered nanochannels suitable as catalytic supports or scaffolds in tissue engineering. Improving the physical properties of these materials depends on control of the interface between the two polymers which controls its microstructure.[14] Thus, characterization of the morphology of PS-*b*-PLA block copolymers, as well as PS−PLA blends, remains key in the development of novel, high-performance, PS−PLA-based materials.

We are using soft X-ray spectromicroscopy to study phase segregation in spun-cast thin films of PS−PLA blends. Our techniques provide quantitative information on the composition of these polymers. Several studies have utilized near-edge X-ray absorption fine structure (NEXAFS) spectra obtained in an X-ray photoemission electron microscope (X-PEEM) or scanning transmission X-ray microscope (STXM) to characterize immiscible polymer blends.[16−21] Our research group has previously used X-PEEM to characterize spun-cast films of phase-segregated polystyrene (PS)−poly(methyl methacrylate) (PMMA) with respect to polymer molecular weights and annealing times and temperatures.[22] The chemical sensitivity, particularly at the C 1s edge, combined with the near-surface sensitivity of X-PEEM, provides quantitative characterization of the composition and morphology in the outermost ∼10 nm of the film.

The aim of this work is to visualize and quantitatively analyze different morphologies produced at the surfaces of PS−PLA films by varying mass ratio, total polymer concentration, and annealing times. This study is part of an effort to develop phase-segregated PS−PLA films with surface microstructure in the submicron range as candidate semibiodegradable biomaterials. A subsequent paper will report our investigations of protein adsorption on the more promising PS−PLA substrates.[23]

2. Materials and Methods

2.1. Materials. Polystyrene (MW = 104K, δ = 1.05) and polylactide (MW = 33K, δ = 1.33) were obtained from Polymer Source Inc. and used as received. The samples were of high purity, as confirmed by proton NMR. Varying ratios of the two polymers were spun-cast (4000 rpm, 40 s) from 1.0, 0.7, and 0.4 wt % dichloromethane solutions onto clean 1 × 1 cm native oxide silicon wafers (Wafer World, Inc.) and degreased with trichloroethylene, acetone, and methanol, followed by rinsing with doubly deionized water. The PS−PLA substrates were annealed at 45 °C (1 and 6 h) and 70 °C (1 h) in a vacuum oven at a pressure ∼10^{-5} Torr, achieved with a cryo-trapped turbo pump.

2.2. Atomic Force Microscopy (AFM). AFM images were collected with a Quesant Q-scope 250 (Quesant Instruments, Ambios Technology, Santa Cruz, CA), operated in noncontact mode. Standard noncontact silicon cantilevers from Quesant were used. Phase and height mode images (10 × 10 μm) were collected simultaneously at a scan rate of 1.8−2.0 Hz under ambient conditions.

2.3. STXM. A scanning transmission X-ray microscope (STXM) was used to collect high-quality reference spectra of PS and PLA. The STXM operates in transmission mode and offers slightly better energy resolution (0.1−0.2 eV) compared to X-PEEM (0.4−0.5 eV); however, similar NEXAFS line shapes are obtained from both methods. The STXM data were collected on beamline 5.3.2 at the Advanced Light Source (ALS) in Berkeley, CA.[24,25] Typically, solvent-cast samples with thickness below 100 nm were analyzed by collecting micrometer-sized stacks. Image sequences[26] were used in homogeneous areas to minimize radiation damage. An image at a damage-sensitive energy (288.5 eV)[27] was recorded after each spectral measurement to monitor damage. Only results from measurements with negligible (<10%) damage were used analytically.

2.4. X-PEEM. All X-PEEM measurements were performed at the ALS on the PEEM-2 instrument on beamline 7.3.1 using elliptical right circularly polarized light (70−80%). Detailed accounts of the experimental apparatus, beamline setup, and

* Corresponding author. E-mail: aph@mcmaster.ca.
† BIMR, McMaster University.
‡ School of Biomedical Engineering, McMaster University.
§ Berkeley Laboratory.

10.1021/ma802176b CCC: $40.75
Published on Web 02/16/2009

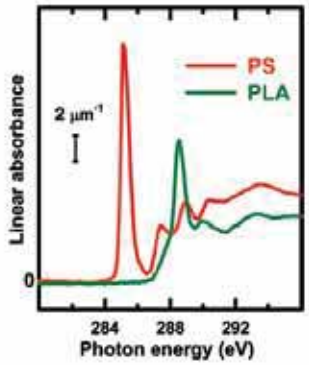

Figure 1. C 1s X-ray absorption spectra of polystyrene (PS, red) and polylactide (PLA, green), as recorded in STXM. The spectra are plotted on an absolute linear absorbance scale, after subtraction of a linear background to isolate only the C 1s signal.

instrument optics have been presented previously.[28] In short, photoelectrons and secondary electrons ejected by absorption of the monochromatic X-rays are accelerated into an electrostatic imaging column, where the spatial distribution is magnified and detected by a CCD camera. X-PEEM is a surface-sensitive technique with a sampling depth (1/e) of 4 nm for polymers,[29] with the integrated signal sampling the top 10 nm of the sample.

A 100 nm thick Ti foil was used as a second-order light filter. To minimize radiation damage, a fast shutter (0.1 s) was used. This reduced the X-ray exposure by 50% by blocking the beam during the time required to transfer images from the CCD camera and to step the photon energy. The incident flux was reduced to about 10% of the full intensity by masking the beam upstream of the monochromator. A limited number of energies (23 in C 1s) and a short exposure time (1 s) per image were used as other ways to minimize radiation damage. The field of view was approximately 20×20 μm.

2.5. X-PEEM Chemical Mapping and Quantitative Analysis. The reference C 1s spectra for PS and PLA are presented in Figure 1 on a quantitative linear absorbance scale. The two species are easily differentiable. PS is characterized by an intense C 1s $\rightarrow$ $\pi^*_{C=C}$ transition at 285.15(3) eV while PLA exhibits a strong C 1s $\rightarrow$ $\pi^*_{C=O}$ transition at 288.53(3) eV.

All quantitative analyses were performed with the aXis2000 software package.[30] The C 1s image sequences were aligned (if needed), normalized to the ring current, and divided by the I_0 spectrum obtained from a clean HF-etched Si(111) chip. Next, the spectrum was corrected for the absorption of Si with a linear energy term representing the bolometric response of PEEM detection. Each stack was calibrated by assigning the peak of the C 1s $\rightarrow$ $\pi^*_{C=C}$ transition of PS to 285.15 eV.

The spectrum at each pixel was fit to linear combinations of the PS and PLA reference spectra using singular value decomposition (SVD), which provides an optimal solution for the analysis of highly overdetermined data sets.[31,32] The fit coefficients at each pixel provide component maps which are the spatial distribution of each component (Figure 2). Nonuniform illumination was corrected by dividing each component map by a heavily smoothed version of the sum of all component maps. Since X-PEEM samples ~10 nm into the surface, the intensity scale of the sum of the component maps was set to 10 in order to give estimates of the thickness in nanometers of each component in the sampled region.[29]

Next, a threshold mask was applied to the PS and PLA component maps to identify those pixels corresponding to PS-rich or PLA-rich areas (Figure 3a,b). Threshold levels were adjusted manually to a value which isolated only the domains of common spectral characteristics as determined by the color-coded composite maps. The average spectra extracted from the PS-rich and PLA-rich regions were further modified by setting the pre-edge region

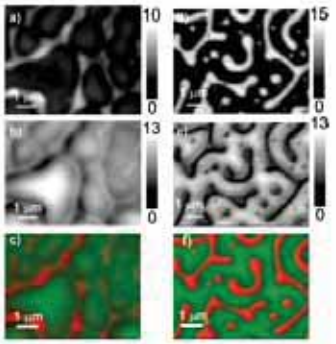

Figure 2. (left) Component maps of (a) PS and (b) PLA, derived from C 1s image sequences measured from an as-spun 40:60 PS:PLA (1 wt %) film (gray scale is thickness in nanometers). (c) Rescaled color composite map (red = PS, green = PLA). (right) Component maps of (d) PS and (e) PLA, derived from C 1s image sequences measured from 40:60 PS:PLA (0.7 wt %) film annealed 1 h at 70 C. (f) Rescaled color composite map. In (c) and (f), the relative contribution from red has been increased by 40% and that of green has been decreased by 20% in order to visualize more clearly the continuous domain, which is PS-rich in (c) and PLA-rich in (f).

to zero intensity, followed by least-squares fit to the same PS and PLA reference spectra used to generate the component maps (Figure 3c,d). Several stacks were obtained for each sample and the compositional results from these independent repeat measurements were averaged to yield the final quantitative results. The uncertainties cited in Table 1 are the standard deviations from these multiple determinations.

3. Results

3.1. Optimization of a PS−PLA Blend System. *3.1.1. Polymer Weight Ratios.* Four solutions with PS:PLA w/w ratios of 20:80, 40:60, 60:40, and 80:20 (1% total polymer weight) were dissolved in dichloromethane and spun-cast on Si(111). The AFM phase mode micrographs of these samples are displayed in Figure 4a−d. AFM revealed interesting variations in the microstructure at the surface, particularly for the 40:60 and 60:40 PS:PLA ratios. Although AFM provides excellent height resolution at the surface (<1 nm), it does not have any intrinsic chemical sensitivity, and domain composition cannot be determined without film destruction. Typically, AFM studies of binary or ternary polymer systems use either a complementary technique with chemical sensitivity (i.e., XPS, TOF-SIMS) or the selective removal of one component via washing with an appropriate solvent.[33−35] Thus, chemical characterization of these phase-segregated films required an additional technique, in this case X-PEEM.

The color-coded composite maps of the 40:60 and 60:40 PS:PLA ratio films derived from the X-PEEM C 1s data (Figure 4e−h) are a green color, indicating that for both ratios the surface is dominated by PLA. Although the AFM micrographs strongly suggested morphologies indicative of phase segregation, X-PEEM unambiguously reveals that there is a large excess of PLA in the near-surface region sampled (~10 nm) relative to the solution composition.

The spectra for the PS-rich and PLA-rich regions were extracted from the image sequences for 40:60 and 60:40 PS−PLA films using threshold masking,[36] and these spectra were then analyzed to quantify the composition of the discrete and continuous domains (Table 1). The PS region was compiled from the pixels with the most red color and is considered "PS-rich" relative to the PLA region. For the 40:60 PS:PLA ratio, the PLA-rich region has a composition of 86(5) vol % PLA and 14(5) vol % PS. In contrast, the PS-rich region consists of

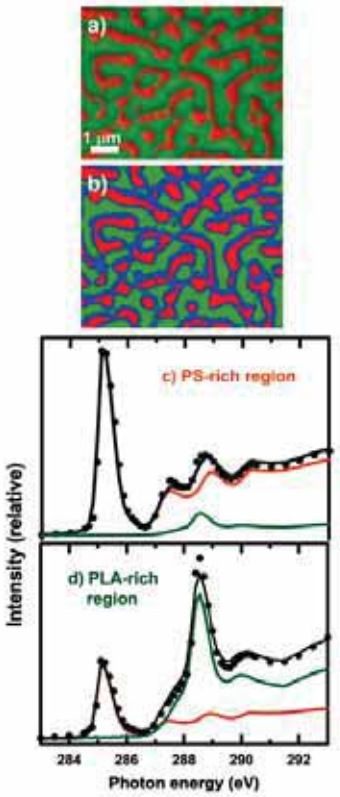

Figure 3. (a) Sample X-PEEM color-coded composite map (nonrescaled) derived from a singular value decomposition (SVD) analysis, using the PS and PLA reference spectra (Figure 1) of a C 1s image sequence (23 energies) recorded from a PS−PLA blend thin film spun-cast from a dichloromethane solution with a total loading of 0.7 wt % polymer in a 40:60 PS:PLA ratio, and annealed 6 h at 45 C. (b) Mask used to extract spectra of specific regions. Red denotes PS-rich regions, green denotes PLA-rich regions, defined by threshold masking the PS and PLA component maps. The remaining blue pixels represent areas with intermediate compositions which were not included in the quantitative analysis. (c) Curve fit of the average C 1s spectra of the PS-rich region (data, dots; fit, black line; components, colored lines). (d) Curve fit of the average C 1s spectra of the PLA-rich region (same color coding).

only 40(5) vol % PS with PLA contributing over 60(5) vol % of the signal. Analysis of the PS:PLA 60:40 blend shows even more anomalous results with an ~80(5) vol % of PLA found in both the PS and PLA regions. The large percentage of PLA in the near surface region may indicate the presence of a relatively thick (~8.0(5) nm) layer of PLA at the substrate surface.

PLA has also been found to segregate at the air−polymer interface in poly(sebacic anhydride) (PSA)−PLA blends.[37] In that case, the segregation was attributed to differences in the surface free energies of the polymer components, with the lower surface free energy polymer segregating to the surface.[37] However, the surface free energies of PS and PLA are very similar ($\gamma_{PLA} = 40.2$ mJ/m^2 and $\gamma_{PS} = 41.0$ mJ/m^2 [38,39]). Thus, it is more likely that the presence of excess PLA at the surface is due to the higher solubility of PLA in dichloromethane, such that the PLA stayed dissolved longer in the liquid phase and hence developed an overcoat layer.[40]

3.1.2. Total Polymer Concentration Dependence. The 40:60 PS:PLA composition was selected for dilution experiments since less PLA was detected in the X-PEEM study. The total percentage of polymer relative to the solvent was decreased from 1 to 0.7 wt % and then to 0.4 wt %, while maintaining the composition at the 40:60 ratio. AFM images (Figure 5a−c) show that the film cast from a 0.7 wt % solution exhibits a classic dispersed droplet morphology. Further dilution to 0.4 wt % produced a film with "blotchy" spots, likely corresponding to the same domains found for the 0.7 wt % film (Figure 5c).

The X-ray spectromicroscopy analysis of the 0.7 wt % PS:PLA 40:60 film reveals that phase segregation is incomplete. Although the PLA-rich region contains over 80(5) vol % PLA, PLA is also the dominant component in the PS region, contributing 60(5)% of the total signal (Figure 5d−f). In contrast, X-PEEM imaging of the 0.4 wt % 40:60 PS:PLA film shows a much more "red" color, corresponding to an increased signal from PS. The boundaries of the domains of PLA (green) are not sharp, which suggests that the PLA domains may be quite thin, as expected from the very dilute concentration of the polymer solution.

The 40:60 PS:PLA film showed negligible change in the PS fraction at the surface upon dilution from 1.0 to 0.7 wt % (Table 1). In fact, a fairly large fraction of PLA still exists in both the PS and PLA regions. In the PLA region, the PS fraction was 14(5)% in the 1.0 wt % to 19(5)% in the 0.7 wt % polymer solutions, which are the same values within experimental error. Upon further dilution of the solution to 0.4 wt %, the PS-rich regions now contain a stronger PS signal (75(5)%) while the PLA-rich region also shows a strong PS signal. Interestingly, the quantitative analysis of the three polymer concentrations (1, 0.7, and 0.4 wt %) indicates that the PS fraction increases upon dilution. One possible explanation may be that X-PEEM is detecting a layer of PS that exists under the PLA domains, leading to a more "red" color. Still, the quantitative X-PEEM results show that PS and PLA are not completely phase segregated.

3.1.3. Effect of Temperature. The morphology of a polymer blend can change significantly after annealing. For films with dispersed droplet structure, coarsening of the droplets is expected to occur from coalescence. Annealing also provides a means for driving the system toward its thermodynamic equilibrium, which in this case should be complete phase segregation of the PS and PLA. However, as we have annealed our films relatively gently it is likely that the observed changes in spatial distributions are primarily a result of kinetic factors. Typically, distributions in the unequilibrated as-coated system can be strongly affected by different solubilities or substrate affinities. These initial distributions can then be altered by annealing at temperatures in excess of the glass transition (T_g) temperature ($T_g \sim 60$ °C for PLA), where there is greater polymer mobility.[40] Samples of the 40:60 PS:PLA (0.7 wt %) film were annealed at 45 °C for 1 and 6 h and at 70 °C for 1 h. AFM micrographs of the annealed films demonstrate a progressive coarsening effect with increasing temperature, with the domains growing larger laterally and also in height (the surface corrugation increased from 35 nm in the unannealed film to 95 nm in the 70 °C annealed film) (Figure 6).

The X-PEEM results are consistent with the morphology determined by AFM. After annealing for 1 h at 45 °C, the PLA domains have begun to coalesce, which is further enhanced after annealing for 6 h. An additional 5 h of annealing at 45 °C led to further phase segregation of the two polymer components, with the green color of PLA becoming much more pure (Figure 6e). After annealing for 1 h at 70 °C, the domain size coarsens significantly and X-PEEM spectromicroscopy reveals that the discrete domains are now PS-rich (Figure 6f), as opposed to the as-cast and 45 °C annealed films in which the discrete domains are PLA-rich. Figure 2 compares the results from the

Table 1. Composition of PS and PLA (%/pixel) in the PS-Rich and PLA-Rich Regions of PS:PLA Blends with Respect to Polymer Ratios, Total Polymer Concentration, and Annealing (Uncertainty 5%)

		polymer ratios PS:PLA		conc dependence PS:PLA 40:60			annealing PS:PLA 40:60 (0.7%)		
region	component	40:60	60:40	1%	0.7%	0.4%	1 h at 45 °C	6 h at 45 °C	1 h at 70 °C
PS	PS	37	20	37	39	74	80	86	90
	PLA	63	80	63	61	26	20	14	10
PLA	PS	14	8	14	19	58	36	24	23
	PLA	86	92	86	81	42	64	76	77
film thickness[a] (±5 nm)		130	107	130	62	36	89	93	104

[a] Total film thickness (nm) as measured by AFM. Uncertainty estimated from repeat measurements over a scratch made with a sharp tweezer tip.

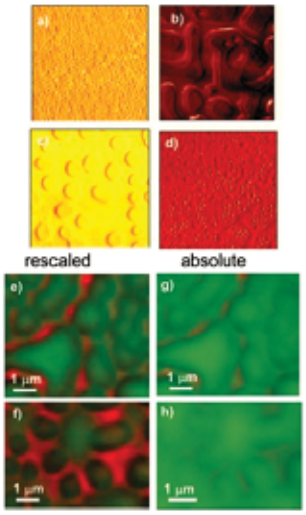

Figure 4. (upper four images) AFM phase mode images of PS:PLA thin film blends spun-cast from a 1 wt % dichloromethane solution loaded with PS:PLA in (a) 20:80 ratio, (b) 40:60 ratio, (c) 60:40 ratio, and (d) 80:20 ratio. All AFM images are 10 μm × 10 μm. (lower four images) X-PEEM color-coded composite map (rescaled) of (e) 40:60 PS:PLA ratio and (f) 60:40 PS:PLA ratio; the relative contribution from red has been increased 40%, and that of green has been decreased by 20% in order to visualize more clearly which is the continuous domain; (nonrescaled) of (g) PS:PLA 40:60 ratio and (h) PS:PLA 60:40 ratio. PS is coded red, and PLA is coded green.

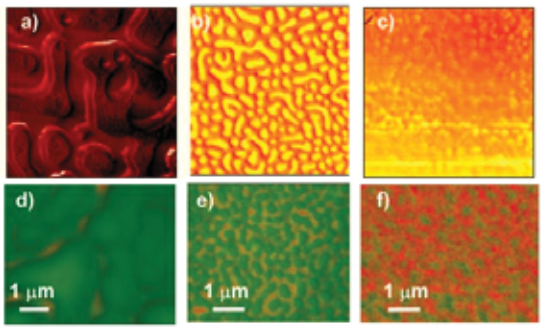

Figure 5. (upper row) AFM phase mode images of 40:60 PS:PLA films spun-cast from dichloromethane solutions with total polymer loading of (a) 1.0, (b) 0.7, and (c) 0.4 wt %. All AFM images are 10 μm × 10 μm. (lower row) X-PEEM color-coded composite maps (nonrescaled) of 40:60 PS:PLA films (d) 1.0, (e) 0.7, and (f) 0.4 wt %. PS is coded red, and PLA is coded green.

as-cast and most strongly annealed samples to emphasize this interesting phase-inversion result.

To verify the phase inversion indicated by X-PEEM, unannealed and 70 °C annealed PS−PLA films were washed with cyclohexane to selectively remove the PS component and re-examined with AFM (Figure 7). Analysis of the unannealed film after the wash showed very similar surface morphology compared to the unwashed film (Figure 7a,b). In contrast, AFM micrographs of cyclohexane-washed 70 °C annealed films (Figure 7c,d) revealed pitted circular holes consistent with the morphology and size of the discrete domains of PS prior to the cyclohexane wash. Thus, both X-PEEM and AFM of the solvent-modified sample consistently indicate that a phase inversion occurs when the as-cast films are annealed above the T_g of PLA.

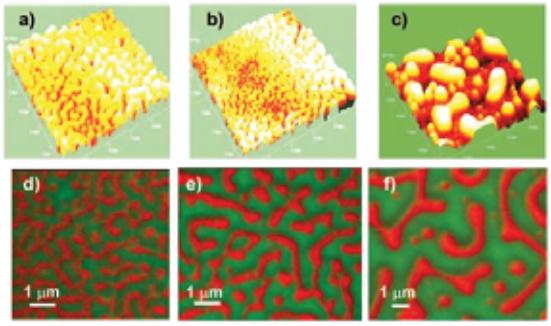

Figure 6. AFM height mode images of 40:60 PS:PLA thin films cast from a 0.7 wt % solution: (a) as-cast, maximum height 35 nm, (b) annealed 1 h at 45 °C, maximum height 45 nm, (c) annealed 1 h at 70 °C, maximum height 90 nm. All AFM images are 10 μm × 10 μm. X-PEEM color-coded composite maps (nonrescaled) of 40:60 PS:PLA thin films cast from a 0.7 wt % films which were (d) annealed 1 h at 45 °C, (e) annealed 6 h at 45 °C, and (f) annealed 1 h at 70 °C. PS is coded red, and PLA is coded green.

4. Discussion

Phase inversion caused by annealing has also been detected in PS−PMMA films spun-cast from toluene or THF. After annealing for 5 min above the T_g of both PS and PMMA (190 °C), a phase inversion was detected.[41] At present, we do not fully understand why the phase inversion in the PS−PLA thin film occurs below the T_g of PS. Phase inversion is known to be affected by volume fraction (ϕ) and structural parameters of the two polymers such as interfacial tension (σ), viscosity (η), and shear stress and strain (or elasticity).[42] In our case, the volume fraction remains unchanged, no shear stress is added, and the interfacial tensions of PS and PLA are very similar. We suggest that, although we are heating below the T_g of PS, there could be changes in the viscosity of the two polymers upon heating, leading to the phase inversion. This may be analogous to previously examined PMMA and poly(ethylene-*alt*-propylene) cryogenic mechanical alloying (CMA).[43] According to the Utracki model, adding one polymer to another polymer in either order causes an increase in the viscosity of the mixtures.[44] In order for a phase inversion to occur, the increasing viscosities must reach the same value. Thus, we speculate that by increasing our annealing temperature to 70

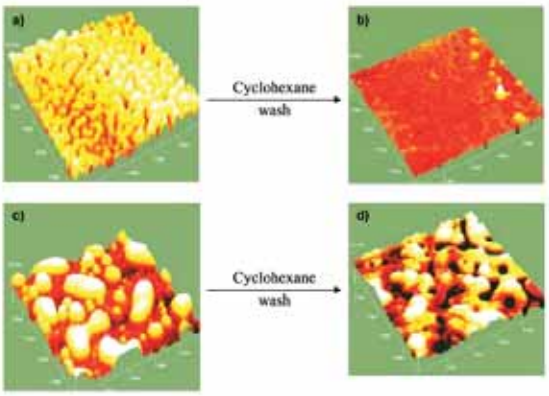

Figure 7. AFM height mode images of 40:60 PS:PLA thin films cast from a 0.7 wt % solution which were (a) as-cast, (b) as-cast, followed by wash with cyclohexane; (c) annealed 1 h at 70 °C, (d) annealed, followed by wash with cyclohexane. All images are 10 μm × 10 μm.

°C, the viscosities of PLA and PS may be similar enough to result in a phase inversion.

The quantitative X-PEEM analyses show there is a considerable increase in the degree of phase separation with annealing, as indicated by greater purity of the discrete and continuous domains. Further enhancement is seen with longer annealing time, especially in the PLA-rich region. However, although higher temperature dramatically impacts the morphology, it does not result in complete phase segregation (Table 1). In the PS-rich region there still remains ~10% of PLA, while in the PLA-rich region there is 20−30% of PS.

For complete phase segregation, annealing at temperatures in excess of the T_gs of both PS and PLA is required. For example, in the case of PS−PMMA thin films which were annealed at 142 °C for 42 h and 170 °C for 8 days, it was found that the morphology obtained at the lower temperature was a transient state which only approached equilibrium upon annealing at higher temperature.[45] In the case of PS−PLA, annealing at a temperature of ~170 °C is impossible due to the low melting point (T_m) of PLA, which is 145−200 °C depending on MW and 145 °C at a MW of 33 000 g/mol.[46−48] Clearly, our PS−PLA films are not fully equilibrated. Yet, even in the case of PS−PMMA, annealing for 8 days at 170 °C did not result in a fully equilibrated sample.[45] Furthermore, since the surface tensions of PS and PLA are very similar, the calculated parameters controlling PS spreading on PLA ($S_{PS} = \gamma_{PLA} - \gamma_{PS} - \gamma_{PS/PLA}$) and vice versa ($S_{PLA} = \gamma_{PS} - \gamma_{PLA} - \gamma_{PS/PLA}$) are both negative, meaning neither polymer can wet the other.[45] Thus, if the sample is thermally equilibrated, PS and PLA should be fully phase segregated in both the bulk and at the surface.[45]

Literature reports of bulk PS−PLA blends examined by differential scanning calorimetry (DSC) and thermal gravimetric analysis (TGA) reveal that the miscibility of the two polymers is highly dependent on polymer composition, with some data sets showing miscibility while others suggesting immiscibility.[10] A Fourier transform infrared photoacoustic spectroscopy (FTIR-PAS) study has detected the formation of n−π bonds between the carboxyl groups of PLA and the benzyl rings of PS, possibly contributing to the incomplete phase segregation.[10] Nonetheless, it is much more likely that small trapped microdomains of the opposite polymer exist at or below the spatial resolution of the X-PEEM, hence giving rise to measurable amounts of the minority component in the quantitative analysis. The existence of small microdomains is evident in the PLA region in the AFM micrographs (Figure 6c).

5. Conclusions

The chemical purity of domains at the surface of a partially phase-segregated PS−PLA blend has been optimized by investigating the morphological and chemical dependence of the thin films with respect to polymer ratio, total polymer concentration, and annealing protocol (time and temperature). While annealing at 70 °C gave a significant improvement in the extent of phase segregation, further optimization of the annealing process is needed in order to achieve 100% phase segregation and eliminate the microdomains. Interestingly, a phase inversion was seen when the films were annealed at temperatures above the T_g of PLA. We interpret this as the result of thermal evolution of the viscosity. Our X-PEEM results show that, in this case, the surface composition suggested by AFM did not correspond to the actual chemical composition, emphasizing the value of an independent verification by a chemically sensitive analysis such as XPEEM or by chemically removing one component from the system.

The annealed PS−PLA blends exhibit a structured surface morphology with distinct surface energies and functional groups. This is required for preferential domain interactions with specific biomacromolecules, a property which might be desired for certain biomaterials applications. In a companion publication we will report our X-PEEM studies of preferential protein adsorption on the best chemically segregated PS−PLA surface.

Acknowledgment. This research is supported by the Natural Science and Engineering Research Council (NSERC, Canada) and the Canada Research Chair programs. X-ray microscopy was carried out using PEEM2 and the polymer STXM at the ALS which is supported by the US Department of Energy under Contract DE-AC03-76SF00098.

References and Notes

(1) Ragauskas, A. J.; Williams, C. K.; Davison, B. H.; Britovsek, G.; Cairney, J.; Eckert, C. A.; Frederick, W. J.; Hallet, J. P.; Leak, D. J.; Liotta, C. L.; Mielenz, J. R.; Murphy, R.; Templer, R.; Tschaplinski, T. *Science* **2006**, *311*, 484–489.
(2) Athanasiou, K. A.; Niederauer, G. G.; Agrawal, C. M. *Biomaterials* **1996**, *17*, 93–102.
(3) Hutmacher, D. W. *Biomaterials* **2000**, *21*, 2529–2543.
(4) Bhardwaj, R.; Mohanty, A. K. *Biomacromolecules* **2007**, *8*, 2476–2484.
(5) Willet, J. L.; Shogren, R. L. *Polymer* **2002**, *43*, 5935–5947.
(6) Li, J.; He, Y.; Inoue, Y. *Polym. Int.* **2003**, *52*, 949–955.
(7) Ljungberg, N.; Wesslen, B. *Polymer* **2003**, *44*, 7679–7688.
(8) Ljungberg, N.; Wesslen, B. *Biomacromolecules* **2005**, *6*, 1789–1796.
(9) Frick, E. M.; Zalusky, A. S.; Hillmyer, M. A. *Biomacromolecules* **2003**, *4*, 216–223.
(10) Mohamed, A.; Gordon, S. H.; Biresaw, G. *J. Appl. Polym. Sci.* **2007**, *106*, 1689–1696.
(11) Olayo-Valles, R.; Lund, M. S.; Leighton, C.; Hillmyer, M. A. *J. Mater. Chem.* **2004**, *14*, 2729–2731.
(12) Zalusky, A. S.; Olayo-Valles, R.; Wolf, J. H.; Hillmyer, M. A. *J. Am. Chem. Soc.* **2002**, *124*, 12761–12773.
(13) Ho, R. M.; Tseng, W. H.; Fan, H. W.; Chiang, Y. W.; Lin, C. C.; Ko, B. T.; Huang, B. H. *Polymer* **2005**, *46*, 9362–9377.
(14) Sarazin, P.; Favis, B. D. *Biomacromolecules* **2003**, *4*, 1669–1679.
(15) Bates, F. S.; Fredrickson, G. H. *Annu. Rev. Phys. Chem.* **1990**, *41*, 525–557.
(16) Slep, D.; Asselta, J.; Rafailovich, M. H.; Sokolov, J.; Winesett, D. A.; Smith, A. P.; Ade, H.; Anders, S. *Langmuir* **2000**, *16*, 2369–2375.
(17) Si, M.; Araki, T.; Ade, H.; Kilcoyne, A. L. D.; Fisher, R.; Sokolov, J. C.; Rafailovich, M. H. *Macromolecules* **2006**, *39*, 4793–4801.
(18) Tzvetkov, G.; Graf, B.; Wiegner, R.; Raabe, J.; Quitmann, C.; Fink, R. *Micron* **2008**, *39*, 275–279.
(19) Hitchcock, A. P.; Stöver, H. D. H.; Croll, L. M.; Childs, R. F. *Aust. J. Chem.* **2005**, *58*, 423–432.
(20) Zhu, S.; Liu, Y.; Rafailovich, M. H.; Sokolov, J.; Gersappe, D.; Winesett, D. A.; Ade, H. *Nature (London)* **1999**, *400*, 49–51.
(21) Ade, H.; Winesett, D. A.; Smith, A. P.; Qu, S.; Ge, S.; Sokolov, J.; Rafailovich, M. *Europhys. Lett.* **1999**, *45*, 526–532.
(22) Morin, C.; Ikeura-Sekiguchi, H.; Tyliszczak, T.; Cornelius, R.; Brash, J. L.; Hitchcock, A. P.; Scholl, A.; Nolting, F.; Appel, G.; Winesett,

D. A.; Kaznacheyev, K.; Ade, H. *J. Electron Spectrosc. Relat. Phenom.* **2001**, *121*, 203–224.
(23) Leung, B. O.; Hitchcock, A. P.; Brash, J. L.; Scholl, A.; Doran, A. Manuscript in preparation.
(24) Warwick, T.; Ade, H.; Kilcoyne, A. L. D.; Kritscher, M.; Tyliszczak, T.; Fakra, S.; Hitchcock, A. P.; Hitchcock, P.; Padmore, A. H. *J. Synchrotron Radiat.* **2002**, *9*, 254–257.
(25) Kilcoyne, A. L. D.; Tyliszczak, T.; Steele, W. F.; Fakra, S.; Hitchcock, P.; Franck, K.; Anderson, E.; Harteneck, B.; Rightor, E. G.; Mitchell, G. E.; Hitchcock, A. P.; Yang, L.; Warwick, T.; Ade, H. *J. Synchrotron Radiat.* **2003**, *10*, 125–136.
(26) Jacobsen, C. J.; Zimba, C.; Flynn, G.; Wirick, S. *J. Microsc.* **2000**, *19*, 173–184.
(27) Wang, J. Ph.D Thesis, Department of Chemistry, McMaster University, Hamilton, Ontario, Canada, **2008**.
(28) Anders, S.; Padmore, H. A.; Duarte, R. M.; Renner, T.; Stammler, T.; Scholl, A.; Scheinfein, M. R.; Stohr, J.; Seve, L.; Sinkovic, B. *Rev. Sci. Instrum.* **1999**, *70*, 3973–3981.
(29) Wang, J.; Li, L.; Morin, C.; Hitchcock, A. P.; Doran, A.; Scholl, A. *J. Electron Spectrosc.* **2009**, doi: 10.1016/j.elspec.2008.01.002.
(30) aXis 2000 is free for noncommercial use. It is written in Interactive Data Language (IDL) and available from http://unicorn.mcmaster.ca/aXis2000.html.
(31) Strang, G. *Linear Algebra and Its Applications*; Harcourt Bracourt, Jovanovich: San Diego, 1988.
(32) Koprinarov, I. N.; Hitchcock, A. P.; McCrory, C. T.; Childs, R. F. *J. Phys. Chem. B* **2002**, *106*, 5358–5364.
(33) Wang, P.; Koberstein, J. T. *Macromolecules* **2004**, *37*, 5671–5681.
(34) Walheim, S.; Ramstein, M.; Steiner, U. *Langmuir* **1999**, *15*, 4828–4836.
(35) Virgilio, N.; Favis, B. D.; Pepin, M.-F.; Desjardins, P.; L'Esperance, G. *Macromolecules* **2005**, *38*, 2368–2375.
(36) L.Li, L.; Brash, J.; Cornelius, R.; and Hitchcock, A. P. *J. Phys. Chem. B* **2008**, *112*, 2150–2158.
(37) Davies, M. C.; Shakesheff, K. M.; Shard, A. G.; Domb, A.; Roberts, C. J.; Tendler, S. J. B.; Williams, P. M. *Macromolecules* **1996**, *29*, 2205–2212.
(38) Ton-That, C.; Shard, A. G.; Teare, D. O. H.; Bradley, R. H. *Polymer* **2001**, *42*, 1121–1129.
(39) Otsuka, H.; Nagasaki, Y.; Kataoka, K. *Sci. Technol. Adv. Mater.* **2000**, *1*, 21–29.
(40) Ton-That, C.; Shard, A. G.; Daley, R.; Bradley, R. H. *Macromolecules* **2000**, *33*, 8453–8459.
(41) Walheim, S.; Boltau, M.; Mlynek, J.; Krausch, G.; Steiner, U. *Macromolecules* **1997**, *30*, 1995–5003.
(42) Steinmann, S.; Gronski, W.; Friedrich, C. *Polymer* **2001**, *42*, 6619–6629.
(43) Smith, A. P.; Ade, H.; Smith, S. D.; Koch, C. C.; Spontak, R. J. *Macromolecules* **2001**, *34*, 1536–1538.
(44) Utracki, L. A. *J. Rheol.* **1991**, *35*, 1615–1637.
(45) Haris, M.; Appel, G.; Ade, H. *Macromolecules* **2003**, *36*, 3307–3314.
(46) Woo, S. I.; Kim, B. O.; Jun, H. S.; Chang, H. N. *Polym. Bull.* **1995**, *35*, 415–421.
(47) Chen, C. C.; Chueh, J. Y.; Tseng, H.; Huang, H. M.; Lee, S. Y. *Biomaterials* **2003**, *24*, 1167–1173.
(48) Ajioka, M.; Enomoto, K.; Suzuki, K.; Yamaguchi, A. *J. Environ. Polym. Degrad.* **1995**, *3*, 225–234.

MA802176B

CHAPTER 4: X-RAY SPECTROMICROSCOPY STUDY OF PROTEIN ADSORPTION TO A POLYSTYRENE-POLYLACTIDE BLEND

The following chapter presents the X-PEEM characterization of human serum albumin (HSA) adsorbed to polystyrene-polylactide (PS-PLA) blend surfaces with respect to surface rugosity in the 35 – 90 nm range and ionic strength. It was found that the topography changes did not affect protein adsorption. X-PEEM revealed that the conformation of HSA increases with increasing ionic strength. These ionic strength experiments were supported by data from ^{125}I-radiolabeling experiments.

Copyright

Author contribution

The author of this thesis contributed to this publication in the following ways: all sample preparation, all acquisition of the AFM data, all X-PEEM data collection, all X-PEEM data analysis, and the first draft of the manuscript. Rena Cornelius performed the ^{125}I-radiolabeling experiments. Andreas Scholl provided help with the sample transfer.

1838 *Biomacromolecules* **2009**, *10*, 1838–1845

X-ray Spectromicroscopy Study of Protein Adsorption to a Polystyrene−Polylactide Blend

Bonnie O. Leung,*,† Adam P. Hitchcock,† Rena Cornelius,‡ John L. Brash,‡ Andreas Scholl,§ and Andrew Doran§

BIMR and School of Biomedical Engineering, McMaster University, Hamilton, Ontario, Canada L8S 4M1, and Advanced Light Source, Berkeley Lab, Berkeley, California 94720

Received March 3, 2009; Revised Manuscript Received May 8, 2009

Synchrotron-based X-ray photoemission electron microscopy (X-PEEM) was used to study the adsorption of human serum albumin (HSA) to polystyrene-polylactide (40:60 PS-PLA, 0.7 wt %) thin films, annealed under various conditions. The rugosity of the substrate varied from 35 to 90 nm, depending on the annealing conditions. However, the characteristics of the protein adsorption (amounts and phase preference) were not affected by the changes in topography. The adsorption was also not changed by the phase inversion which occured when the PS-PLA substrate was annealed above T_g of the PLA. The amount of protein adsorbed depended on whether adsorption took place from distilled water or phosphate buffered saline solution. These differences are interpreted as a result of ionic strength induced changes in the protein conformation in solution.

1. Introduction

Polylactide (PLA), synthesized by ring-opening polymerization of lactide, is a biocompatible and biodegradable synthetic polyester commonly used in tissue engineering and as drug delivery vehicles. For scaffold engineering and drug microcapsules, the rate of degradation and controlled release, respectively, can be greatly impacted by combining a nonbiodegradable polymer such as polystyrene (PS)[1] or polyethylene glycol (PEG)[2] with a biodegradable material. The combination of biodegradable and nonbiodegradable polymers is known as a bioblend.[3] Bioblends can be a simple, cost-effective means of obtaining a composite with tunable physical or chemical properties.[4]

Protein adsorption to biomaterials is important for the biocompatibility of a material, because it is the first event that occurs after implantation of a medical device.[5] PLA is often blended with PEG to produce surface-PEGylated micelles capable of drug delivery.[6−8] Protein adsorption to these microparticles shows a consistent trend of decreased adsorption with increased PEG at the surface.[9,10] Moreover, surface characterization of PLA-PEG spun cast films by X-ray photoelectron spectroscopy (XPS) reveals less protein adsorption compared to pure PLA.[11] However, a major limitation of these studies is the lack of information regarding the spatial distribution of the adsorbed protein relative to the individual components of the dual-polymer substrate.

We use soft X-ray spectromicroscopy techniques such as surface-sensitive synchrotron-based X-ray photoemission electron microscopy (X-PEEM) to visualize and quantitatively map biomolecules adsorbed to candidate biomaterials. Previously, our systematic X-PEEM studies of human serum albumin (HSA) or fibrinogen (Fg)[12] adsorption to phase-segregated PS-poly(methyl methacrylate) (PMMA) thin films with varying protein concentration,[13] exposure time, pH,[14] and protein−peptide competitive adsorption[15] demonstrated that adsorption to PS-PMMA blend surfaces is controlled mainly by hydrophobic effects.

Recently, atomic force microscopy (AFM) and X-ray spectromicroscopy were used to characterize the morphology and phase segregation of a spun-cast PS-PLA bioblend.[16] It was found that the surface morphology depended on mass ratio, total polymer concentration, annealing time, and temperature. Phase segregation improved significantly when the film was heated above the glass transition temperature (T_g) of PLA. This also resulted in a striking phase inversion where the discrete domains became PS-rich rather than PLA-rich.[16]

Here we report studies of the adsorption of HSA to this PS-PLA platform. In addition to investigating the effect of the phase inversion on protein adsorption, we examined the effect of topography since the rugosity of our polymer surface changed from a mean value of 35 to 90 nm rms upon annealing, while retaining similar chemical properties. Also, the effect of ionic strength was investigated by comparing the adsorption of HSA from distilled deionized (DDI) water and phosphate-buffered saline (PBS) solutions. This study is part of an ongoing effort to provide insight into the interaction of blood and blood components with phase-segregated and patterned polymer materials by mapping and quantifying the adsorption of the major blood proteins to candidate biomaterials. These results are intended to contribute to a better understanding of protein adsorption phenomena, which may lead to the development of tissue contacting medical devices of improved biocompatibility.

2. Materials and Methods

2.1. Materials. Polystyrene (MW = 104 K, δ = 1.05) and polylactide (MW = 33 K, δ = 1.33) were obtained from Polymer Source Inc. and used as received. PS/PLA 40:60, 0.7 wt % films were spun cast (4000 rpm, 40 s) from dichloromethane onto a clean 1 × 1 cm native oxide silicon wafer (Wafer World, Inc.), degreased with trichloroethylene, acetone, and methanol, followed by rinsing with DDI.

HSA was obtained from Behringwerke AG, Marburg, Germany, and found to be homogeneous as judged by sodium dodecyl sulfate polyacrylamide gel electrophoresis (SDS-PAGE). Protein solutions for

* Corresponding author. E-mail: leungbo@mcmaster.ca.
† BIMR.
‡ School of Biomedical Engineering.
§ Advanced Light Source.

10.1021/bm900264w CCC: $40.75
Published on Web 06/04/2009

exposure were prepared with DDI water or PBS using HSA concentrations of 0.05, 0.01, and 0.005 mg/mL.

2.2. Substrates and Protein Exposure. Pure PS or PLA were dissolved in toluene or dichloromethane, respectively, and blends of PS with PLA (40:60 ratio) were dissolved in dichloromethane. The solutions were spun cast onto a cleaned native oxide silicon wafer. The PS/PLA substrates were annealed at 45 (1 h, 6 h) and 70 °C (1 h) in a vacuum oven at a pressure ~10^{-5} Torr, achieved with a cryo-trapped turbo pump. The morphology of these substrates and miscibility of the two components were previously characterized by atomic force microscopy (AFM) and X-ray spectromicroscopy.[16]

The films were annealed just prior to protein adsorption studies. The pure PS, pure PLA, or PS/PLA substrate was placed in a beaker, covered with 5 mL of 0.05, 0.01, or 0.005 mg/mL protein solution for 20 min and then diluted three times with at least 50 mL of DDI or PBS buffer. The substrate was removed and vigorously rinsed. The protein adsorbed sample was then carefully dried by touching the edge of the Si wafer with lens paper.

2.3. Scanning Transmission X-ray Microscopy (STXM). High quality near-edge X-ray absorption fine structure (NEXAFS) reference spectra of PS, PLA, and HSA were collected with STXM on beamline 5.3.2 at the Advanced Light Source (ALS) in Berkeley, CA, using X-rays with 80% linear polarization.[17,18] The STXM operates in transmission mode and offers slightly better energy resolution (0.1−0.2 eV) compared to X-PEEM (0.4−0.5 eV); however, similar NEXAFS line shapes are obtained from both methods. Typically, thin film samples with thickness below 100 nm are produced by solvent casting onto an X-ray transparent silicon nitride window. Micrometer size homogeneous areas were measured using image sequences[19] to minimize radiation damage. An image at a damage sensitive energy was recorded after each image sequence measurement to ensure negligible damage. All reference spectra were normalized so that the intensity scale of each component is set to the signal expected from 1 nm of the polymer or protein at its bulk density.

2.4. X-PEEM. All X-PEEM measurements were performed at ALS on bend magnet beamline 7.3.1 (PEEM-2). Detailed accounts of the experimental apparatus, beamline setup and instrument optics have been presented previously.[20] Briefly, photoelectrons and secondary electrons ejected by absorption of 70−80% right circularly polarized monochromatic X-rays are accelerated into an electrostatic imaging column, where the spatial distribution is magnified and detected by a CCD camera. Circularly polarized X-rays are used at PEEM-2 due to slightly better energy resolution compared to linear polarized X-rays. Thus the results are not affected by possible molecular alignment effects (linear dichroism). X-PEEM is a partial electron yield technique with a strong emphasis on low kinetic energy secondary electrons. Thus, X-PEEM is surface sensitive with a sampling depth (1/e) of 4 nm for polymers[21] and an integrated sampling depth of the outer 10 nm of the sample.

With PEEM-2, a 100 nm thick titanium filter was used to eliminate second-order light. To reduce radiation damage, a shutter with a 0.1 s response time was implemented to block the X-ray beam during the time required to transfer images from the charge coupled device (CCD) camera and to step the photon energy. This resulted in an exposure reduction of 50%. The incident flux was reduced to about 10% of the full intensity by masking upstream of the monochromator, and a limited number of energies (23 in C 1s, 47 in N 1s) and a short exposure time per image (1 s) were used as other ways to minimize radiation damage. The field of view was approximately 20 μm.

2.5. X-PEEM Data Analysis. The C 1s and N 1s reference spectra for PS, PLA, and HSA are plotted in Figure 1. At the C 1s edge, the spectra can be easily differentiated with PS characterized by a C 1s → $\pi^*_{C=C}$ transition at 285.15(3) eV. PLA and HSA show strong C 1s → $\pi^*_{C=O}$ transitions at 288.53(3) and 288.20(6) eV, respectively. The carbonyl transition in HSA is at a slightly lower energy than that in PLA since the amide functional group (R-CONH) is a less electronegative environment than the ester group (R-COOR').[12] At the N 1s edge,

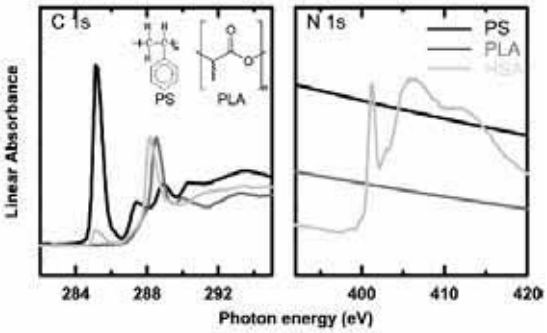

Figure 1. C 1s X-ray absorption spectra of PS (black), PLA (dark gray), and HSA (light gray) as recorded in STXM. The spectra are plotted on an absolute linear absorbance scale. In the case of the C 1s signals, linear background was subtracted.

HSA is easily recognized since it is the only component containing nitrogen. PS and PLA are featureless in the N 1s edge.

All data analyses were performed with the aXis2000 software package.[22] C 1s and N 1s image sequences were aligned, if necessary, normalized to the ring current, and divided by the I_0 spectrum collected from a clean, HF-etched Si(111) chip. The I_0 spectrum itself was corrected for the adsorption of the underlying silicon, as well as with a linear energy term representing the bolometric response of the PEEM detection. All carbon stacks were calibrated by assigning the C 1s → $\pi^*_{C=C}$ transition of PS to 285.15 eV, while the nitrogen stacks were calibrated at the N 1s → π^*_{amide} transition, which occurs at 401.20(5) eV.[21]

The spectra at each pixel of the C 1s image sequence were fit to PS, PLA, and HSA reference spectra by means of singular value decomposition (SVD), an optimized method for least-squares analysis in highly overdetermined data sets.[23,24] At the N 1s edge, because neither PS nor PLA show any transitions, only the spectra of PS and HSA are used in the fit, with areas strong in PS thus representing both PS and PLA. PS was included in the fit to account for a slightly downward sloping background arising from the C 1s continuum. The fit coefficients generated from the SVD analysis are presented as component maps, which are the spatial distributions of each component. Skewed illumination was corrected by dividing the whole stack with a heavily smoothed version of the sum of all the component maps. Finally, the intensities were adjusted so as to give quantitative results by dividing the intensity of each image in the image sequence by a scale factor, which results in a total average thickness (sum of all components) of 10 nm, the sampling depth of X-PEEM.[21]

For combined C 1s and N 1s chemical mapping, a N 1s stack was collected immediately after a C 1s stack with the same region of interest specifications without further alignment. Only well-aligned stacks were used to avoid further misalignment between the two stacks. Next, both stacks were fit with the reference spectra using the SVD method. The C 1s component images of PS and PLA were combined with the N 1s component map of HSA to yield a more accurate and detailed map of the protein. Although the combination of C 1s and N1s edges provides a better qualitative analysis of protein localization, we are still investigating the optimization of multiedge fitting for extracting quantitative information. Thus, all quantitative spectral analysis results presented in this paper are those derived from the C 1s edge only.

For quantitative analysis, a threshold mask was applied to each component map to isolate specific pixels corresponding to PS, PLA, or the interface (Figure 2). In this procedure, only pixels above a certain defined value were included. The average NEXAFS spectrum found for each of the three regions was further modified by setting the pre-edge intensity to zero and then fitting the background subtracted spectrum to the PS, PLA, and HSA reference spectra. Several stacks obtained from different regions of the same sample were analyzed as independent repeat measurements, and the results were averaged to

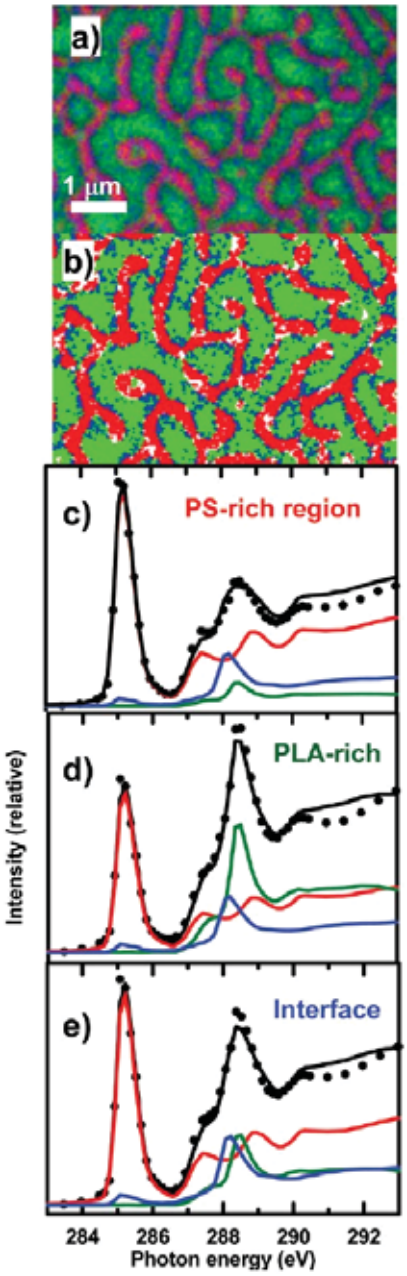

Figure 2. (a) Sample X-PEEM color-coded composite map (absolute) derived from SVD analysis, using the PS, PLA, and HSA reference spectra (Figure 1) of a C 1s image sequence (23 energies) recorded from a PS/PLA blend thin film spun-cast from a dichloromethane solution with a total loading of 0.7 wt % polymer in a 40:60 PS/PLA ratio, and annealed 6 h at 45 °C. (b) Mask used to extract spectra of specific regions. Red denotes PS-rich regions, green denotes PLA-rich regions, defined by threshold masking the PS and PLA component maps. The remaining blue pixels define areas at the interface between the PS-rich and PLA-rich domains. (c) Curve fit of the average C 1s spectra of the PS-rich region (data, dots; fit, black line; components, colored lines). (d) Curve fit of the average C 1s spectra of the PLA-rich region (same color coding). (e) Curve fit of the average C 1s spectra of the interface region (same color coding).

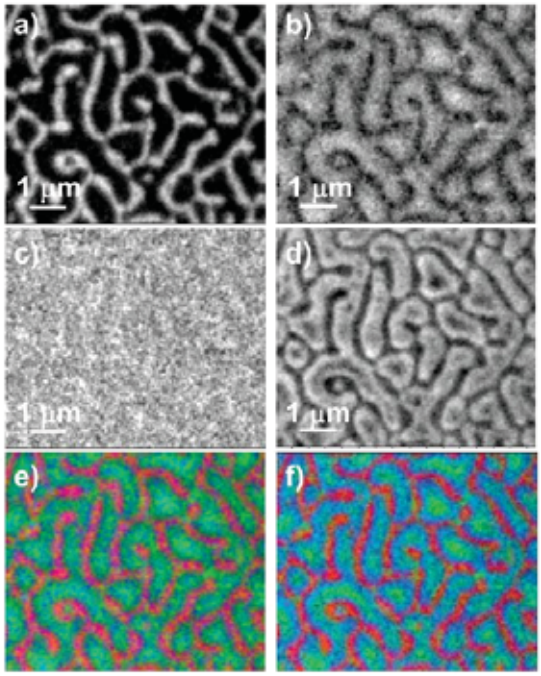

Figure 3. Component maps measured from a 40:60 PS/PLA ratio annealed 6 h at 45 °C. Component maps of (a) PS, (b) PLA, (c) HSA, derived from a C 1s image sequence (gray scale is thickness in nm). (d) HSA component map obtained from fit to the N 1s image sequence of the same area. (e) Rescaled color composite map based on component maps derived from the C 1s image sequence (red = PS, green = PLA, blue = HSA). (f) Rescaled color composite map combining maps from C 1s and N 1s (red = PS (C1s), green = PLA (C1s), blue = HSA (N1s)).

obtain the final quantitative values. The uncertainties reported are the standard deviations from these multiple determinations.

2.6. ^{125}I-Radiolabeling. HSA (Sigma Aldrich) was labeled with ^{125}I (ICN Biomedicals, Mississauga, ON, Canada) using standard radioiodination methods with IODO-GEN (Pierce Chemical Company, Rockford, IL). The labeled protein was dialyzed overnight against DDI water. Radiolabeling experiments were performed with four repeats by exposing 1 mL solutions of 0.05, 0.01, or 0.005 mg/mL HSA from DDI water or PBS solution for 20 min followed by four static rinses of 2.5 min duration each. Adsorbed amounts were calculated as described earlier.[25]

3. Results and Discussion

3.1. Combined C 1s and N 1s Chemical Mapping. Figure 3 presents sample component maps obtained from SVD fitting of the reference spectra to representative stacks at the carbon and nitrogen edge of 0.05 mg/mL HSA adsorbed to a PS/PLA 40:60 (0.7 wt %) film annealed for 6 h at 45 °C. At the carbon edge, the use of three reference spectra (PS, PLA, and HSA) in the fit yields three component maps. The bright white pixels of the PS (Figure 3a) and PLA (Figure 3b) maps indicate areas of PS and PLA, respectively. A close examination of the HSA component map (Figure 3c) reveals that the pixels indicative of protein are brightest at the interface between the PS and PLA continuous phases. As previously shown for blood protein adsorption to PS/PMMA films, the interface is the area of lowest free energy and thus the preferred site of adsorption.[12,13]

The nitrogen edge is very sensitive to protein as it is the only nitrogen-containing species in this system. As demonstrated by the protein component map derived from the N 1s sequence (Figure 3d), HSA adsorbs most extensively to the interface between the PS and PLA cocontinuous domains (as determined from the C 1s analysis) but also has significant signal on the PLA-rich domain. This is evident by the dark gray areas corresponding to continuous PS and also a darker area toward the center of the domains corresponding to PLA. The tricolor coded composite component map based only on the C 1s image sequence component maps (Figure 3e) reveals that the protein (color coded in blue) is strongest at the interface between PS (red) and PLA (green). Because the carbon and nitrogen stacks are collected at the exact same region, the component maps of PS and PLA (which are easily distinguishable at the carbon edge) can be combined with the HSA component map from the N 1s edge. The resulting map (Figure 3f) reveals the protein distribution relative to the substrate components with much greater precision than the analysis based solely on the C 1s image sequence. The site of preferential HSA adsorption occurs at the interface between the two polymer domains.

X-PEEM chemical mapping using combined carbon and nitrogen ls edges provides a means for mapping HSA through a combination of near edge and elemental discrimination. Among the available species-specific microscopy techniques, scanning X-ray photoemission microscope (SPEM)[26] has similar capabilities to X-PEEM. However, X-PEEM currently has better spatial resolution (<50 nm) relative to SPEM (~150 nm) and lower radiation damage rates. STXM is a complementary technique to X-PEEM because X-rays transmit through the entire polymer film; however, X-PEEM is more sensitive to adsorbed protein since it probes only the top 10 nm of the film surface. Furthermore, some X-PEEM microscopes such as those at Elettra and the Canadian Light Source (CLS) have energy filters that allow for XPS imaging at slightly better spatial resolution. Electron energy loss spectroscopy (EELS) in transmission electron microscopes (TEM) offers 5 nm (or lower) spatial resolution.[27] However, this technique is very limited for biomaterial applications due to much higher radiation damage[28,29] and poorer energy resolution than X-ray techniques.

3.2. Effect of Topography. Previously, the miscibility and morphology of three PS/PLA 40:60 (0.7 wt %) films were examined as a function of annealing times (1 h vs 6 h) and temperatures (45 and 70 °C).[16] It was found that annealing at 45 °C for 1 and 6 h led to a progressive coarsening of the PLA continuous domains, with the height of the domains increasing by 10 nm, as judged by AFM. Annealing at 70 °C for 1 h, in excess of the glass transition temperature (T_g) of PLA ($T_g \sim 60$ °C), resulted in a phase inversion where the discrete domains were composed of PS. The PS domains doubled in height (~90 nm) at this temperature.

Strikingly, although the morphology of the PS-PLA films changed significantly with vacuum annealing, the quantitative results from X-PEEM[16] revealed the composition of the blends to be similar, with the percentages of PS and PLA varying by only 10 and 13% in the PS and PLA regions, respectively, for the three films annealed for 1 h at 45 °C, 6 h at 45 °C, and 1 h at 70 °C. However, the rugosity of these three films varied from 35 to 90 nm (rms fluctuation). Thus, the three films provide chemically similar platforms for protein adsorption studies and allow an investigation of the effect of topography, independent of surface chemistry.

Figure 4a−c illustrates the rescaled X-ray spectromicroscopy color-coded composite maps of the three films obtained after exposure to 0.05 mg/mL solutions of HSA from DDI water, while Figure 4d–f presents rescaled X-ray spectromicroscopy color-coded composite maps of the three films (different samples of same history) prior to protein adsorption. In comparison to the PS-PLA films prior to protein adsorption, the X-PEEM composite maps after HSA adsorption show a much more blue color arising from the adsorbed protein. The purely red (PS) and green (PLA) regions in the native films are now "pink" and "turquoise", clearly indicating that HSA has adsorbed to some extent across the entire surface. Similar to the results obtained from HSA adsorption to PS/PMMA films,[13] a thin band of protein (blue) is seen to adsorb preferentially at the interface, which we thus conclude is the area of lowest free energy.

Table 1 summarizes the quantitative analysis of HSA thicknesses on the PS, PLA and interface regions of these films. Comparison of HSA adsorption to the PS, PLA, and interface regions among the three films reveal markedly consistent adsorption thicknesses, with variations less than 0.5 nm, the estimated uncertainty in the measurements. The data analysis quantifies the preferential adsorption to the interface, with a 0.6−0.9 nm greater HSA thickness at the interface than on the PS or PLA regions (Table 1). Furthermore, comparison of the thicknesses of adsorbed HSA between the PS-PLA films and PS-PMMA films shows clear similarities in the location of preferential adsorption and thickness values.[13] Likely, this similarity arises from the chemical similarity of the PS-PLA and PS-PMMA systems, with PLA and PMMA polymers composed of similar functional groups and, thus, the domains having similar hydrophobicities. The quantitative analyses show a trend of slightly increasing adsorbed HSA thickness as the domain height increases. However, the increase is within the limits of uncertainty.

The data obtained (Table 1) show that topographical variation in the 35−90 nm range does not significantly alter HSA adsorption to PS/PLA. Further evidence is seen in the control experiments where 0.05 mg/mL HSA was adsorbed to flat films spun cast from only PS or PLA. Adsorption on both pure substrates showed thickness of adsorbed HSA (1.4(5) nm on pure PS; 1.7(5) nm on pure PLA) similar to that on the blended films.

There are conflicting reports in the literature on the dependence of protein adsorption on topography. Small structures below ~5 nm[30−32] appear to result in a higher amount of adsorbed protein, whereas for some proteins, larger structures (greater than 10 nm) do not affect the adsorbed quantity.[33] It has been postulated that larger structures appear as smooth surfaces for proteins, and the effective surface area is increased by only a small amount.[30] Nonetheless, it is evident that this behavior is highly protein specific. For example, a titanium substrate patterned by local anodic oxidation to exhibit 1−2 nm high or 3−4 nm high titanium lines (fwhm 40 nm) revealed F-actin to preferentially adsorb to the 1−2 nm high structures, while protein A (and subsequently IgG) showed no preference to structures of either height.[31] Also, it was shown that increasing the root-mean-square roughness of evaporated tantalum films from 2 to 40 nm resulted in increased adsorption of fibrinogen and conformational changes in adsorbed fibronectin.[34,35] More relevant to the present work, surface roughness variations in titanium from 2 to 20 nm were reported not to affect the amount of HSA adsorbed.[33] Thus, the observation in the present work that topography had no effect on albumin adsorption to PS-PLA films may be due to the intrinsic nature of HSA itself.

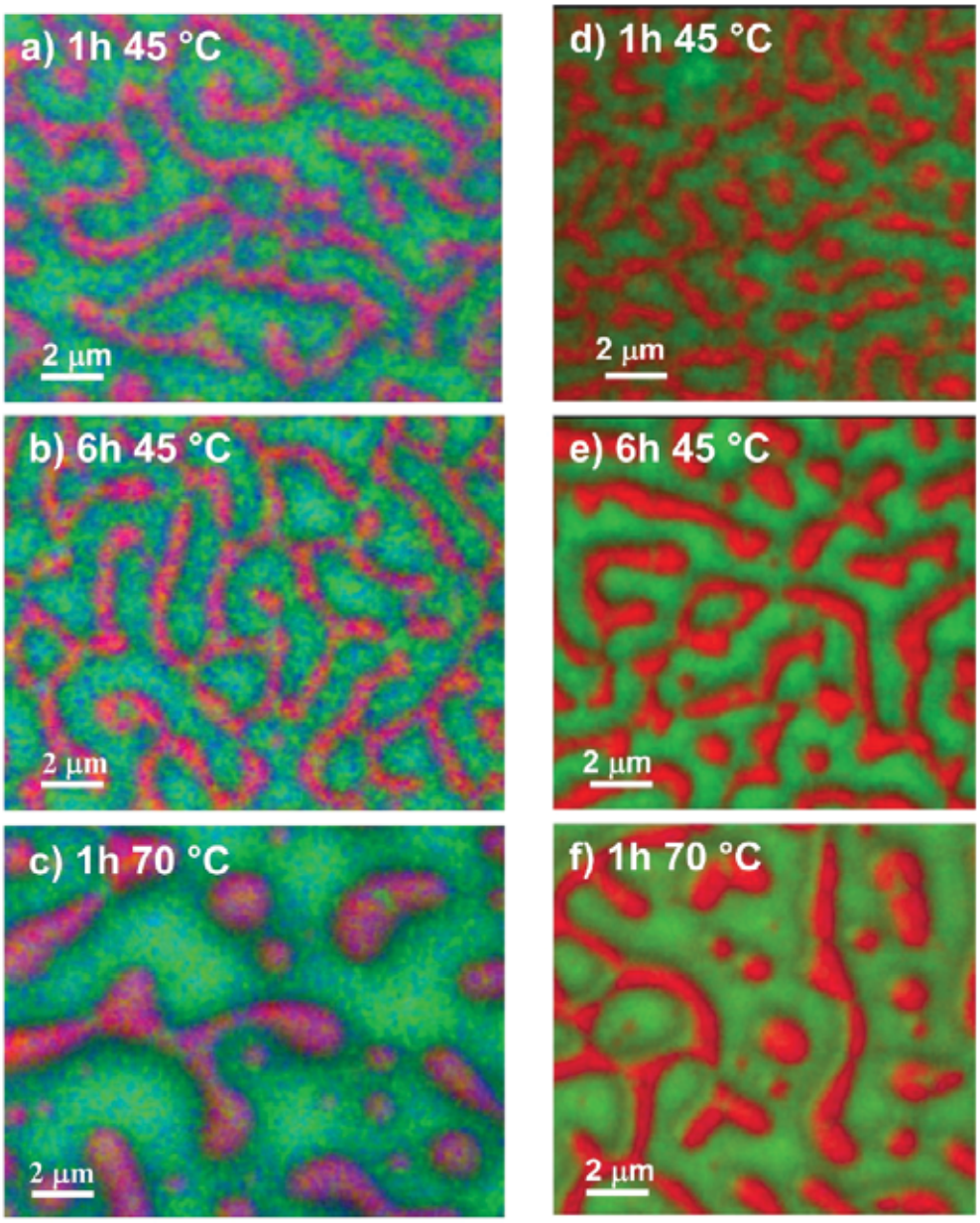

Figure 4. (Left) X-PEEM rescaled color-coded composite maps of 40:60 PS/PLA films (0.7 wt % loading) annealed at (a) 1 h at 45 °C, (b) 6 h at 45 °C, (c) 1 h at 70 °C and exposed to 0.05 mg/mL solutions of HSA from DDI water. The maps were derived from C 1s image sequences. PS is coded red, PLA is coded green, and HSA is coded blue. (Right) Color coded maps from C 1s image sequences of PS/PLA spun cast films (without adsorbed protein) vacuum annealed for (d) 1 h at 45 °C, (e) 6 h at 45 °C, (f) 1 h at 70 °C.

3.2. Effect of Salts. Three concentrations of HSA (0.005, 0.01, and 0.05 mg/mL) in DDI water and PBS buffer were exposed to the PS/PLA 40:60 (0.7 wt %) film annealed for 1 h at 70 °C. Figure 5a−f and g−l present the color-coded composite maps obtained for the three films immersed in DDI water and PBS buffer protein solutions, respectively. For the DDI system, the rescaled images reveal that at the highest protein concentration (0.05 mg/mL) HSA (blue) preferentially adsorbs to the interface between the PS and PLA domains, as evidenced by a thin band of blue. As the protein concentration decreases, the band disappears and the blue color is more evenly spread across the surface. The color composite map presented on an absolute scale for the 0.05 mg/mL system (Figure 5b) shows more turquoise and pink colors suggesting slightly higher protein adsorption, while that for lower concentration (0.005 mg/mL, Figure 5f)

Table 1. Thickness (nm) of PS, PLA, and HSA in the PS, PLA, and Interface from PS/PLA 40:60 (0.7 wt %) Films[a]

region	composite thickness (nm)	0.05 mg/mL HSA		
		1 h, 45 °C	6 h, 45 °C	1 h, 70 °C
PS	PS	6.3	7.0	8.1
	PLA	2.1	0.9	0.0
	HSA	1.7	2.1	1.9
PLA	PS	2.7	2.9	2.5
	PLA	5.4	5.2	5.1
	HSA	1.9	1.9	2.4
interface	PS	4.4	4.7	6.5
	PLA	3.3	2.5	0.7
	HSA	2.3	2.8	2.7

[a] Films were annealed 1 h at 45 °C, 6 h at 45 °C, and 1 h at 70 °C. Uncertainty: ±0.5 nm.

exhibits many bright green pixels, implying less uniform distribution of protein.

The rescaled images of the samples in the PBS buffer system (Figure 5g,i,k) demonstrate similar shades of turquoise and pink. The images at the higher concentrations (0.05 and 0.01 mg/mL) reveal preferential protein adsorption to the interface between PS and PLA domains. The blue color of the absolute image of the film exposed to 0.05 mg/mL HSA (from PBS buffer, Figure 5h) is indicative of a high amount of adsorbed protein. As the concentration decreases, the images gain a significantly "greener" and "redder" hue, indicating decreased protein adsorption. Qualitatively, at higher protein concentrations (0.05 mg/mL HSA), HSA shows greater adsorption from a PBS compared to a DDI solution; however, at lower concentrations (0.01 and 0.005 mg/mL HSA), similar thicknesses of adsorbed protein are observed in both systems.

The quantitative results obtained from the spectral fitting for the films exposed to protein from DDI water reveal that, regardless of concentration, protein adsorption is the most extensive at the interface between PS and PLA (Table 2). As the concentration of HSA decreases, the average thickness of protein across the entire polymer surface also decreases. Comparison of adsorption on PS and PLA regions at a particular concentration shows a slight preference for the PS region, similar to the PS/PMMA system.[13,14] This similarity may be due to the presence of the ester functional group in both PLA and PMMA.

The quantitative results for HSA adsorption from PBS buffer also show preferential adsorption at the interface; however, the thickness values are almost twice as great as those detected in DDI water at the interface for all three protein concentrations. The X-PEEM results reveal a general increase in the thickness of adsorbed protein with increasing ionic strength (especially on the PLA and interface regions), which appears to conflict with literature reports showing a decrease in adsorbed quantity with increasing salt concentration on silica, pegylated Nb_2O_5, and $Si(Ti)O_2$ surfaces, as determined using neutron reflectivity,[36] optical waveguide light made spectroscopy,[37] and integrated optical methods,[38] respectively. However, according to the latter studies, although the number of protein molecules decreased with increasing ionic strength, the area occupied by the adsorbed molecules increased almost 10-fold at a NaCl concentration of 0.5 mol/L.[38]

The increased HSA thickness detected for adsorption from buffer, especially in the PLA and interface regions, could be due to an increased number of adsorbed HSA molecules or to a change in conformation resulting in increasing size, with no change in the number density. To investigate these possibilities, adsorbed quantities were measured using ^{125}I-labeled HSA under

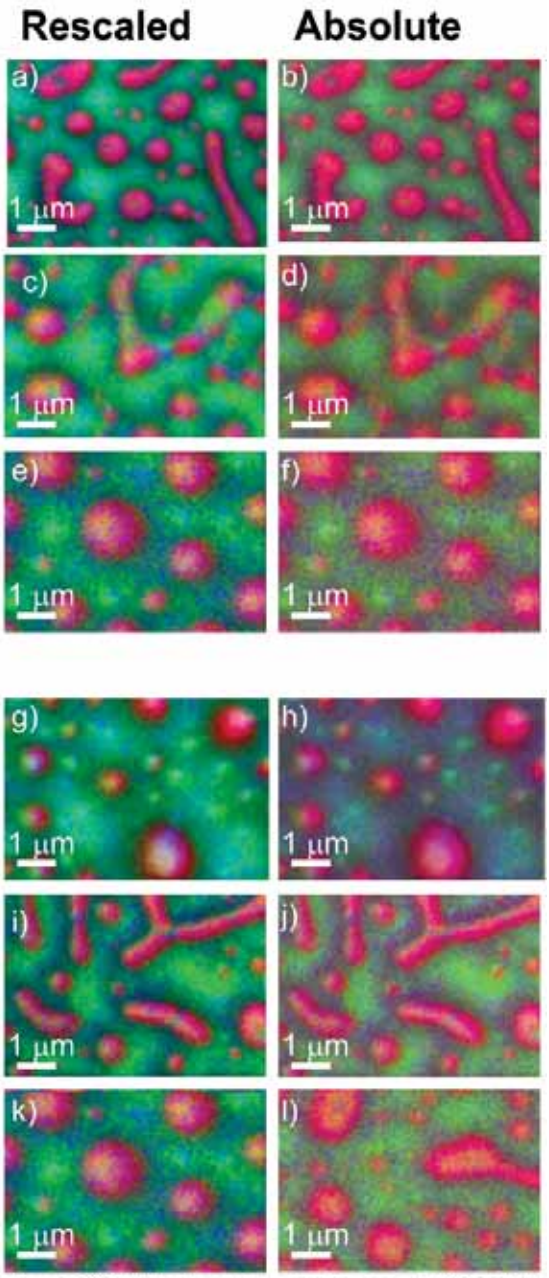

Figure 5. X-PEEM color coded composite maps of 40:60 PS/PLA films (0.7 wt % loading), annealed 1 h at 70 °C with protein adsorbed from DDI water: (a) 0.05 mg/mL HSA (rescaled), (b) 0.05 mg/mL HSA (absolute), (c) 0.01 mg/mL HSA (rescaled), (d) 0.01 mg/mL HSA (absolute), (e) 0.005 mg/mL HSA (rescaled), and (f) 0.005 mg/mL HSA (absolute). Same polymer composition with protein adsorbed from PBS buffer: (g) 0.05 mg/mL HSA (rescaled), (h) 0.05 mg/mL HSA (absolute), (i) 0.01 mg/mL HSA (rescaled), (j) 0.01 mg/mL HSA (absolute), (k) 0.005 mg/mL HSA (rescaled), (l) 0.005 mg/mL HSA (absolute). PS is coded red, PLA is coded green, and HSA is coded blue.

identical conditions from both DDI and PBS solution (Figure 6). The radiolabeling method provides a means of measuring

Table 2. Thickness (nm) of PS, PLA, and HSA in the PS, PLA, and Interface Regions from PS/PLA 40:60 (0.7 wt %) Films[a]

		HSA adsorbed from DDI			HSA adsorbed from PBS		
region	composite thickness (nm)	0.05 mg/mL	0.01 mg/mL	0.005 mg/mL	0.05 mg/mL	0.01 mg/mL	0.005 mg/mL
PS	PS	8.1	8.0	9.0	7.8	8.3	9.2
	PLA	0.0	0.9	0.2	0.2	0.3	0.2
	HSA	1.9	1.1	0.8	2.0	1.4	0.7
PLA	PS	2.5	3.0	3.0	2.6	2.5	2.7
	PLA	5.1	6.1	6.7	4.7	6.0	6.5
	HSA	2.4	0.9	0.3	2.8	1.5	0.8
interface	PS	6.5	5.1	3.8	3.9	4.6	4.6
	PLA	0.7	3.1	4.5	2.0	2.5	2.7
	HSA	2.7	1.8	1.7	4.1	3.5	2.8

[a] Films annealed 1 h at 70 °C and exposed to 0.05, 0.01, and 0.005 mg/mL HSA from either DDI water or PBS buffer. Uncertainty: ±0.5 nm.

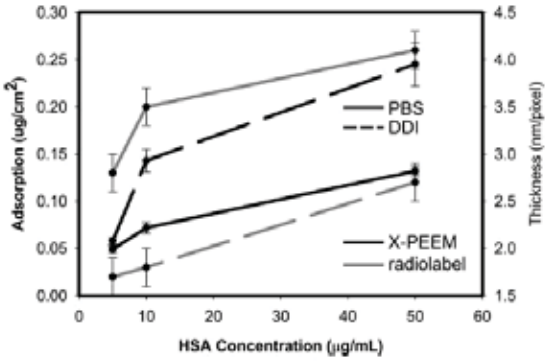

Figure 6. Isotherms for adsorption of ^{125}I-labeled HSA from PBS and DDI water. PBS is solid and DDI is dashed. X-PEEM detected thickness is plotted in gray, radiolabeling in black.

Table 3. ^{125}I Radiolabeling Experiments[a]

concentration	DDI	sd	PBS	sd
0.005	0.058	0.004	0.049	0.004
0.01	0.143	0.012	0.072	0.006
0.05	0.245	0.023	0.132	0.005

[a] HSA adsorption (μg/cm^2) from DDI water or PBS buffer with standard deviations (sd, $n = 4$).

the number of adsorbed protein molecules, independent of their conformation. The data from these experiments showed that at the higher concentrations (0.05 and 0.01 mg/mL protein) the number of HSA molecules adsorbed from DDI water is almost double that from buffer, while similar numbers of molecules were adsorbed from both media at the lowest concentration (0.005 mg/mL HSA; Table 3). These results are in striking contrast to the X-PEEM data, which showed increasing thicknesses of HSA on the PLA and interface regions with increasing ionic strength. Thus, we conclude that if the number of adsorbed protein molecules is lower for adsorption from PBS compared to DDI water (as judged by radiolabeling) then the increased thickness detected from X-PEEM must arise from a change in conformation to a more extended structure.

In the case of charged surfaces, previous studies[36–38] have attributed the decrease in protein adsorption at higher ionic strength to electrostatic effects. Here we show that such a decrease occurs on a neutral substrate. We speculate that in DDI water, the hydrophilic, charged amino acid residues of HSA are likely less exposed compared to PBS buffer; thus, water molecules have an increased opportunity to hydrogen bond (or form structured water) to the more hydrophobic protein molecule in DDI water. When adsorption occurs from this situation (DDI water) there is a greater entropy loss compared to adsorption from PBS buffer where there is a lower extent of entropy loss since there is less disruption of structured water. Thus, we conclude that the hydrophobic effect plays an important role in protein adsorption to the blend materials studied in this work.

The difference in thicknesses of HSA adsorbed from PBS versus DDI solutions probably arise from changes in protein conformation in solution with change in ionic strength, revealed via comparison of the X-PEEM and radiolabeling results. Therefore, in combination with techniques such as radiolabeling or other methods that measure adsorbed quantity, X-PEEM provides an effective, albeit indirect, approach to probing conformational changes in adsorbed protein that may give rise to a change in thickness.

4. Conclusions

The adsorption of HSA to PS-PLA surfaces was studied by X-PEEM and radiolabeling. The influence of topography, buffer conditions, and annealing on the adsorption were investigated. No significant changes in adsorption were observed upon increasing the surface roughness of the substrate. By investigating the adsorption of HSA from PBS and DDI water solutions and comparing the results of X-PEEM and radiolabeling experiments, it is concluded tentatively that the HSA molecule is expanded in PBS compared to DDI water.

Acknowledgment. This research is supported by the Natural Sciences and Engineering Research Council of Canada (NSERC), AFMNet, and the Canada Research Chair programs. X-ray microscopy was carried out using PEEM2 and STXM532 at the ALS. The ALS is supported by the U.S. Department of Energy under Contract DE-AC03-76SF00098.

References and Notes

(1) Saravanan, M.; Bhaskar, K.; Srinivasa, R. G.; Dhanaraju, M. D. *J. Microencapsulation* **2003**, *20*, 289–302.
(2) Cai, Q.; Bei, J.; Wang, S. *Polym. Adv. Technol.* **2002**, *13*, 534–540.
(3) Biresaw, G.; Carriere, C. J.; Willett, J. L. *J. Appl. Polym. Sci.* **2004**, *94*, 65–73.
(4) Zhang, G.; Zhang, J.; Wang, S.; Shen, D. *J. Polym. Sci., Part B: Polym. Phys.* **2003**, *41*, 23–30.
(5) Castner, D. G.; Ratner, B. D. *Surf. Sci.* **2002**, *500*, 28–60.
(6) Yasugi, K.; Nagasaki, Y.; Kato, M.; Kataoka, K. *J. Controlled Release* **1999**, *62*, 89–100.
(7) Agrawal, S. K.; Sanabria-DeLong, N.; Coburn, J. M.; Tew, G. N.; Bhatia, S. R. *J. Controlled Release* **2006**, *112*, 64–71.
(8) Zhou, S.; Liao, X.; Li, X.; Deng, X.; Li, H. *J. Controlled Release* **2003**, *86*, 195–205.
(9) Jeong, J. H.; Lim, D. W.; Han, D. K.; Park, T. G. *Colloids Surf., B* **2000**, *18*, 371–379.
(10) Vittaz, M.; Bazile, D.; Spenlehauer, G.; Verrecchia, T.; Veillard, M.; Puisieux, F.; Labarre, D. *Biomaterials* **1996**, *17*, 1575–1561.
(11) Lucke, A.; Tebmar, J.; Schnell, E.; Schmeer, G.; Gopferich, A. *Biomaterials* **2000**, *21*, 2361–2370.

(12) Morin, C.; Hitchcock, A. P.; Cornelius, R. M.; Brash, J. L.; Scholl, A.; Doran, A. *J. Electron. Spectrosc. Relat. Phenom.* **2004**, *137*−*140*, 785–794.
(13) Li, L.; Hitchcock, A. P.; Robar, N.; Cornelius, R.; Brash, J. L.; Scholl, A.; Doran, A. *J. Phys. Chem. B* **2006**, *110*, 16763–16773.
(14) Li, L.; Hitchcock, A. P.; Cornelius, R.; Brash, J. L.; Scholl, A.; Doran, A. *J. Phys. Chem. B* **2008**, *112*, 2150–2158.
(15) Leung, B. O.; Hitchcock, A. P.; Brash, J. L.; Scholl, A.; Doran, A.; Henklein, P.; Overhage, J.; Hilpert, K.; Hale, J. D.; Hancock, R. E. W. *Biointerphases* **2008**, *3*, F27–F35.
(16) Leung, B. O.; Hitchcock, A. P.; Brash, J. L.; Scholl, A.; Doran, A. *Macromolecules* **2009**, *42*, 1679–1684.
(17) Warwick, T.; Ade, H.; Kilcoyne, A. L. D.; Kritscher, M.; Tylisczcak, T.; Fakra, S.; Hitchcock, A. P.; Hitchcock, P.; Padmore, H. A. *J. Synchrotron Radiat.* **2002**, *9*, 254–257.
(18) Kilcoyne, A. L. D.; Tylisczak, T.; Steele, W. F.; Fakra, S.; Hitchcock, P.; Franck, K.; Anderson, E.; Harteneck, B.; Rightor, E. G.; Mitchell, G. E.; Hitchcock, A. P.; Yang, L.; Warwick, T.; Ade, H. *J. Synchrotron Radiat.* **2003**, *10*, 125–136.
(19) Jacobsen, C. J.; Zimba, C.; Flynn, G.; Wirick, S. *J. Microsc. (Oxford, U.K.)* **2000**, *197*, 173–184.
(20) Anders, S.; Padmore, H. A.; Duarte, R. M.; Renner, T.; Stammler, T.; Scholl, A.; Scheinfein, M. R.; Stohr, J.; Seve, L.; Sinkovic, B. *Rev. Sci. Instrum.* **1999**, *70*, 3973–3981.
(21) Wang, J.; Li, L.; Morin, C.; Hitchcock, A. P.; Doran, A.; Scholl, A. *J. Electron Spectrosc. Relat. Phenom.* **2009**, *170*, 25–36.
(22) aXis2000 is free for noncommercial use. It is written in Interactive Data Language (IDL) and available from http://unicorn.mcmaster.ca/aXis2000.html.
(23) Strang, G. In *Linear Algebra and Its Applications*; Harcourt Bracourt, Jovanovich: San Diego, CA, 1988.
(24) Koprinarov, I. N.; Hitchcock, A. P.; McCrory, C. T.; Childs, R. F. *J. Phys. Chem. B* **2002**, *106*, 5358–5364.
(25) Chan, B. M. C.; Brash, J. L. *J. Colloid Interface Sci.* **1981**, *82*, 217–225.
(26) Goldoni, A.; Larciprete, R.; Gregoratti, L.; Kaulich, B.; Kiskinova, M.; Zhang, Y.; Dai, H.; Sangaletti, L.; Parmigiani, F. *App. Phys. Lett.* **2002**, *80*, 2165–2167.
(27) Sugena, K.; Tence, M.; Mory, C.; Colliex, C.; Kato, H.; Okazaki, T.; Shinohara, H.; Hirahara, K.; Bandow, S.; Iijima, S. *Science* **2000**, *290*, 2280–2282.
(28) Rightor, E. G.; Hitchcock, A. P.; Ade, H.; Leapman, R. D.; Urquhart, S. G.; Smith, A. P.; Mitchell, G.; Fischer, D.; Shin, H. J.; Warwick, T. *J. Phys. Chem. B* **1997**, *101*, 1950–1960.
(29) Wang, J.; Botton, G. A.; West, M. M.; Hitchcock, A. P. *J. Phys. Chem. B* **2009**, *113*, 1869–1876.
(30) Macarena Blanco, E.; Horton, M. A.; Mesquida, P. *Langmuir* **2008**, *24*, 2284–2287.
(31) Gallia, C.; Collaud Coen, M.; Hauert, R.; Katanaev, V. L.; Gröning, P.; Schlapbach, L. *Colloids Surf., B* **2002**, *26*, 255–267.
(32) Dolatshahi-Pirouz, A.; Rechendorff, K.; Hovgaard, M. B.; Foss, M.; Chevallier, J.; Besenbacher, F. *Colloids Surf., B* **2008**, *66*, 53–59.
(33) Cai, K.; Bossert, J.; Jandt, K. D. *Colloids Surf., B* **2006**, *49*, 136–144.
(34) Rechendorff, K.; Hovgaard, M. B.; Foss, M.; Zhdanov, V. P.; Besenbacher, F. *Langmuir* **2006**, *22*, 10885–10888.
(35) Hovgaard, M. B.; Rechendorff, K.; Chevallier, J.; Foss, M.; Besenbacher, F. *J. Phys. Chem. B* **2008**, *112*, 8241–8249.
(36) Su, T. J.; Lu, J. R.; Thomas, R. K.; Cui, Z. F.; Penfold, J. *J. Colloids Interface Sci.* **1998**, *203*, 419–429.
(37) Pache, S.; Voros, J.; Griesser, H. J.; Spencer, N. D.; Textor, M. *J. Phys. Chem. B* **2008**, *109*, 17545–17552.
(38) Ramsden, J. J.; Prenosil, J. E. *J. Phys. Chem.* **1994**, *98*, 5376–5381.

BM900264W

CHAPTER 5: AN X-RAY SPECTROMICROSCOPY STUDY OF ALBUMIN ADSORPTION TO CROSS-LINKED POLYETHYLENE OXIDE FILMS

Polyethylene oxide (PEO) was combined with 1.5, 5.0 and 10.0 % pentaerythritol triacrylate (PETA), a UV crosslinker, and then exposed to human albumin serum (HSA) solutions to examine if the crosslinker affected the biocompatibility of PEO. It was found that the PETA crosslinker is highly surface active and segregates to the substrate-air interface. Furthermore, more protein adsorption was seen with increasing PETA concentrations. Thus, adding 5.0% or more PETA affects the protein resistance of PEO.

Copyright

Author contribution

The author of this thesis contributed to this publication in the following ways: all sample preparation, all X-PEEM data collection, all X-PEEM data analysis, and the first draft of the manuscript. Andreas Scholl provided help with the sample transfer.

CHAPTER 5: AN X-RAY SPECTROMICROSCOPY STUDY OF ALBUMIN ADSORPTION TO CROSS-LINKED POLYETHYLENE OXIDE FILMS

5.1. Introduction

Polyethylene oxide (PEO) is a hydrophilic polymer commonly used in biomedical applications to reduce protein adsorption [89] or improve biocompatibility [90]. The effectiveness of PEO for reducing protein adsorption to surfaces likely arises from its molecular conformation in aqueous solution, with repulsive forces developed at certain separation distances resulting in a steric repulsion effect [91 - 95]. Furthermore, PEO density, chain length, conformation, lack of charge, and its interactions with water are known to affect protein resistance [96 - 99].

Since PEO is soluble in water, techniques such as γ [100], UV [101,102] and electron irradiation [103], have been employed to crosslink the PEO chains to prevent mass loss upon protein exposure. UV-initiated crosslinking of PEO with pentaerythritol triacrylate (PETA) or other radical crosslinkers [104] is becoming increasingly popular since PEO can be crosslinked in both solution and solid state [105,106]. The inclusion of PETA to form crosslinked PEO has been used in biomedical applications such as hydrogels [107] and micelles [108] for drug delivery, or to form chemically patterned surfaces for cell studies [109]. However, to our knowledge, the effect of PETA crosslinker on the biocompatibility of PEO-based materials has not been systematically investigated.

In this study, we use synchrotron-based X-ray photoemission electron microscopy (X-PEEM) for surface characterization of thin PEO films containing variable levels of

PETA crosslinker. We then investigate the effect of the PETA on the adsorption of human serum albumin (HSA) to these surfaces. Previously, we used X-PEEM to study HSA adsorption to phase segregated polystyrene (PS)-poly(methyl methacrylate) (PMMA) [59-61, 110, 111] or PS-polylactide (PLA) [112] thin films. This study is part of an on-going effort to use X-PEEM and other techniques to obtain detailed information on the interfacial interactions of proteins by measuring the distribution of specific proteins over well-characterized, chemically segregated surfaces at high spatial resolution.

5.2 Experimental

5.2.1 Materials and Protein Exposure

PEO (MW=600K) and PETA were purchased from Sigma Aldrich and used as received. Human serum albumin (HSA) was purchased from Behringwerke AG, Marburg, Germany, and found to be homogeneous as judged by sodium dodecyl sulphate polyacrylamide gel electrophoresis (SDS-PAGE).

To examine the effect of PETA crosslinker, PEO (50 mg) and PETA (0%, 1% (0.8 mg, 2.6×10^{-6} mol), 5% (2.5 mg, 8.4×10^{-6} mol) and 10% (5.1 mg, 1.7×10^{-5} mol) by weight were dissolved in dichloromethane (5 g) and spun cast (4000 rpm, 40s) onto a clean native oxide silicon wafer. Then the substrates were exposed to a 365 nm UV lamp under flowing nitrogen for 40 min to crosslink the PEO. No filters or initiators were used. The films were 100 – 200 nm thick. Next, the thin films were immersed in 5 mL of 0.005

mg/mL HSA for 20 min, washed vigorously and air dried. For the PEO sample with 0% PETA, the PEO dissolved upon exposure to protein solution.

5.2.2 X-ray Spectromicroscopy

High quality near-edge X-ray absorption fine structure (NEXAFS) reference spectra of PEO, PETA and HSA (Figure 5.1) were collected with the scanning transmission X-ray microscope (STXM) on beamline 5.3.2 at the Advanced Light Source (ALS) in Berkeley, CA [113,114]. While the STXM beamline has better energy resolution (0.1 - 0.2 eV) compared to the X-PEEM beamline (0.4 - 0.5 eV), similar spectral lineshapes were obtained from both techniques. Samples for STXM were solvent-cast onto an X-ray transparent silicon nitride window (75 nm thick, 1 mm x 1 mm, Norcada Inc) and micrometer sized areas were probed using image sequences (stacks [115]). The intensity scale of each reference spectrum was normalized to the signal expected from 1 nm of the polymer or protein at its bulk density.

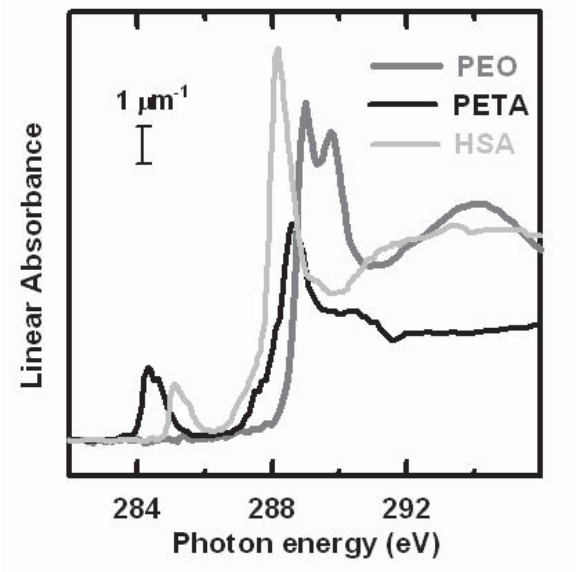

Figure 5.1: C 1s X-ray absorption spectra of polyethylene oxide (PEO), pentaerythritol triacrylate (PETA) and human serum albumin (HSA) as recorded in STXM. The spectra are plotted on an absolute linear absorbance scale.

X-PEEM data collection was performed at the ALS on beamline 7.3.1 with the PEEM-2 microscope. Briefly, photoelectrons and secondary electrons are ejected upon absorption of 70-80% left circularly polarized monochromatic X-rays. The electron distribution is magnified with an electrostatic imaging column and the spatial distribution is detected with a CCD camera [81]. X-PEEM is a total electron yield technique which probes the top 10 nm of the sample, with a measured sampling depth of (1/e) of 4 nm for organic polymers [81]. A 100 nm thick titanium filter was used to reduce second-order light. A shutter with 0.1 second response time blocked the X-ray beam except during image acquisition.

5.2.3 X-PEEM Data Analysis

All data analyses were performed with the aXis2000 software package [83]. C 1s image sequences were aligned and then normalized to the ring current and to the I_0 spectrum obtained from a clean HF-etched Si chip. The I_0 spectrum was corrected for the absorption of underlying silicon and the linear bolometric response function of the detector. The energy scales were set by calibrating the C 1s $\rightarrow \pi^*_{C=C}$ transition of a clean polystyrene sample to 285.15 eV.

Singular value decomposition was used to fit the C 1s spectrum at each pixel of an image sequence with the PEO, PETA and HSA reference spectra [116,117]. The fit coefficients obtained from the SVD fit are assembled into component maps which show the spatial distribution of each component. Non-uniform illumination was compensated by dividing each component map with a heavily smoothed image of the sum of all

components. Furthermore the intensity of each image was divided by a scale factor which results in a total average thickness (sum of all components) of 10 nm, the total depth sampled by X-PEEM [75].

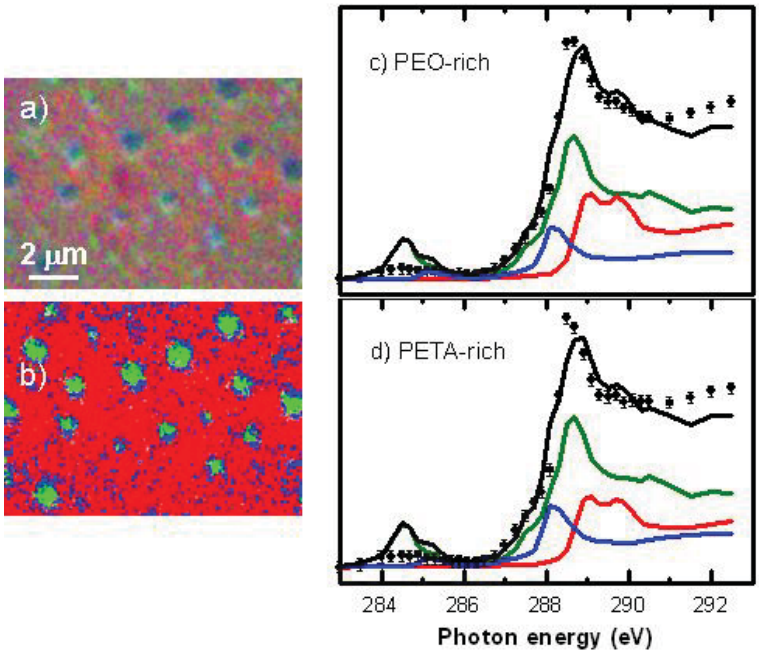

Figure 5.2: a) Sample X-PEEM color coded composite map (non-rescaled) derived from a singular value decomposition (SVD) analysis, using the PEO, PETA and HSA reference spectra (Fig. 1), of a C 1s image sequence (23 energies) recorded from a spun-cast PEO blend with 10% PETA contribution. b) Mask used to extract spectra of specific regions. Red denotes PEO-rich regions, green denotes PETA-rich regions, defined by threshold masking the PEO and PETA component maps. The remaining blue pixels define areas at the interface between the PEO-rich and PETA-rich domains and were not used in the fitting procedure. c) Curve fit of the average C 1s spectra of the PEO-rich region (data, dots; fit, black line; components, colored lines) d) Curve fit of the average C 1s spectra of the PETA-rich region (same color coding).

PEO-rich and PETA-rich areas were examined quantitatively by applying a threshold mask to the stack to obtain pixels specific to PEO or PETA (Figure 5.2). Only pixels above a defined value were included and the average NEXAFS spectrum from each masked region was further altered by setting the pre-edge intensity to zero. Each

PEO-rich or PETA-rich average NEXAFS spectrum was then fit with the PEO, PETA and HSA reference spectra. For each type of sample several stacks were quantitatively examined and the results were averaged to determine the uncertainty or standard deviation.

5.3. Results and Discussion

The C 1s reference spectra for PEO, PETA and HSA are plotted in Figure 5.1. The three species can be easily distinguished at the C 1s edge. The PEO spectrum is dominated by C 1s $\rightarrow \sigma^*_{C\text{-}H}$ and C 1s $\rightarrow \sigma^*_{C\text{-}O}$ transitions at 289.0 and 289.8 eV [78]. PETA is characterized by two main transitions at 284.5 and 288.6 eV corresponding to C 1s $\rightarrow \pi^*_{C=C}$ and C 1s $\rightarrow \pi^*_{C=O}$ transitions. The C=C π^* transition at 284.5 eV is 0.7 eV lower than the corresponding C 1s $\rightarrow \pi^*_{C=C}$ transition in polystyrene due to conjugation of double bonds in the PETA structure. HSA shows a strong C 1s $\rightarrow \pi^*_{C=O}$ transition at 288.20 eV, which is 0.4 eV lower than the C 1s $\rightarrow \pi^*_{C=O}$ transition of PETA due to the less electronegative environment of the carbon atom in the amide-group of proteins.

The color coded maps of the PEO films with 1.5, 5 and 10 wt-% PETA crosslinker obtained from X-PEEM are shown in Figure 5.3. The same data are presented in two different ways. In the rescaled maps (d, i, n) the intensity of each component is mapped separately to the full range of its color (0-255), resulting in greater sensitivity for the localization of each component. In the absolute maps (e,j,o) the intensity of each component is displayed on a common scale (0-10 nm), which preserves the thickness information.

The rescaled color coded image for the 1.5 wt-% PETA sample (Figure 5.3d) reveals an inhomogeneous surface with small PETA domains (~ 50 nm) scattered within a PEO matrix, with PEO, PETA and HSA color coded as red, green and blue, respectively. These small PETA domains are hard to resolve and may be beyond the resolution limits of the X-PEEM used for these studies. As the concentration of crosslinker increases, the surface evolves from slightly structured to having large circular domains of green crosslinked PETA. With increasing crosslinker concentration, the images become pinker and teal, indicative of HSA adsorption to the entire surface. At the highest PETA concentration studied (10 wt-%), there is a marked correlation between the green dots of PETA and intensely blue HSA (Figure 5.3n).

The absolute color coded images show the surface changing from bright red (Figure 5.3e) to bright green (Figure 5.3o) as the concentration of PETA increases from 1.5% to 10%, suggesting that surface enrichment of PETA occurs at the substrate-air interface. In these images, the blue color representing HSA is faint indicating that although PETA segregates to the surface, the PEO still retains some protein resistance.

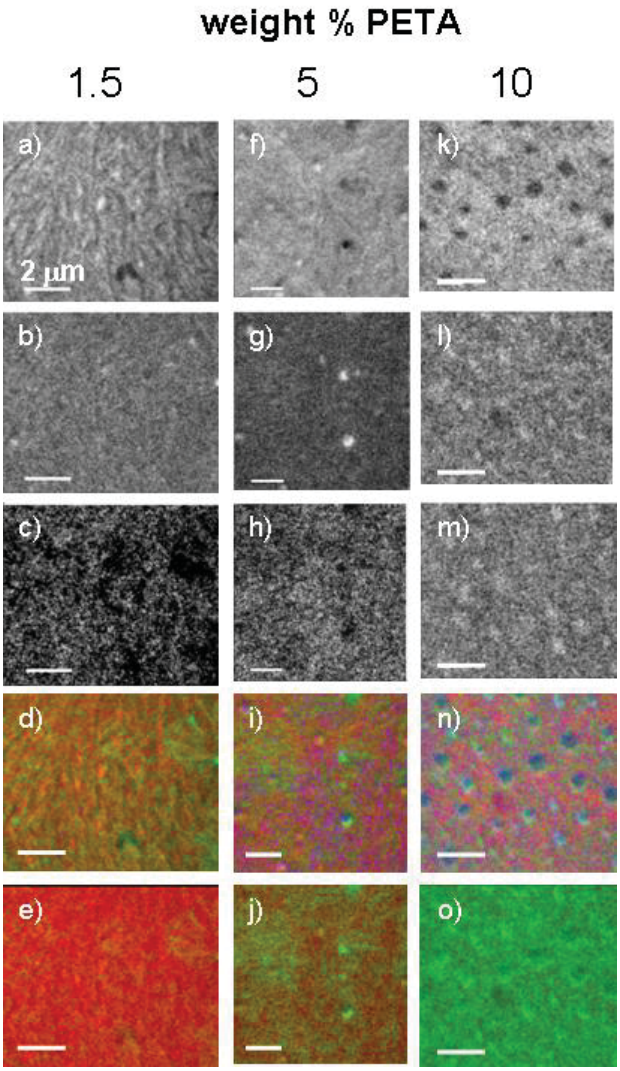

Figure 5.3: X-PEEM color coded composite maps of PEO with 1.5% PETA crosslinker a) PEO, b) PETA, c) HSA, d) rescaled, e) absolute; PEO with 5% PETA f) PEO, g) PETA, h) HSA, i) rescaled, j) absolute; PEO with 10% PETA k) PEO, l) PETA, m) HSA, n) rescaled, o) absolute. PEO is coded red, PETA is coded green and HSA is coded blue.

Figure 5.4 compares the average spectra extracted from the 1.5, 5 and 10 wt-% PETA samples compared to pure PEO and pure PETA. As the concentration of PETA increases the main NEXAFS peak shifts to lower energy and the spectral line shape

changes from mainly PEO (1.5% wt- PETA sample) to mainly PETA (10 wt-% PETA sample).

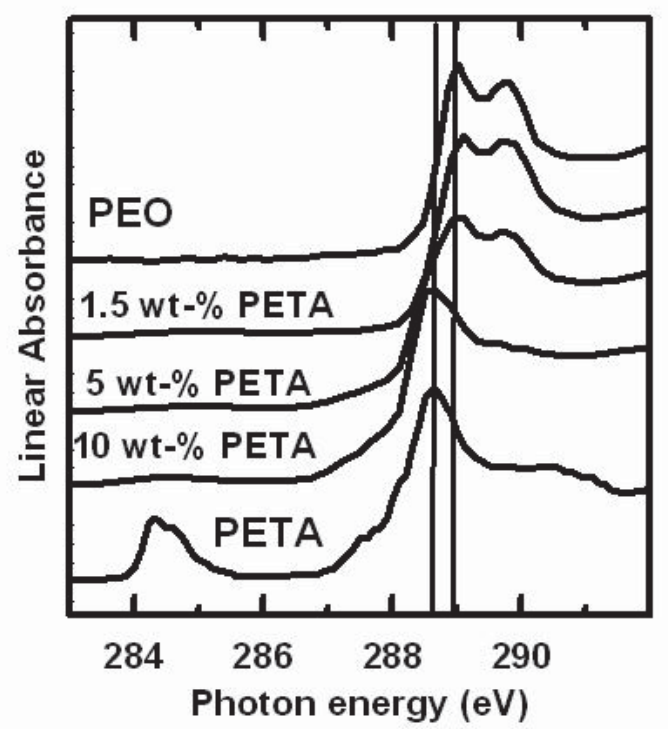

Figure 5.4: C 1s X-ray absorption spectra of PEO with 1.5% 5% and 10% PETA, compared to the spectra of pure PEO and PETA.

Doytcheva et al. suggested that under UV irradiation, PETA (singlet) undergoes an intersystem crossing to form an excited triplet state which is capable of cleaving a proton from PEO to form a PEO radical and a PETA radical [106]. Our experiments verify that PETA acts as both an initiator and a crosslinker since UV irradiation of PEO alone does not form crosslinked PEO. Also, our NEXAFS spectra show almost no intensity in the C 1s $\rightarrow \pi^*_{C=C}$ transition at 284.5 eV, which should be seen if the double bonds of PETA were still present. This clearly indicates that the crosslinking mechanism

occurs by PEO and PETA radical attack of the PETA double bond. FTIR analysis of PEO crosslinked with PETA for micelle formation also showed no evidence of C=C double bonds indicating complete radical polymerization [118]. Furthermore, our crosslinking experiments were performed under a blanket of N2 to exclude oxidation of the double bond by air.

Table 5.1: Thickness (nm) of PEO, PETA, and HSA in PEO-rich and PETA-rich areas for 1 wt% PEO samples with 1.5, 5 and 10 wt-% PETA concentration. These films were exposed to 0.005 mg/mL HSA in DDI water. Uncertainty ±0.5 nm.

Region	Composite	Percent PETA (wt-%)		
	Thickness (nm)	1.5 %	5 %	10 %
PEO	PEO	9.3	5.7	2.2
	PETA	0.7	3.7	6.5
	HSA	0.0	0.7	1.3
PETA	PEO	8.7	4.8	1.6
	PETA	1.3	4.9	7.0
	HSA	0.0	0.3	1.4

The quantitative results extracted from PEO-rich and PETA-rich areas are summarized in Table 5.1. For the 1.5 wt-% PETA sample, a small amount of PETA (0.7 nm) is detected in the PEO-rich area. At this low crosslinker concentration, PEO still retains its non-fouling properties with no detectable HSA adsorption. The PETA-rich area shows an increase of 6 % PETA revealing that PEO remains the dominating component (~ 90 %) across the top 10nm of the surface. HSA is not detected, even in the PETA-rich areas.

However, as the concentration of PETA increases to 5 wt-%, a detectable amount of HSA adsorbs to the surface. At 5 wt-% PETA, the crosslinker thickness in the PEO-rich areas increases from 0.7 nm to 3.7 nm, while in the PETA-rich area, it increases by almost four-fold to 4.9 nm. At this relatively low PETA concentration (5 wt-%), the top 10 nm of the surface shows a mixture of ~ 50:50 PEO:PETA with 0.3 - 0.7 nm of HSA. These results show that PETA is strongly surface segregated. Typically, if there is sufficient mobility in polymer systems, the component with the lower surface free energy segregates to the surface [119]. Since PETA is more hydrophobic than PEO [108], PETA should have lower surface free energy and would be expected to segregate to the surface [120,121]. Furthermore, the molecular weight difference between PETA and PEO should also affect the surface composition with the lower molecular weight PETA segregating to the surface [122].

At 10 wt-% PETA, the crosslinker becomes the dominant component (65-70%) at the surface for both the PEO and PETA-rich regions. Here, the thickness of adsorbed protein doubles to 1.3 - 1.4 nm across the entire surface with only a small amount of PEO (15-20%) detectable. These quantitative results show that at a crosslinker concentration > 5 wt-%, the PEO surface begins to lose its non-fouling properties and begins to adsorb protein. As the concentration of PETA increases, the amount of adsorbed HSA also increases, suggesting that HSA binds preferentially to the crosslinker. Furthermore, small regions of PETA enrichment in the surface below the spatial resolution of the X-PEEM microscope may also cause irreversible protein adsorption to those regions of the surface.

Recently, fluorescence microscopy treated by integral geometry analysis was used to quantify the adsorption of labeled lentil lectin (LcH) or concavalin A (ConA) to several polymeric surfaces including PEO crosslinked with PETA [123]. While this technique can spatially resolve and quantify lectin adsorption to the surface, it provides no information on the polymeric substrate. This fluorescence study suggested that lectin adsorption may be influenced to some extent by the presence of PETA; however, since the spun-cast PEO film studied was prepared using 15% PETA, the crosslinker is undoubtedly the dominant component of the film surface.

The inclusion of PETA and other UV-initiated radical crosslinkers [104] to form PEO-based biomaterials such as hydrogels [102, 107] or micelles [108] for drug delivery is becoming increasingly common. In the formation of micelles, PETA is used to stabilize the hydrophobic core [108] and is likely not present at the air-substrate interface. However, for hydrogel or micro-array applications, it is likely that the highly surface active PETA crosslinker is present as a major component at the interface, and as such may compromise the antifouling properties of PEO.

5.4. Conclusions

PEO containing 1.5, 5 and 10 wt-% PETA was crosslinked by UV exposure, exposed to 0.005 mg/mL HSA and examined with X-PEEM. As the concentration of PETA increased, it became the dominant component in the top 10 nm of the surface. Upon exposure to HSA, increased protein adsorption was seen with increasing PETA

concentration. It is concluded that at PETA concentrations above 5 wt-%, PEO begins to lose its non-fouling properties.

CHAPTER 6: AN X-RAY SPECTROMICROSCOPY STUDY OF PROTEN ADSORPTION TO A POLYSTYRENE-POLYETHYLENE OXIDE BLEND

Polystyrene (PS) was combined with polyethylene oxide (PEO) to form a blend film. Although the surface was not completely phase segregated, protein adsorption to the film still gave insight into how PS affects the protein repellency of PEO, and vice versa. The results showed that the incorporation of PEO into PS reduced the protein adsorption on PS. However, included PS in the PEO areas compromised the protein repellent nature of PEO.

Author contribution

The author of this thesis contributed to this publication in the following ways: all sample preparation, all AFM results, acquisition of the X-PEEM data, all X-PEEM data analysis, and the first draft of the manuscript. Andreas Scholl provided help with the sample transfer.

CHAPTER 6: AN X-RAY SPECTROMICROSCOPY STUDY OF PROTEN ADSORPTION TO A POLYSTYRENE-POLYETHYLENE OXIDE BLEND

6.1. Introduction

Biofouling, or the uncontrolled accumulation and persistent adhesion of biological material to surfaces, occurs when the surface fails to replicate the natural structure and function at the contact site [124,125]. The initial step in this biological cascade begins with rapid adsorption of proteins to the material surface [2]. Thus investigation of selectivity in the first steps of protein adsorption to candidate biomaterials can give insights into mechanisms of biocompatibility.

Polyethylene oxide (PEO) and polyethylene glycol (PEG)–based composites are important blood compatible materials [126,127]. Self assembled monolayers (SAMs) of PEO [128] and also PEO-grafted polymers [129] have been documented to show low bioadhesion, with the short, highly dense PEO chains (‘brush’) preventing the protein from “seeing” the underlying substrate [130]. High molecular weight PEO is also effective in preventing protein adsorption, with the polymer strands at the surface forming loops and tails extending into the aqueous medium [131]. PEO has been blended with a variety of synthetic and natural materials such as polylactide [132], collagen [133], Bombyx mori silk [134], and many others to form fibers, scaffolds and drug carriers with improved biocompatibility and stealth capabilities.

PEO is a water soluble polymer and mass loss occurs upon exposure to protein solution. Several techniques to crosslink PEO have been successful, including γ [100], UV [104,102,135] and electron irradiation [103]. In particular, UV-initiated crosslinking

of PEO with pentaerythritol triacrylate (PETA) was shown to occur even in the solid state [106]. Fluorescence microscopy obtained via integral geometry analysis showed that a PEO surface crosslinked with PETA resulted in the least amount of adsorbed lectin compared to poly(methyl methacrylate) (PMMA) or polystyrene (PS) surfaces [123].

Although many claims of PEO-based non-fouling surfaces are available in patents and the literature, Kingshott and Griesser caution that detailed and reliable characterization of the candidate biomaterial surface must be completed to exclude problems such as contamination and surface defects, followed by a sufficiently sensitive technique to measure amounts and locations of protein adsorption [124].

X-ray spectromicroscopy based on surface sensitive X-ray photoemission electron microscopy (X-PEEM) has been shown to be an effective spatially-resolved technique for surface characterization, and also quantification of biomolecules adsorbed to the surface of model biomaterials, with the advantage that it can simultaneously probe the near-surface region of the substrate since its sampling depth (~10 nm) encompasses both the adsorbed biomolecules and the outer regions of the substrate.

Herein, we report the chemical composition and surface morphology of PS-PEO thin films spun cast from various mass ratios and polymer concentrations, followed by evaluation of these surfaces as candidate biomaterials. Previously, Grainger, et al. also saw that the incorporation of PEO to PS resulted in decreased protein adsorption. Their study varied the amount of the hydrophilic component in their PS-PEO block co-polymer films and found decreased HSA adsorption with increasing hydrophilic ratios [136]. Furthermore, although the minimum amount of protein adsorption for single

protein solutions were found on the surfaces with 40% PEO ratios, the same protein repellency was not found for multi-component protein or plasma solutions, suggesting that single protein experiments may be too much of a simplification of the *in vivo* processes [137].

Moreover, films created from di-block copolymers of PS-PEO, which formed PEO nanocylinders in a matrix of PS, were also shown to significantly reduce the adsorption of bovine serum albumin (BSA), lysozyme, and fibrinogen (Fg) compared to control PS surfaces [138]. Protein adsorption in that study was characterized in bulk by quartz crystal microbalance with dissipation (QCM-D), and qualitatively with atomic force microscopy (AFM). In our study, we spatially map the distribution of HSA across the surface of the PS-PEO blends, and quantify the amount of HSA adsorbed to the PS, PEO and interface regions.

This present study is part of an on-going effort to provide insight into the interaction of blood and blood components with phase-segregated and patterned model biomaterials. These results are intended to contribute towards further understanding of the fundamentals of protein adsorption, which may lead to the development of improved blood- and tissue-contacting medical devices.

6.2. Materials and Methods

Please see chapter 2 for information on the materials, substrates, protein exposure, AFM, and X-PEEM set-up.

6.2.1 X-PEEM Data Analysis

The C 1s reference spectra for PS, PEO and HSA are presented in Figure 6.1. At the C 1s edge, the spectra can be easily differentiated with PS characterized by its C 1s → $\pi^*_{C=C}$ transition at 285.15(3) eV, HSA by its strong C 1s → $\pi^*_{C=O}$ transition at 288.20(6) eV, and PEO by C1s → σ^*_{C-H} and C1s → σ^*_{C-O} transitions at 289.03(8) and 289.78(8) eV, respectively [78].

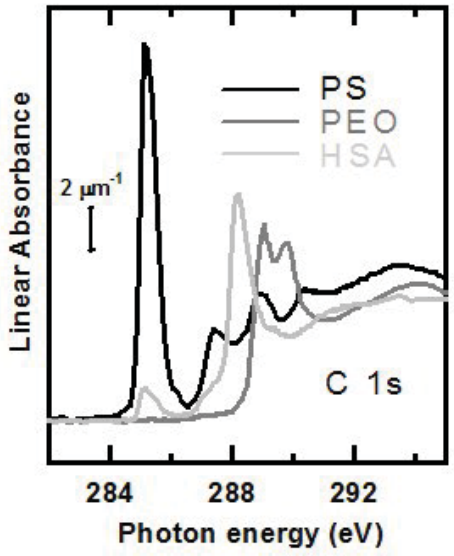

Figure 6.1: C 1s X-ray absorption spectra of polystyrene (PS, black), polyethylene oxide (PEO, dark gray) and human serum albumin (HSA, light gray), recorded with STXM. The spectra are plotted on an absolute linear absorbance scale.

The aXis2000 software package was used to perform data analyses [83]. C 1s image sequences were aligned if necessary, normalized to the ring current and divided by the I_0 spectrum collected from a clean, HF-etched Si(111) chip. The I_0 spectrum was corrected for the absorption of the underlying silicon and a factor proportional to the

photon energy representing the bolometric response of the X-PEEM detection. All carbon stacks were calibrated by assigning the C 1s → $\pi^*_{C=C}$ transition of PS to 285.15 eV.

Singular value decomposition (SVD) is an optimized method for least squares analysis in highly over-determined data sets [116,117] and was used to fit each pixel of the C 1s image sequence with PS, PEO and HSA reference spectra. The fit coefficients generated from the SVD analysis are presented as component maps which are the spatial distributions of each component. A heavily smoothed image arising from the sum of the component maps was used to correct skewed illumination by dividing each component map with the smoothed image. Finally, the intensities were adjusted by dividing the intensity of each image in the image sequence by a scale factor which resulted in a total average thickness (sum of all components) of 10 nm, corresponding to the sampling depth of X-PEEM [75].

Figure 6.2 shows an example of the methodology to extract quantitative results. After fitting to obtain component maps (presented as a color coded composite in Fig. 6.2a), a threshold mask was applied to each component map to isolate specific pixels corresponding to PS, PEO or the interface. Figure 6.2b shows the color coded combination of the masks used in this example. The averaged spectrum from all pixels with a component signal above a threshold value was extracted. The resulting average NEXAFS spectrum for each of the three regions was further modified by setting the pre-edge intensity to zero. The spectra of each region (Fig. 6.2c,d,e) were then fit to the pre-edge background subtracted PS, PEO and HSA reference spectra. Several stacks obtained from different regions of the same sample were analyzed as independent repeat

measurements and the final quantitative results were averaged with the uncertainties from these multiple determinations used as the standard deviation.

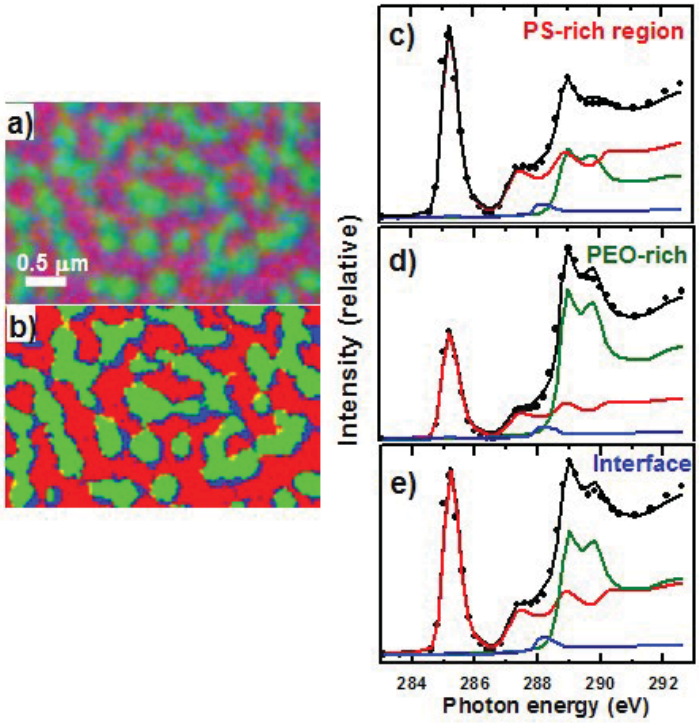

Figure 6.2: Example of analysis procedures for a C 1s image sequence (23 energies) recorded from a PS/PEO blend thin film spun-cast from a dichloromethane solution with a total loading of 0.5 wt% polymer in a 60:40 PS:PEO ratio with 0.05 mg/mL adsorbed HSA. a) Color coded composite (non-rescaled) of the PS (red), PEO (green) and HSA (blue) component maps derived from singular value decomposition (SVD) using the pure species reference spectra (Fig. 1). b) Mask used to extract spectra of specific regions. Red denotes PS-rich regions, green denotes PEO-rich regions, defined by threshold masking the PS and PEO component maps. The remaining blue pixels define areas at the interface between the PS-rich and PEO-rich domains. c) Curve fit of the average C 1s spectrum of the PS-rich region (data, dots; fit, black line; components, colored lines) d) Curve fit of the average C 1s spectrum of the PEO-rich region (same color coding) e) Curve fit of the average C 1s spectrum of the interface region (same color coding).

6.3. Results and Discussion

6.3.1 Substrate Characterization

6.3.1.1 Atomic Force Microscopy (AFM)

AFM was used to verify that the PEO was crosslinked and polymer did not leach into aqueous solution upon exposure to water. A PS-PEO 40:60 film was spun cast from dichloromethane and the same surface was imaged prior and after water exposure (Figure 6.3). The surface morphology remained the same, even though the AFM images were taken at different locations, showing that the film surface did not dissolve/leach after exposure to water for 20 minutes. While we imaged the dry polymer before wetting and then waiting for the polymer to dry again before imaging, it would be an interesting experiment to image the surface under hydrated conditions to see if there is an effect arising from hydration.

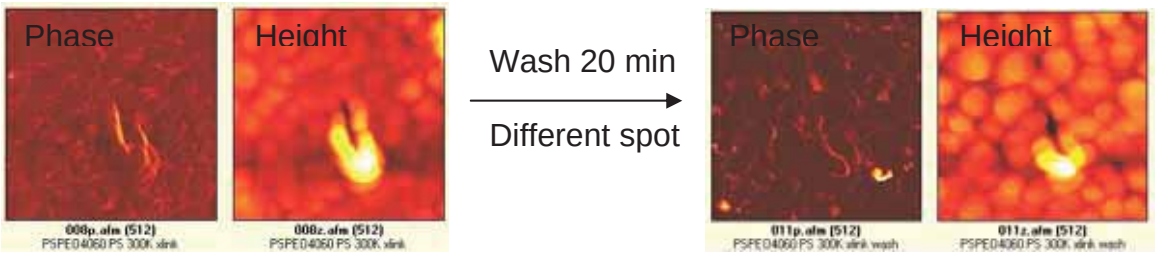

Figure 6.3: AFM height and phase mode images for a PS-PEO 40:60 film imaged before and after immersion in DDI water for 20 min.

Four films with PS:PEO 20:80, 40:60, 60:40 and 80:20 composition were spun cast from dichloromethane (1 wt%), UV crosslinked, and imaged with AFM. These films are ~300 nm thick as determined by AFM imaging across a scratch in each film (results not shown). AFM phase mode images (Figure 6.4a,c,e,g) reveal interesting microstructure in the 500– 2000 nm range for all four films. The similar color shading in

all four phase images indicates that similar phases / polymer components exist at each surface.

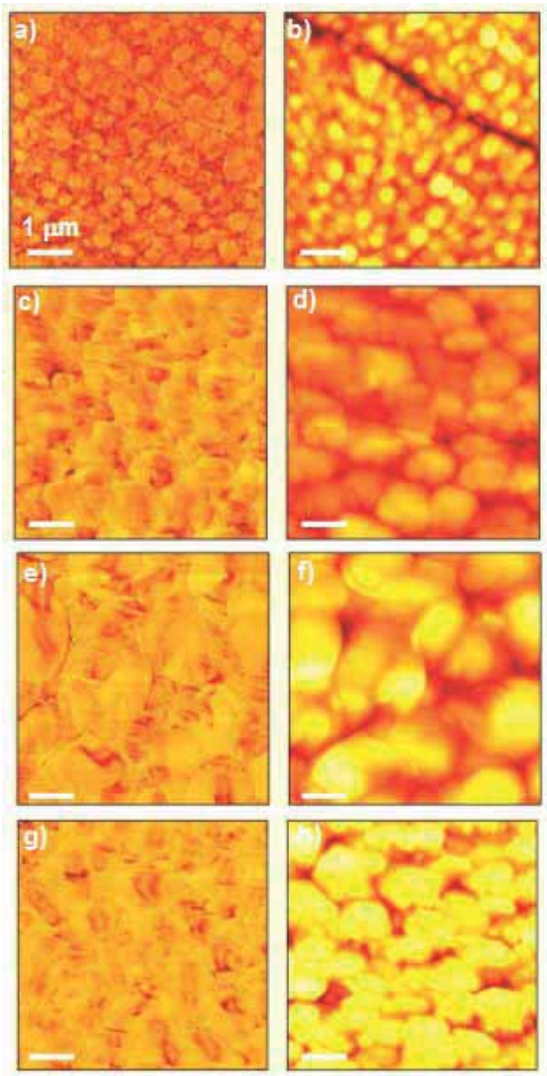

Figure 6.4 AFM phase mode images of PS:PEO thin film blends spun cast from a 1 wt% dichloromethane solution loaded with a) 20:80 w/w ratio, c) 40:60 ratio, e) 60:40 ratio, g) 80:20 ratio. AFM height mode images b) 20:80 ratio, d) 40:60 ratio, f) 60:40 ratio, h) 80:20 ratio. AFM images are 5 µm x 5 µm.

The height mode images (Figure 6.4b,d,f,h) show that the more yellow-colored domains increase in size laterally from ~500 to 1000 nm, as the PS:PEO ratio changes

from 20:80 to 80:20. Naively these domain size changes would suggest that the small domains seen in the PS:PEO 20:80 film and the larger domains seen in the PS:PEO 80:20 film are composed mainly of PS. However, polymer identity is difficult to determine by AFM without polymer destruction or verification with a chemically sensitive technique [139,140,141], and there are many cases known where there is little or no correlation between bulk and surface composition.

Samples for X-PEEM analysis need to be considerably thinner in order to have adequate conductivity to avoid charging that occurs along extruded structures (ie. low rugosity films are required). Thus, in order to obtain samples suitable for X-PEEM analysis the PS:PEO 40:60 and 60:40 solutions were diluted to 0.5 wt% and spun cast under otherwise identical conditions. The height mode images shown in Figure 6.5 reveal a regular, randomly patterned film surface. A close inspection of the morphology of these films reveal the PS:PEO 40:60 surface to be composed more of a classic dispersed droplet compared to more oblong structures in the PS:PEO 60:40 film. The pattern from the height mode images is observed faintly in the phase mode images, suggesting incomplete phase separation but to a relatively small extent since there is very minor color shading variation. The thicknesses of the PS:PEO 40:60 and 60:40 films determined by AFM across a scratch are 130(5) and 147(5) nm, respectively, suitable for X-PEEM analysis.

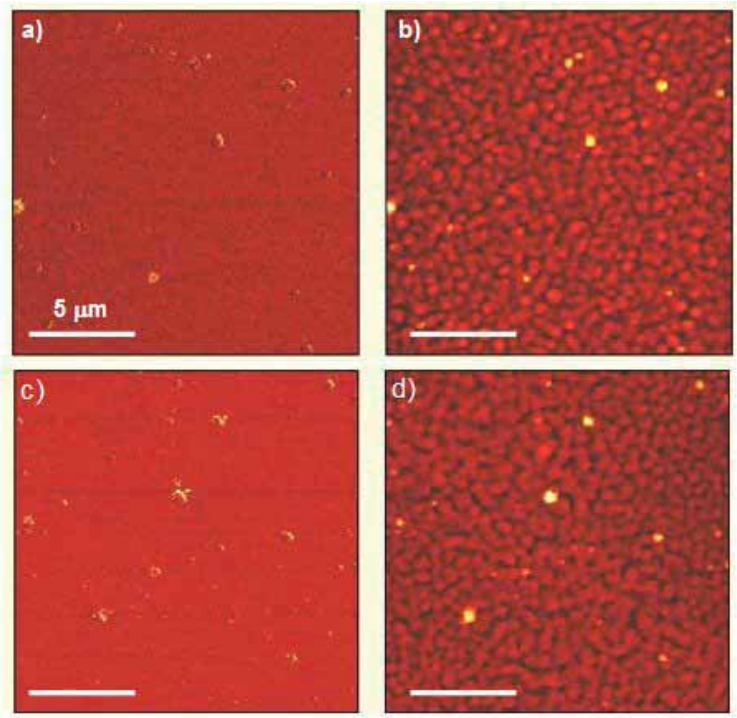

Figure 6.5: AFM phase mode images of PS:PEO thin film blends spun cast from a 0.5 wt% dichloromethane solution loaded with a) 40:60 w/w ratio, c) 60:40 ratio. AFM height mode images b) 40:60 ratio, d) 60:40 ratio. AFM images are 15 μm x 15 μm.

6.3.1.2 X-PEEM Analysis

Figure 6.6 presents two different presentations of the color coded composites of the PS and PEO component maps derived from SVD fitting of C 1s image sequences measured from the unannealed PS:PEO 40:60 and PS:PEO 60:40 thin films (0.5 wt% from CH_2Cl_2, UV irradiated to crosslink the PEO component). The maps on the left are rescaled such that the intensity of each component is scaled separately to the full range (0-256) of its color, resulting in greater sensitivity to the spatial distribution of each component. The maps on the right are displayed on a common absolute scale (0-10 nm), which preserves the true compositional information.

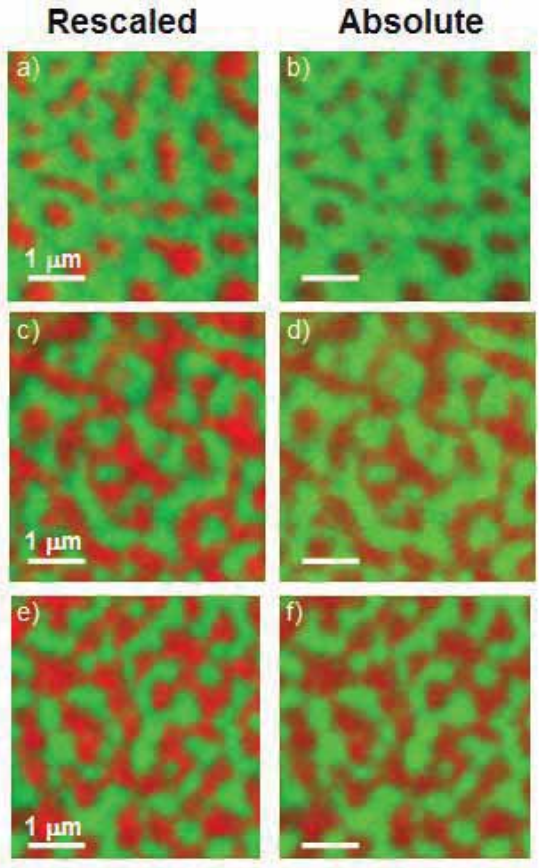

Figure 6.6 Color coded composite maps derived from C 1s X-PEEM image sequences of (a,b) 40:60 (w/w) PS:PEO, (c,d) 60:40 PS:PEO , and (e,f) 60:40 PS:PEO annealed films cast from 0.5 wt% dichloromethane solutions. The left maps (a,c,e) are rescaled while the right maps (b,d,f) are on an absolute scale. PS is coded red, PEO is coded green.

The rescaled color coded images verify the different surface morphologies for the two films obtained from AFM, with the discrete domains of the PS and PEO exhibiting classical dispersed droplet and worm-like structures, respectively, for the PS:PEO 40:60 (Figure 6.6a) and 60:40 films (Figure 6.6c). As the mass ratio changes from PS:PEO 40:60 to 60:40, a phase inversion is seen as the red-colored PS component alters from discrete domains to the continuous phase, and vice versa for the green-colored PEO component. For polymers with similar viscosities, the phase inversion point occurs when

the composition of two blended polymers is approximately equal [142], which in this case is close to 50:50. The crosslinked PEO regions are bright green in the absolute images of the PS:PEO 40:60 (Figure 6.6b) and 60:40 films (Figure 6.6d), suggesting these regions are pure PEO. In contrast, the red PS regions for both films show a much more green color indicative of incomplete phase segregation.

The X-PEEM spectral fitting results obtained for the two polymer thin films quantifies the partial phase separation (Table 6.1). Here, the PS or PEO region is defined as the pixels with the most red or green color, respectively, and is considered especially "PS-rich" or "PEO-rich". For the PS:PEO 40:60 substrate, the quantitative results reveal that the PEO region is dominated by 8.2(5) nm of PEO while only 1.8(5) nm of PS is detected. This small amount of PS likely arises from trapped PS micro-domains with sizes below the spatial resolution of the X-PEEM microscope. The dominant component in the PS region for this film is also PEO (5.5(5) nm) with only 4.4(5) nm of detected PS.

Table 6.1: Composition of PS and PEO (%/pixel) in the PS-rich and PEO-rich regions of PS:PEO blends with respect to polymer ratios, total polymer concentration and annealing. Uncertainty ±0.5 nm.

Region	Component	Polymer ratios		Annealing
		PS:PEO 40:60		PS:PEO 60:40
		40:60	60:40	18h at 160 C
PS	PS	4.4	7.1	7.4
	PEO	5.5	2.9	2.6
PEO	PS	1.8	3.3	3.4
	PEO	8.2	6.7	6.6

(1) Total film thickness (nm) as measured by AFM. Uncertainty estimated from repeat measurements over a scratch made with a sharp tweezer tip.

Similar quantitative results are observed in the PEO region of the PS:PEO 60:40 film. The PEO region is dominated by 6.7(5) nm of PEO signal, with 3.3(5) nm of detected PS. In contrast, the PS region of this film reveals a greater thickness of PS (7.1(5) nm), resulting from the higher concentration of PS in this system. Still, 2.9(5) nm of PEO is detected, showing that this film remains only partially phase segregated.

Since solvent-cast blends are thermodynamically unequilibrated due to rapid solvent evaporation, the thin film substrates may reach equilibrium by annealing above the glass transition temperature (T_g), leading to greater phase separation [143]. After vacuum annealing for 18 h at 160 °C, above the Tg of both polymers (PS Tg: 110 °C, PEO Tg: -55 °C [144]), the quantitative analysis obtained from X-PEEM revealed no difference between the annealed and unannealed films (uncertainty ±0.5 nm). Even with annealing, some surface enrichment of PEO is seen at the PS region (Table 6.1).

In theory, the surface free energy of each polymer component is useful for predicting surface enrichment, with the lower surface free energy polymer segregating toward the air [145]. In this case, PS has a lower surface free energy (γ_{PEO} = 44 mJ/m^2 and γ_{PS} = 41.0 mJ/m^2 [146,119]). X-ray photoemission spectroscopy (XPS) of blends of low molecular weight diblock and triblock copolymers of PS/PEO and PEO/PS/PEO in various solvents showed PS surface enrichment in the top 5 nm of the film surface [147,148]. However, low molecular weight polymers (10 – 30 K) were used, followed by several applications of dip-coating, which is a more equilibrated method of creating thin films compared to spin coating [147,148]. Moreover, the characterization of these

surfaces was carried out only with non-spatially resolved XPS. Spatially resolved X-PEEM analysis has the ability to detect surface enrichment of PEO even in the PS region.

Furthermore, polar PEO is likely more soluble in polar dichloromethane relative to PS, such that PEO stays dissolved longer in solution and upon spin coating develops an overlayer on the surface [119]. Surface enrichment of PEO has also been found with chitosan blends of PEO [149] and copolymers of PEO-g-PMMA (γ_{PMMA} = 40.2 mJ/m^2) and was attributed to the bulk composition and low T_g of PEO [146]. Since the T_g of PEO is low, PEO segments have greater flexibility and movement compared to PS, thus more PEO is proposed to move towards the surface compared to PS [146].

Although the PS:PEO 60:40 film exhibits incomplete phase segregation, protein adsorption to this surface will provide insight into 1) evaluating protein adsorption to the PEO crosslinked, discrete domains, 2) examining how protein adsorption to a PS surface changes with incorporation of PEO and 3) comparison of the PS:PEO system to the PS:PLA surface previously characterized by X-PEEM [110].

6.3.2 Protein Adsorption

6.3.2.1 Protein Adsorption to the PS-PEO Surface

The unannealed PS:PEO 60:40 film was exposed to 0.005, 0.01 and 0.05 mg/mL HSA, followed by examination with X-PEEM. The rescaled images reveal significant color changes compared to the pure PS-PEO substrate, indicative of protein adsorption to the surface (Figure 6.7a,c,e). At all three concentrations, the blue color representing protein is most concentrated at the interface between PS and crosslinked PEO. This is the

area of the lowest free energy [60]. As the concentration of HSA increases, the PS region changes from red to pink, suggesting a greater amount of blue HSA adsorbing to the surface while the color of the green PEO discrete domains remains similar, suggesting crosslinked PEO is more protein resistant compared to PS.

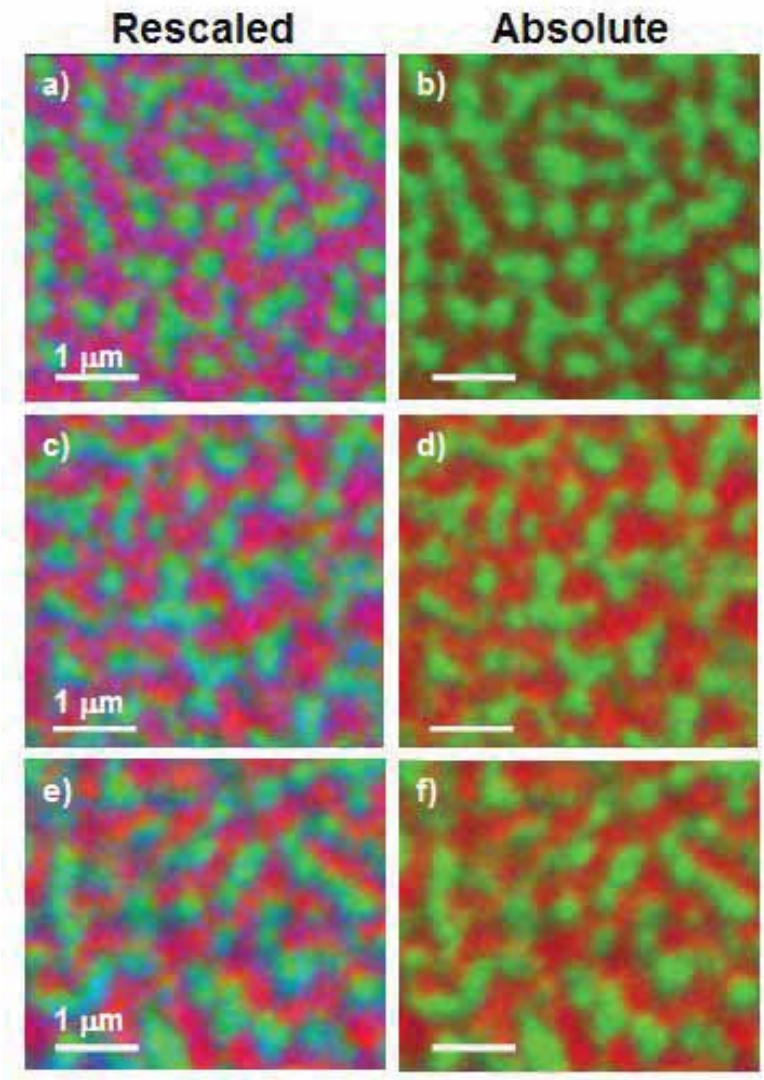

Figure 6.7 Color coded composite maps derived from C 1s X-PEEM image sequences of (a,b) 0.05 mg/mL HSA, (c,d) 0.01 mg/mL HSA, and (e,f) 0.005 mg/mL HSA adsorbed to an unannealed 60:40 PS:PEO film, 0.5 wt% loading. The left maps (a,c,e) are rescaled while the right maps (b,d,f) are on an absolute scale. PS is coded red, PEO is coded green and HSA is coded blue.

The absolute images for the 0.005 and 0.01 mg/mL HSA samples show red and green images comparable to the native substrate, signifying a low amount of adsorbed protein (Figure 6.7b,d). At the highest concentration of 0.05 mg/mL HSA, the red color of the PS continuous phase is darker, suggesting a small adsorbed contribution from the protein. The green color of the discrete domains remains sharply bright, revealing little adsorbed HSA (Figure 6.7f).

Table 6.2: Thickness (nm) of PS, PEO, and HSA in the PS, PEO and interface regions from PS:PEO 60:40 (0.5 wt%) films exposed to 0.05, 0.01, and 0.005 mg/mL HSA from DDI water. Uncertainty: ±0.5 nm.

Region	Composite	HSA concentration (mg/mL)		
	Thickness (nm)	0.05	0.01	0.005
PS	PS	6.1	6.5	6.9
	PEO	3.1	2.7	2.6
	HSA	0.8	0.8	0.5
PEO	PS	2.7	3.8	3.1
	PEO	7.1	5.2	6.2
	HSA	0.8	1.0	0.7
Interface	PS	4.8	5.1	4.9
	PEO	4.3	3.5	4.2
	HSA	1.0	1.4	1.0

The quantitative results indicate that for all concentrations examined, HSA shows preferential adsorption to the interface between the PS and crosslinked PEO domains, which is the area of the lowest free energy (Table 6.2). As the concentration of HSA increases, the thickness of the protein detected on the PS region is almost doubled from 0.005 mg/mL to 0.05 mg/mL. In contrast, the thickness of detected protein on the

crosslinked PEO domains is the same within uncertainties, suggesting that crosslinked PEO is protein resistant at the highest concentration examined (0.05 mg/mL HSA). Still, crosslinked PEO is not completely protein resistant since 0.7 – 1.0 nm of HSA is detectible on the domains.

Previously, we characterized PEO films with the addition of 1.5%, 5% and 10% PETA and found that below a PETA concentration of 1.5% that no adsorbed HSA was detectable via X-PEEM [150]. The amount of PETA used for these PS-PEO crosslinked films is 0.5%. Thus, PETA should not significantly contribute to the detected 0.7-1.0 nm of HSA adsorbed on the crosslinked PEO domains. Rather, the adsorption of HSA arises from the incomplete phase segregation of the PS-PEO films, since the PEO-rich area shows 33% contribution from PS.

Furthermore, a PS:PEO 60:40 film (0.5 wt%) with no PETA and no UV crosslinking was exposed to a 0.005 mg/mL HSA solution (Figure 6.8) for 20 min. The color coded micrographs show very red absolute images, indicative of PS as the dominant component within the top 10 nm of the film surface. Although most of the PEO dissolved into solution, some PEO-rich areas were found. Likely, in these regions the PEO polymer chains were entwined with PS and anchored to the surface.

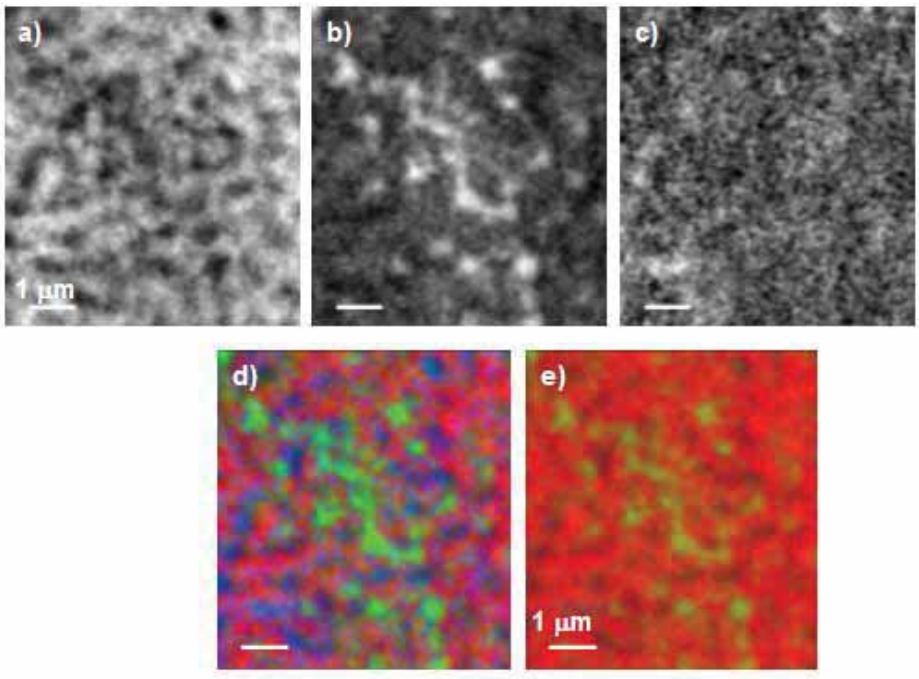

Figure 6.8: a) PS, b) PEO c) HSA component maps derived from a C 1s X-PEEM image sequence of 0.005 mg/mL HSA adsorbed to a non-crosslinked PS:PEO 60:40 (0.5 wt%) film. Color coded composite maps d0 rescaled e) absolute. PS is coded red, PEO is coded green and HSA is coded blue.

The quantitative results verify that PS dominates (60-80%) the entire surface (Table 6.3) with only 3.6 nm of PEO detected in the PEO-rich region. More importantly, the amount of HSA detected on the surface of the non-crosslinked PS-PEO film is within the uncertainty of the amount of HSA detected on the crosslinked PS-PEO film, verifying that at the low PETA concentration used, the crosslinker does not affect HSA adsorption to the PEO-rich regions in this study.

Table 6.3: Thickness (nm) of PS, PEO and HSA in the PS, PEO and interface regions of a non-crosslinked PS:PEO 60:40 (0.5wt%) film exposed to 0.005 mg/mL HSA from DDI water. Uncertainty: ±0.5 nm.

Region	Composite Thickness (nm)	HSA concentration (mg/mL) 0.005
PS	PS	7.9
	PEO	1.5
	HSA	0.6
PEO	PS	6.0
	PEO	3.6
	HSA	0.4
Interface	PS	7.0
	PEO	2.4
	HSA	0.6

6.3.2.2 Comparison to a PS-PLA Spun Cast Surface

In comparison to the PS-PLA 40:60 (0.7 wt%) spun-cast substrate previously characterized by X-PEEM [104], at low concentrations of HSA (0.005 and 0.01 mg/mL HSA) similar protein thicknesses are detected on the PS continuous domains. At higher concentrations (0.05 mg/mL HSA) a significant decrease (0.8 nm) in protein thickness is detected on the PS regions of the PS-PEO blend compared to the PS-PLA blend. This increased protein resistance is attributed to the incomplete phase segregation of PS and PEO in the PS region for the pure substrate. Since the PS area is composed of ~70% PS and ~30% PEO, a significant fraction of high molecular weight PEO is incorporated in this region. This allows for the possibility of extended loops of PEO along the PS surface which may contribute to the increased protein repellency.

The suppression of protein adsorption, platelet adhesion and activation, by PEO has also been observed for monomethyl ether-PEG-b-PLA blends [151], polysulfone (PSf)-g-PEO [126], and blends of chitosan and PEO [149] via XPS and electron spectroscopy for chemical analysis. In the case of the PSf-g-PEO film with 56% grafted low molecular weight PEO (MW 750), no adsorbed bovine serum albumin (BSA) was detected by XPS [126]. We speculate that using densely grafted PS-g-PEO may provide even greater protein resistance compared to the high MW PEO used in this study.

6.4. Conclusions

PS-PEO films spun cast from dichloromethane with various mass ratios and concentrations were characterized by AFM and X-PEEM. Our results show incomplete phase segregation of PS and PEO. The surface enrichment of PEO in the PS region leads to enhanced protein repellency upon protein adsorption. PEO is crosslinked with a very low concentration of PETA and it was found that 0.5% PETA does not affect protein adsorption to the PEO surface. Rather, incomplete phase segregation of the film with 33% PS in the PEO-rich regions led to the detected 0.7-1.0 nm HSA adsorbed to the PEO discrete domains.

CHAPTER 7: AN X-RAY SPECTROMICROSCOPY STUDY OF PROTEIN ADSORPTION TO A POLYSTYRENE-POLY(METHYL METHACRYLATE)-b-POLYACRYLIC ACID BLEND

Polystyrene (PS) was blended with a block copolymer of poly(methyl methacrylate)-b-polyacrylic acid (PMMA-PAA) with the PAA segments being negatively charged under neutral aqueous conditions. Adsorption studies of positively charged SUB-6 peptide and negatively charged HSA to the surface showed that electrostatic interactions were involved. Furthermore, the pH was varied, which changes the charges of both the protein and the substrate. The results showed that the most protein adsorption occurred at pH 4.0, and the adsorption at different pH was also influenced by electrostatic interactions.

Author contribution

The author of this thesis contributed to this publication in the following ways: all sample preparation, all AFM results, acquisition of the X-PEEM data, all X-PEEM data analysis, and the first draft of the manuscript. Rena Cornelius performed the ^{125}I-radiolabeling experiments. Andreas Scholl provided help with the sample transfer.

CHAPTER 7: AN X-RAY SPECTROMICROSCOPY STUDY OF PROTEIN ADSORPTION TO A POLYSTYRENE-POLY(METHYL METHACRYLATE)-b-POLYACRYLIC ACID BLEND

7.1. Introduction

Synthetic materials that are implanted within the body become immediately coated with a layer of proteins upon first contact with blood [2]. This spontaneous protein adsorption may stimulate a foreign body immune response to the material, with the type, amount and conformation of the proteins, and subsequent cell proliferation and differentiation playing a direct role in the inflammatory response [152].

Although the reduction or elimination of adsorbed protein is desirable for medical devices, controlled protein adsorption is important for the development of biochemical sensors [153,154] or in nanofluidic systems [155]. Nonetheless, the reduction or controlled addition of proteins can often be manipulated through electrostatic interactions. For instance, nanopatterning of carboxyl-terminated self assembled monolayer (SAMs) with lysozyme protein for biosensors applications show protein patterns formed from the attraction of positive protein with the negative surface [156] while electrostatic repulsion can reduce [157] but not always prevent protein adsorption [17].

The main driving forces for protein adsorption include electrostatic interactions, hydrogen bonding, van der Waals forces, and hydrophobic interactions [158]. Previously, studies of protein adsorption to polystyrene-poly(methyl methacrylate) (PS-PMMA) or PS-polylactide (PLA) films investigated with a synchrotron-based soft X-ray

photoemission electron microscope (X-PEEM) revealed hydrophobic interactions as a dominant adsorption mechanism [59-61,110-112]. However, most of the polymeric surfaces analyzed thus far with X-PEEM have been neutral and hydrophobic. Thus, a new negatively charged surface was engineered by blending PS with a block co-polymer of PMMA-b-polyacrylic acid (PAA) (or PMMA-b-PAA) to form a partially negatively charged surface at neutral pH under aqueous conditions to probe electrostatic interactions.

X-PEEM is an ideal tool to map the distribution of protein on polymeric surfaces since this technique combines surface sensitivity (top 10 nm of the film surface) with a spatial resolution of approximately 80 nm. Although techniques such as atomic force microscopy (AFM) [39,159] or transmission electron microscopy (TEM) [40] yield better spatial resolution, X-PEEM provides outstanding chemical information obtained via near-edge X-ray absorption fine structure (NEXAFS) spectroscopy.

In this study, we report the chemical composition and surface morphology of PS/PMMA-b-PAA thin films, and electrostatic interactions between negatively charged protein or positively charged peptide to the negatively charged surface, and the effect of pH. These results are compared to those from HSA adsorption under identical conditions to a neutral PS/PMMA surface [59].

This study is part of a series of investigations dedicated to elucidating insights into the interaction of blood components with polymeric, patterned model biomaterials. These results are intended to further the understanding of protein adsorption and the development of medical devices with enhanced biocompatibility.

7.2. Materials and Methods

Please see chapter 2 for information on the materials, substrates, protein exposure, AFM, ^{125}I radiolabeling, and X-PEEM set-up.

7.2.1 X-PEEM Data Analysis

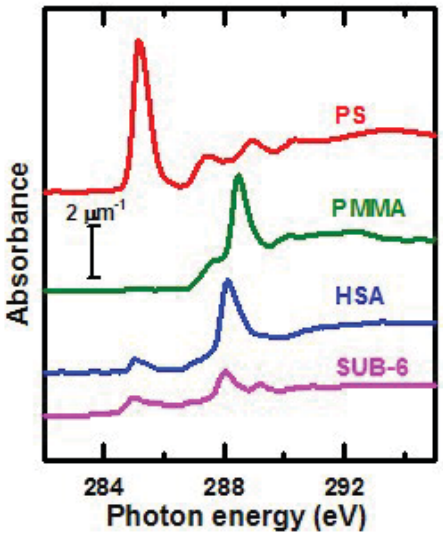

Figure 7.1: C 1s X-ray absorption spectra of polystyrene (PS, red), poly(methyl methacrylate) (PMMA, green), human serum albumin (HSA) (blue) and a cationic peptide (SUB-6, pink), recorded in STXM. The spectra are plotted on an absolute linear absorbance scale with offsets.

The C 1s reference spectra for PS, PMMA, HSA and SUB-6 have been presented previously [111] (Figure 7.1). Here, PMMA is used in place of PMMA-PAA since the spectra of the two are virtually identical. In brief, the PS spectrum is characterized by an intense transition at 285.15(3) eV corresponding to the C 1s → $\pi^*_{C=C}$ transition, PMMA is dominated by an intense transition at 288.45(3) eV corresponding to C 1s → $\pi^*_{C=O}$. HSA shows a strong C 1s → $\pi^*_{C=O}$ transition at 288.20(3) eV and is slightly lower than the transition for PMMA due to the less electronegative environment of the amide group

of the protein backbone. While the C1s spectrum of SUB-6 also exhibits a strong C 1s → $\pi^*_{C=O}$ at 288.20 (3) eV, it has an additional C 1s → $\pi^*_{C=N}$ transition at 289.37(3) eV and significant intensity in the 286 – 287 eV region from the C 1s(C-R) → $\pi^*_{C=C}$ transitions.

All data analyses were performed with the aXis2000 software package [83]. The C 1s stacks were aligned, normalized to the ring current, and divided by the I_0 spectrum. The I_0 spectrum was obtained from a clean, HF-etched Si(111) chip and corrected for the absorption of the underlying silicon and a linear energy term representing the bolometric response of the X-PEEM detection. The C 1s stacks were calibrated by assigning the C 1s → $\pi^*_{C=C}$ transition of PS to 285.15 eV.

Each pixel in the stack was fit to the reference spectra of PS, PMMA and HSA/SUB-6 via singular value decomposition (SVD) which is an optimized method for least squares analysis in highly over-determined data sets [116,117]. The fit coefficients obtained from the SVD fit result in component maps displaying the spatial distribution of each component. Skewed illumination was corrected by dividing a heavily smoothed image obtained from the sum of all component maps. The stack was then divided by a scale factor such that the total average thickness (sum of all components) equaled 10 nm, which is the sampling depth of X-PEEM [75].

A threshold mask was applied to each component map to obtain pixels corresponding to PS, PMMA-b-PAA or the interface (Figure 7.2). Pixels with a component intensity above a certain defined value were averaged to obtain a NEXAFS spectrum specific to each region. The spectrum was further modified by setting the pre-edge intensity to zero. This experimental spectrum was then fitted to the PS, PMMA and

HSA/SUB-6 reference spectra. At least five stacks were obtained from different regions of the same sample and averaged together with the uncertainties from these multiple determinations used for the standard deviation.

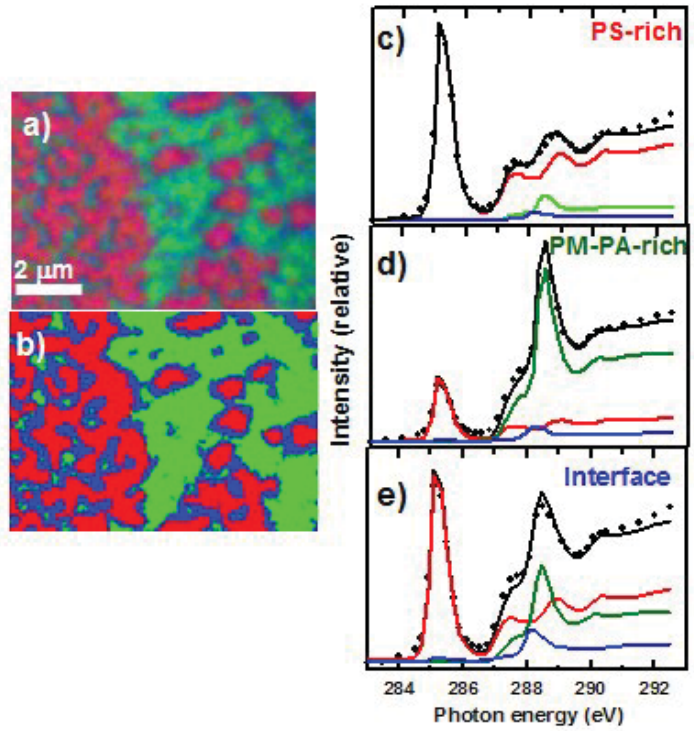

Figure 7.2 a) Sample X-PEEM color coded composite map (non-rescaled) derived from a singular value decomposition (SVD) analysis, using the PS, PMMA and HSA reference spectra (Fig. 1), of a C 1s image sequence (23 energies) recorded from a PS/PMMA-b-PAA 60:40 blend thin film spun-cast from a dichloromethane solution with a total loading of 1 wt% polymer with 0.005 mg/mL adsorbed HSA. b) Mask used to extract spectra of specific regions. Red denotes PS-rich regions, green denotes PMMA-b-PAA-rich regions, defined by threshold masking the PS and PMMA-PAA component maps. The remaining blue pixels define areas at the interface between the PS-rich and PMMA-PAArich domains. c) Curve fit of the average C 1s spectra of the PS-rich region (data, dots; fit, black line; components, colored lines) d) Curve fit of the average C 1s spectra of the PMMA-b-PAA-rich region (same color coding) e) Curve fit of the average C 1s spectra of the interface region (same color coding).

7.2.2 Experiments with Radiolabeled Proteins

HSA was labeled with ^{125}I (ICN Biomedicals, Mississauga, ON, Canada) using the iodogen technique, a standard protocol for radioiodination of proteins with IODO-GEN (Pierce Chemical Company, Rockford, IL). The labeled protein was dialyzed overnight against isotonic Tris buffer to remove unbound radioactive iodide. Trichloroacetic acid precipitation of aliquots of protein solutions before and after completion of the experiments confirmed that >99% of the ^{125}I remained bound to the protein. The adsorption experiments were carried out under static conditions at pH values of 2.0, 4.0, and 8.6. The albumin concentration used was fixed at 0.05 mg/mL with 10% labeled albumin, and the adsorption time was 20 min. After adsorption the surfaces were rinsed statically for 2.5 min using water at the same pH. Each adsorption experiment was performed in four replicates.

7.3. Results and Discussion

7.3.1 Characterization of the PS/PMMA-b-PAA Substrate Surface

PS/PMMA-b-PAA films with mass ratios of 40:60 and 60:40 were spun-cast from dichloromethane (1 wt%) and analyzed with AFM. The phase mode AFM images (Figure 7.3a and c) clearly reveal phase segregated films with domains in the range of 0.5 –1 μm and 2–4 μm, for the 40:60 and 60:40 films, respectively. The height mode images show the domain heights to be ~15(5) and ~20(5) nm, respectively (Figure 7.3b and d). Since the identity of each polymer component is difficult to determine by phase mode AFM without film destruction [139-141], based on the mass ratios, the yellow-colored

component is tentatively assigned as PMMA-b-PAA while the orange colored component is likely PS. As the mass ratio changes from 40:60 to 60:40, a phase inversion occurs with the yellow continuous phase of the 40:60 film becoming the domains in the 60:40 film.

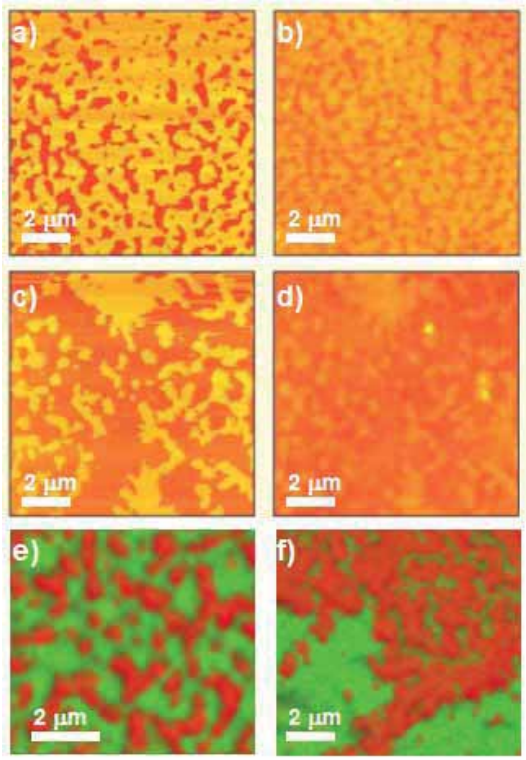

Figure 7.3: AFM phase mode images of PS/PMMA-b-PAA thin film blends spun cast from a 1 wt% dichloromethane solution loaded with a) 40:60 and c) 60:40 PS/PMMA-b-PAA ratio. AFM height mode images b) 40:60 ratio and d) 60:40 ratio. AFM images are 10 µm x 10 µm. X-PEEM color coded composite maps of PS:PMMA-PAA e) 40:60 and f) 60:40. PS is coded red, PMPA is coded green.

The X-PEEM color composite absolute maps are shown in Figure 7.3e and 3f with PS color coded in red and PMMA-b-PAA color coded in green. The X-PEEM maps verify the AFM results, showing that for the 40:60 film, green PMMA-b-PAA is the continuous phase with embedded red PS domains. The X-PEEM maps for the 60:40 films

reveal very small phase segregation with ~ 100 nm thick PMMA-b-PAA domains (green) embedded within continuous regions of PS (red). In addition, areas of very fine phase segregation were inter-dispersed with large domains of pure PMMA-b-PAA (green) up to 5 μm in diameter. Thus, the 10 x 10 μm AFM image for the 60:40 film captured only a portion of the PS-rich area.

The quantitative X-PEEM analysis of the results shown in Fig. 7.3e,f (Table 7.1) showed the 40:60 and 60:40 PS/PMMA-b-PAA films to be well phase-segregated For the 40:60 film, the top 10 nm of PS-rich area contains 8.2(5) nm of PS, while the PMMA-b-PAA-rich area contains 7.1(5) nm of PMMA-b-PAA. The phase segregation improved further for the 60:40 film with 8.3(5) nm of PS in the PS-rich area and 8.4(5) nm of PMMA-b-PAA in the PMMA-b-PAA-rich area. This improvement was likely due to the larger domain sizes of the PS/PMMA-b-PAA 60:40 film. The resulting 1.6 – 1.7(5) nm of the opposite polymer component is likely the result of small microdomains (~ 50 nm) which are below the spatial resolution of the microscope.

Although both the PS/PMMA-b-PAA 40:60 and 60:40 films are phase segregated, the 60:40 film presents larger domains for protein adsorption studies. Since PAA is negatively charged in neutral aqueous solution, the PS/PMMA-b-PAA 60:40 film is useful for studying electrostatic interactions. Firstly, adsorption of positively charged peptide or negatively charged protein to the negatively charged PS/PMMA-b-PAA substrate will be investigated, and secondly, pH effects will be examined.

Table 7.1: Composition of PS and PMMA-PAA (%/pixel) in the PS-rich and PMMA-b-PAA-rich regions of PS/PMMA-b-PAA blends with respect to polymer ratios. Uncertainty ±5 nm.

Region	Component	Polymer ratios PS/PMMA-b-PAA	
		40:60	60:40
PS	PS	8.2	8.3
	PMMA-b-PAA	1.8	1.7
PMMA-b-PAA	PS	2.9	1.6
	PMMA-b-PAA	7.1	8.4

The presence of PAA (the negatively charged polymer) at the surface of the film was verified with fluorescence microscopy. A dilute solution of polylysine-fluorescein was exposed to thin films of PS/PMMA-b-PAA 60:40 and pure PMMA, our control. Only the surfaces with negative charge should bind the positively charged amine group of polylysine.

The fluorescence images reveal the PMMA surface to show no green color indicative of binding fluorescein while the PS/PMMA-b-PAA surface clearly showed fluorescence. The surface shows bands of fluorescence which arises since the sample is not completely flat. Close inspection of the fluorescence image shows the phase segregated pattern where PS-rich domains do not bind fluorescein and remains black (Figure 7.4). Further experiments such as measuring the zeta potential of the PMMA-b-PAA surface will be completed to verify the findings from fluorescence imaging.

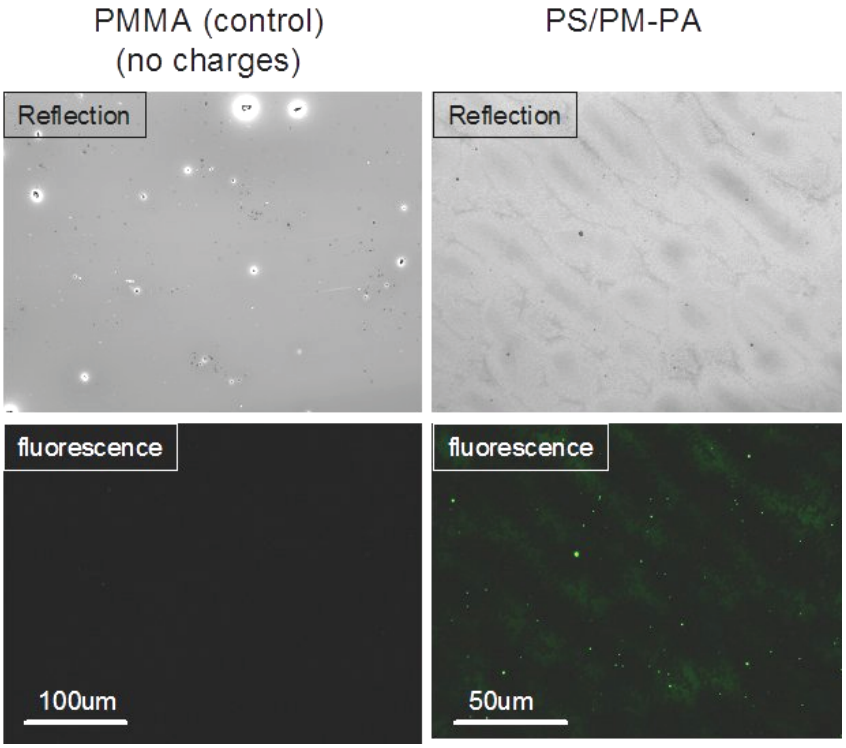

Figure 7.4: Optical images of PMMA and PS/PMMA-b-PAA 60:40 exposed to polylysine-fluorescence. (top) reflection images and (bottom) fluorescence images. Images integrated for 1000 ms, gain 5.

7.3.2 Protein and peptide electrostatic interactions

The PS/PMMA-b-PAA 60:40 substrate was exposed to either 0.005 mg/mL SUB-6 peptide or 0.005 mg/mL HSA protein solutions for 20 minutes and then analyzed with X-PEEM. At neutral pH, SUB-6 is positively charged (+5) while HSA is negatively charged (-15) [160,111].

The color coded composite maps for HSA (upper) or SUB-6 (lower) adsorption to PS/PMMA-b-PAA 60:40 are presented in two different ways (Figure 7.4). The maps on the left are rescaled so the intensity of each component (PS, PMMA-b-PAA and

protein/peptide) is mapped to the full 0-255 color range, which is useful for visualizing the spatial localization of each component. The maps on the right are displayed on an absolute scale (0-10 nm), which preserves the quantitative compositional information.

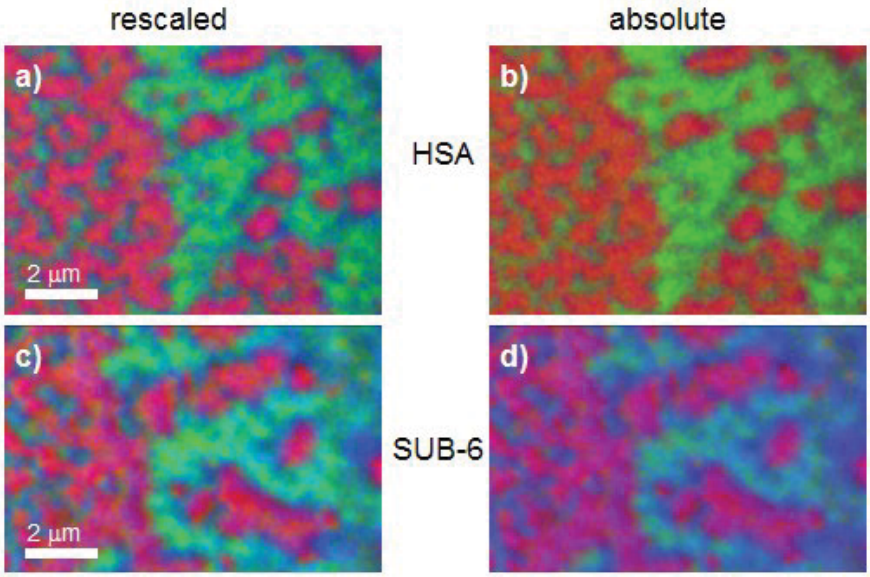

Figure 7.5: X-PEEM color coded composite maps of PS/PMMA-b-PAA 60:40 with 0.005 mg/mL HSA a) rescaled, b) absolute, and 0.005 mg/mL SUB-6 c) rescaled, d) absolute. PS is coded red, PMMA-b-PAA is coded green and HSA/SUB-6 is coded blue.

The rescaled color coded map for HSA adsorption to PS/PMMA-b-PAA is shown in Figure 7.5a, with PS, PMMA-b-PAA and HSA color coded as red, green and blue, respectively. HSA adsorption is strongest at the interdomain interface between PS and PMMA-b-PAA, with some additional protein adsorption to the PS region, which is pink in color. The interface is the area of the lowest free energy [59-61]. The absolute color coded image (Figure 7.5b) still shows the most protein adsorption at the interface, however, now the PS and PMMA-b-PAA colors are much more red and green, respectively, which indicates low protein adsorption to the surface.

The rescaled map for SUB-6 adsorption to the PS/PMMA-b-PAA surface also shows the most peptide adsorbed to the interface, which is strongest in blue color (Figure 7.5c). In contrast to HSA, both the PS and PMMA-b-PAA regions show protein adsorption to the surface, since they are colored in pink and teal. The absolute map of SUB-6 adsorbed to the surface is extremely blue with the most intense blue at the interface between PS and PMMA-b-PAA (Figure 7.5d). Nonetheless, a significant amount of peptide is also adsorbed to the PS and PMMA-b-PAA domains. By comparing the two absolute map (Figure 7.5b and d), it is easily observed that significantly more peptide than protein is adsorbed to the surface.

Table 7.2: Thickness (nm) of PS, PMMA-b-PAA, and HSA/SUB-6 in the PS, PMMA-b-PAA and interface regions from PS/PMMA-b-PAA 60:40 (1 wt%) films exposed to 0.005 mg/mL HSA or SUB-6 from DDI water. Uncertainty: ±0.5 nm.

Region	Composite Thickness (nm)	HSA	SUB-6
PS	PS	7.8	6.2
	PMMA-b-PAA	1.5	0.9
	HSA/SUB-6	0.7	2.9
PMMA-b-PAA	PS	2.1	1.5
	PMMA-b-PAA	7.1	4.4
	HSA/SUB-6	0.8	4.1
Interface	PS	4.9	3.5
	PMMA-b-PAA	3.5	2.2
	HSA/SUB-6	1.6	4.2

The quantitative X-PEEM results support the qualitative analysis - more HSA is adsorbed to the interface (1.6(5) nm) while almost equal amounts of HSA are adsorbed to the PS and PMMA-b-PAA (0.7(5) to 0.8(5) nm) regions (Table 7.2). Since both HSA and

the surface are negatively charged, a repulsive effect is likely present. In fact, HSA adsorption to the negatively charged PS/PMMA-b-PAA surface is more than 50% lower than HSA adsorption to the uncharged PS-PMMA surface at the same concentration [59].

The positively charged SUB-6 peptide shows the opposite adsorption behavior with a large detected adsorbed peptide thickness of 4.1(5) or 4.2(5) nm of SUB-6 on the interface and negatively charged PMMA-b-PAA domains respectively (Table 7.2). Only 2.9(5) nm of peptide is evident on the PS-rich areas. Nonetheless, the amount of peptide adsorbed to the PS/PMMA-b-PAA surface is much higher than the same peptide adsorbed to the uncharged surface [111]. In fact, the adsorption thicknesses of SUB-6 to a charged surface surpasses adsorption from a more concentrated SUB-6 solution (0.01 mg/mL SUB-6) to PS/PMMA, where SUB-6 thicknesses were 1.1(5) nm on PS, 3.0(5) nm on PMMA and 4.2(5) nm at the interface [111]. The increased adsorption of SUB-6 to the PS domains of the charged surface compared to neutral surface is most likely due to adsorption to the microdomains of PMMA-b-PAA embedded within the PS domains.

We propose that electrostatic contributions are the driving force for decreased adsorption of HSA and increased adsorption of SUB-6 to the negatively charged surface. A UV-VIS spectroscopic study of bovine serum albumin (BSA) and lysozyme adsorption to negatively charged silica particles or positively charged AlOOH-coated silica particles found similar results with 90-100% of the protein adsorbed to the oppositely charged surface and almost no (0-10%) protein adsorbed to the surface with the same charge [157]. However, both AlOOH-coated and silica particles are hydrophilic in nature and thus are uncomplicated by the hydrophobic effect.

Indeed, α-lactalbumin was found to adsorb to both a negatively charged Nb_2O_3 and positively charged polylysine surface via optical waveguide lightmode spectroscopy (OWLS), even though α-lactalbumin is negatively charged at pH 7.4 [161]. This adsorption was attributed to the possibility of positive α-lactalbumin patches adsorbing to the negative surface or hydrophobic or entropic factors [162]. Clearly, these factors are also present in the adsorption of HSA to the charged PS/PMMA-b-PAA surface in addition to an electrostatic effect, since HSA adsorption to the negatively charged PS/PMMA-b-PAA surface is reduced but not eliminated.

7,3.3 The effect of pH

HSA (0.05 mg/mL) at pH 2.0, 4.0 and 8.6 were adsorbed to PS/PMMA-b-PAA 60:40 for 20 min. At pH 2.0, HSA is positively charged while the surface is mostly neutral. At pH 4.0, close to the isoelectric point of HSA (IP = 4.7 – 5.3) [163], HSA is slightly positively charged while the surface is negatively charged. And at pH 8.6, both HSA and the surface are negatively charged. HSA itself exists in five different conformations depending on the pH: E, F, N, B, and A [30]. At lower pH, HSA exists in an unfolded and expanded conformation, while at higher pH, HSA is compact.

The color composite maps for HSA adsorbed to PS/PMMA-b-PAA at pH 2.0, 4.0, and 8.6 are presented in Figure 7.6 with PS, PMMA-b-PAA and HSA color coded as red, green and blue, respectively. The maps for HSA adsorption at pH 2.0 (Figure 7.6a,b) and 8.6 (Figure 7.6e,f) reveal a strongly blue interface, which is the area of highest protein adsorption. Qualitatively, similar amounts of HSA are adsorbed to the surfaces at pH 2.0

and 8.6, revealed by similar shades of pink PS and teal PMMA-b-PAA for both maps. Close to the isoelectric point, at pH 4.0, there is so much HSA adsorbed to the PMMA-b-PAA region that almost no green PMMA-PAA is visible (Figure 7.6b-c). The PS region is also strongly colored in pink showing that the greatest amount of HSA adsorbs at pH 4.0.

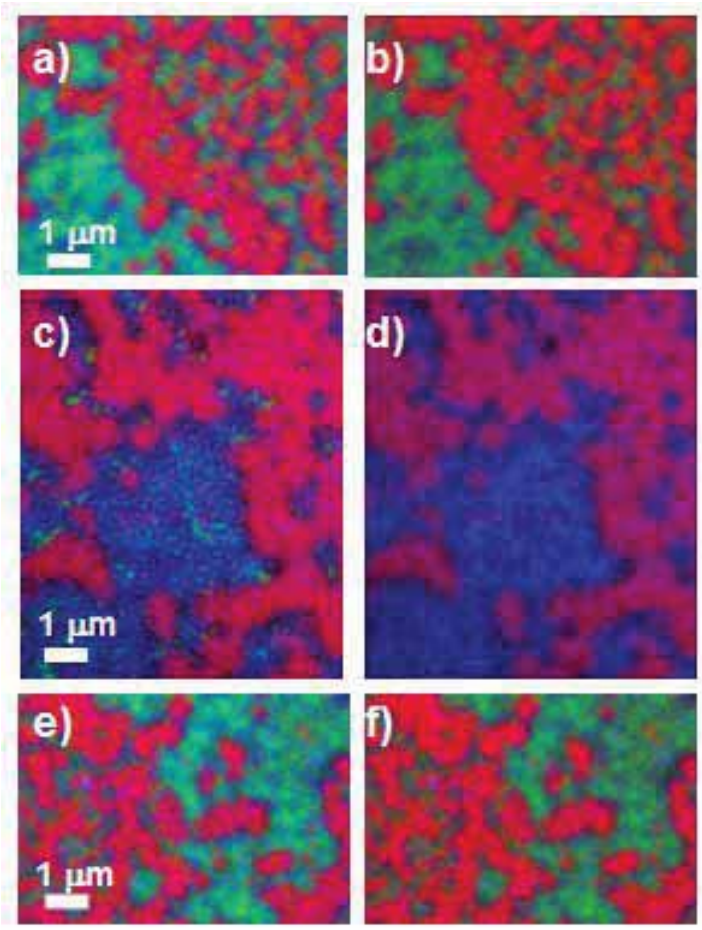

Figure 7.6 X-PEEM color coded composite maps of PS/PMMA-b-PAA 60:40 with 0.05 mg/mL HSA at pH 2.0 a) rescaled, b) absolute, pH 4.0 c) rescaled, d) absolute, and pH 8.6 e) rescaled, f) absolute. PS is coded red, PS-PM is coded green and HSA is coded blue.

At pH 4.0, the quantitative results show HSA adsorbed thicknesses in excess of 4.4(5) nm on the PS/PMMA-b-PAA surface with 7.3(5) nm of HSA adsorbed to the PMMA-b-PAA domains (Table 7.3). Previous studies have shown that the most adsorption occurs at the isoelectric point since the protein carries no charge and thus exhibits the lowest electrostatic repulsion [164,165,166,167]. Since HSA has crystallographic dimensions of 8 x 8 x 3 nm [24], the protein is either adsorbing end-on or forming bilayers. ^{125}I radiolabeling experiments of HSA adsorbed to only PMMA-b-PAA revealed 0.701 μg/cm^2 of HSA on the surface at pH 4.0, 0.05 mg/mL HSA. Theoretically, assuming if HSA is adsorbing end on with dimensions of 8 x 3nm, approximately 0.456 μg/cm^2 would be required to form a monolayer. At pH 4.0, the conformation of HSA is expanded, thus, < 0.456 μg/cm^2 is required for a monolayer. We speculate that HSA adsorption to the PMMA-b-PAA region at pH 4.0 is a combination of monolayer and bilayer adsorption.

HSA adsorption at pH 2.0 and 8.6 are significantly lower compared to pH 4.0 with adsorption values at pH 2.0 and 8.6 in the range of 1.5 – 3.1(5) nm. At pH 4.0, adsorption on PS/PMMA-b-PAA is significantly higher due to electrostatic interactions between the positively charged protein and negatively charged surface. Compared to the uncharged PS/PMMA surface, there is approximately two to three times more adsorbed HSA on PS/PMMA-b-PAA, especially on the PMMA-b-PAA domains. At pH 8.6, adsorption of negative protein to the negative PS/PMMA-b-PAA surface is much greater than adsorption of negative HSA to the uncharged PS/PMMA surface, even though there should be an electrostatic repelling effect between the negative protein and negative

surface. However the thickness value obtained for adsorption of HSA on the uncharged surface (~1 nm) is uncharacteristically low, especially when compared to the radiolabelling results [59].

Table 7.3: Thickness (nm) of PS, PMMA-b-PAA, and HSA in the PS, PMMA-b-PAA and interface regions from PS/PMMA-b-PAA 60:40 (1 wt%) films exposed to 0.05 mg/mL HSA at pH 2.0, 4.0 and 8.6. Uncertainty: ±0.5 nm.

Region	Composite Thickness (nm)	pH 2.0	pH 4.0	pH 8.6
PS	PS	7.4	4.8	7.6
	PMMA-b-PAA	1.1	0.8	0.8
	HSA	1.5	4.4	1.6
PMMA-b-PAA	PS	2.0	1.4	1.4
	PMMA-b-PAA	5.4	1.3	1.8
	HSA	2.6	7.3	3.1
Interface	PS	4.7	4.7	5.2
	PMMA-b-PAA	2.4	2.8	2.1
	HSA	2.9	5.6	2.7

For the PS/PMMA-b-PAA study, the adsorbed HSA thicknesses at pH 8.6 are similar to the thicknesses obtained for pH 2.0. This trend is also seen in the ^{125}I-radiolabelling experiments reported earlier for the pH-dependent X-PEEM study of HSA to neutral PS/PMMA with 0.117, 0.223, and 0.130 μg/cm^2 of adsorbed HSA at pH 2.0, 4.0 and 8.6, respectively [59].

Table 7.4: HSA coverage determined by ^{125}I Radiolabeling experiments[a]

Surface	pH	Coverage μg/cm^2	StdDev
PS-PMPA	2	0.63	0.09
PS-PMPA	4	0.82	0.03
PS-PMPA	8.6	0.24	0.05

[a]HSA adsorption (μg/cm^2) from DDI water or PBS buffer with standard deviations (sd, n = 4).

^{125}I-radiolabelling experiments were also performed for this study with HSA (0.05 mg/mL) adsorption to PS/PMMA-b-PAA at pH 2.0, 4.0 and 8.6 (Figure 7.7, Table 7.4). The same overall adsorption trend was observed, with the most HSA adsorption near the isoelectric point. However, the amount of HSA adsorbed to PS/PMMA-b-PAA was significantly higher than neutral PS/PMMA at all pHs sampled.

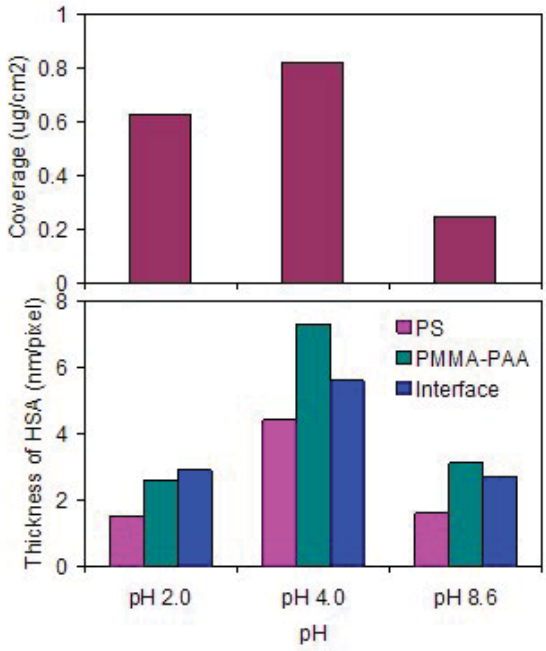

Figure 7.7: (top) ^{125}I radiolabeling derived HSA coverage compared to (bottom) X-PEEM detected thicknesses. Pink denotes HSA thickness observed on PS region, teal denotes HSA thickness observed on PMMA-b-PAA region, and blue denotes HSA thickness observed at the interface.

The greater amount of adsorbed HSA for the PS/PMMA-b-PAA system obtained via ^{125}I radiolabeling may in part be due to the much larger (~5x larger) charged PMMA-b-PAA domains which give rise to more surface area for the electrostatic effect. Furthermore, at pH 2.0, the surface may not be completely charge neutralized, since some other studies are conducted at pH 1.0 to completely protonate the carboxylate groups of PAA [168]. The slightly negative charge of the PAA would then easily attract more HSA compared to the completely neutral PS/PMMA surface.

The large amount of adsorbed HSA at pH 4.0 is clearly due to both adsorption near the isoelectric point and also electrostatic interactions between the positively charged protein and negatively charged surface. Both X-PEEM and ^{125}I radiolabeling show more HSA adsorption to charged PS/PMMA-b-PAA compared to HSA adsorption to neutral PS/PMMA. At pH 8.6, a significantly lower amount of protein is adsorbed as determined by ^{125}I radiolabeling, compared to pH 2.0 and 4.0, likely due to electrostatic repelling of negatively charged protein and negatively charged surface.

Interestingly, the X-PEEM detected thicknesses of HSA are similar at pH 2.0 and 8.6, even though the radiolabeling results show three times more adsorbed HSA at pH 2.0. Although there is a greater amount of HSA adsorbed at pH 2.0, the conformation of HSA at this pH is completely extended (and thinner). In comparison, at pH 8.6, there is less adsorption of HSA, however the structure at alkaline pH is compact, thus giving rise to similar X-PEEM detected thicknesses for the two pH values. Thus, when combined with ^{125}I radiolabelling results, X-PEEM appears to provide useful information with respect to the adsorbed protein conformation.

7.4. Conclusions

X-PEEM and AFM were used to characterize the surface morphology of PS/PMMA-b-PAA spun cast thin films. It was found that the top 10 nm of the film surface was phase segregated. Under neutral aqueous conditions, the surface is partially negatively charged. Electrostatic interactions were seen upon HSA or SUB-6 peptide adsorption to the surface, and also with varying pH where the charges on the substrate and HSA protein were varied. ^{125}I-radiolabelling experiments as a function of pH showed similar trends to the X-PEEM results. In combination with ^{125}I radiolabeling, X-PEEM is capable of indirectly detecting protein conformational changes.

CHAPTER 8: SUMMARY AND FUTURE WORK

8.1 Summary

X-ray photoemission electron microscopy (X-PEEM) and atomic force microscopy (AFM) were used to characterize the surface morphology and phase segregation of a variety of polymer substrates with interesting properties such as biodegradability (PLA), protein resistance (PEO), and adsorption control through electrostatics (PMMA-PAA). Furthermore, protein adsorption studies to these surfaces revealed different and varied adsorption mechanisms.

For blends of polystyrene (PS)-PLA, HSA adsorption to the surface was studied with respect to surface rugosity and ionic strength. The results showed that topography changes in the 35 – 90 nm range had no effect on protein adsorption. Furthermore, X-PEEM showed sensitivity to the adsorbed protein conformation, and was able to detect that the protein existed in an expanded conformation with increasing ionic strength. Measurements at the C 1s and N 1s edge at the same region revealed that multi-edge fitting provides a greater sensitivity for localizing adsorbed protein since only protein contains nitrogen atoms.

The biocompatible polymer polyethylene oxide (PEO) was crosslinked using a UV-initiated crosslinker pentaerythritol triacrylate (PETA). Blends of PEO with 1.5, 5.0 and 10.0 % PETA were obtained, followed by HSA adsorption. The results showed that the PETA crosslinker is highly surface sensitive. As the crosslinker concentration increases, so does the HSA adsorption. Using chemical crosslinkers to immobilize PEO is

becoming increasingly popular in the literature. Hence, care must be taken to ensure that the crosslinker does not compromise the biocompatible nature of PEO.

PS and PEO were blended to form a phase segregated surface with hydrophobic and hydrophilic domains. Although the surface was not completely phase segregated, protein adsorption to this surface still provided insight into evaluating the protein repellency of the PS surface upon incorporation of PEO and vice versa. Addition of PEO to PS resulted in less protein adsorption in the PS region compared to control samples. However, incorporation of hydrophobic PS into PEO compromised the protein repellent nature of PEO.

PS was blended with a block copolymer of poly(methyl methacrylate)-b-polyacrylic acid (PMMA-PAA). The main advantage of incorporating PAA is that it is negatively charged under neutral aqueous conditions. Phase-segregated thin films of PS/PMMA-PAA were prepared. Adsorption studies of positively charged SUB-6 peptide and negatively charged HSA to the surface showed that electrostatic interactions were involved. Furthermore, the pH was varied, which changes the charges of both the protein and the substrate. The results showed that the most protein adsorption occurred at pH 4.0, which is near the HSA isoelectric point, and the adsorption at different pH was also influenced by electrostatic interactions.

8.2 Future Work

This thesis showcases the powerful ability of X-PEEM to simultaneously characterize both the substrate surface, as well as protein/peptide individual or

competitive adsorption for a variety of phase-segregated polymers. X-PEEM can be applied to many other systems relevant to biomaterials including completely phase-segregated PS-PEO blends; engineered surfaces to study biological reactions; examination of lithographic patterns; and to image single protein molecules. These four examples are discussed below as suggestions for near term extensions of this thesis.

8.2.1 Complete phase segregation of PS-PEO

While the X-PEEM study in Chapter 6 examined HSA adsorption to an incompletely phase segregated system, it would be interesting to obtain a completely phase segregated surface of PS and PEO for protein adsorption studies. Since PEO is protein repelling, adsorption of HSA to PS via hydrophobic interactions would likely result in selective protein adsorption, with HSA only adsorbing to the PS and interface regions. This type of system would be interesting from a microarray or nanofluidics perspective.

Recently, a PS-PEO surface was formed by blending low molecular weight polymers (PS MW 64000, PEO MW 42700) crosslinked with 10% PETA, and the surface was found to be phase segregated by means of atomic force microscopy (AFM) [169]. On a cautionary note here, this thesis presented some AFM images of surfaces that appeared phase segregated via AFM, but ultimately X-PEEM analysis revealed them to be incompletely separated (ie. PS-PLA 40:60, unannealed, 0.7 wt% - see chapter 3). Lectin adsorption to the surface was found to be highly selective for the PS region, as analyzed by fluorescence microscopy. However, for this system, some HSA must be

adsorbed to PEO since firstly, the PETA concentration is in excess of 10% and must be surface enriched. In fact, these same authors previously found their PETA crosslinked pure PEO surfaces to show some protein adsorption [123] and secondly, the fluorescence intensity on the PEO regions was not completely zero.

Thus, by fabricating a completely phase segregated PS-PEO surface, likely by using lower molecular weight polymers, X-PEEM can be used to verify the above fluorescence study to examine if the use of 10% PETA crosslinker results in detectable protein adsorption, or if lower concentrations of PETA is required to obtain selective adsorption of HSA to PS only.

8.2.2 Engineering biological reactions

The PS/PMMA-PAA surface was chosen as a blend system not only to examine electrostatic interactions, but also because the carboxylate groups of PAA are free to undergo further chemical reactions such as peptide bond formation with any amine. We attempted to graft the FDA approved biopolymer chitosan, commonly found in the shell of crustaceans, to the PS/PMMA-PAA surface under aqueous conditions in the presence of *N*,*N*′-Diisopropylcarbodiimide, the peptide bond coupling agent.

Figure 8.1 shows the X-PEEM component maps obtained for the chitosan-grafted surface. For the color composite, PS is color coded as red, PMMA-PAA is color coded as green and chitosan is color coded as blue. From the qualitative analysis, the intense blue color corresponding to the chitosan polymer is localized along the interface between PS and PMMA-PAA domains. The quantitative analysis shows 0.0(5) nm, 0.3(5) nm and

0.6(5) nm of chitosan on the PS-rich, PMMA-PAA-rich and interface-rich regions, respectively.

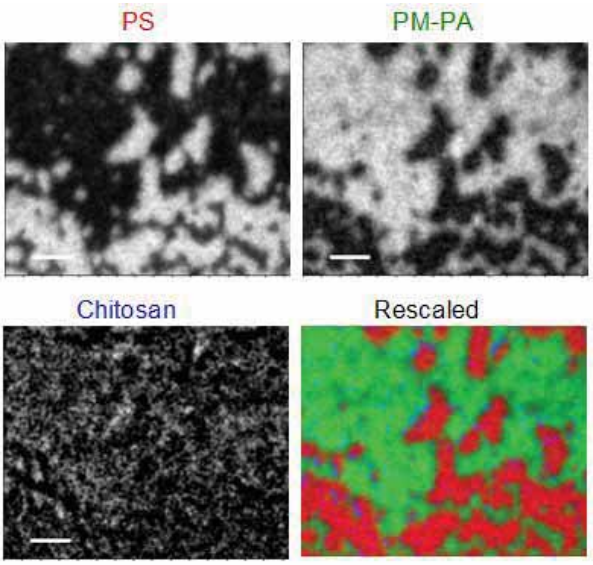

Figure 8.1: Composite maps for PS, PMMA-PAA and chitosan for a chitosan grafted PS/PMMA-PAA surface. PS is color coded as red, PMMA-PAA is color coded as green and chitosan is color coded as blue.

The first concern that arises is whether the detected chitosan is grafted or simply adsorbed to the surface. One method for verifying covalent bonding between PAA and chitosan is to dissolve the thin film into a cosolvent and run a MALDI-MS experiment to check if molecules with the combined molecular weight of PAA and chitosan are present. However, this experiment is complicated by the fact that both PAA and chitosan are polymers and have many free reactive groups that can bind more than one polymer chain. Furthermore, the PMMA groups in the PMAA-PAA domains are unreactive.

To solve this problem, blends of PS with PAA are proposed. PAA is a hydrophilic polymer that dissolves upon contact with aqueous solution, however, the PETA crosslinker can also be used to lightly crosslink PAA [170]. If a blend surface of phase

segregated PS and PAA can be obtained, any molecule with a free amine can be grafted to the surface which would enable surfaces for specific biological reactions.

Specifically, many researchers are incorporating drugs or peptides to the surface of biomaterials to speed the healing process after implantation. The RGD (arginine–glycine–aspartic acid) peptide was investigated as a coating for titanium implants to stimulate cell growth in 2005 by Bellis et al [171]. They found that the RGD peptide and adsorbed serum proteins interactively regulated cell behavior.

Thus, one could probe the interaction of RGD peptide with HSA protein by synthesizing a 10-amino acid peptide of RRRRRRRRGD, which could be easily done with an automatic peptide sequencer. This peptide will be easily recognized by NEXAFS spectroscopy via a characteristic transition at 289 eV arising from the arginine amino acid. Once grafted to the PS-PAA phase segregated surface, HSA interactions with the peptide can be probed by X-PEEM.

8.2.3 Controlled patterning

While this thesis currently focuses on randomly patterned surfaces, new lithographic techniques are emerging for the formation of well-defined patterns for applications in microarray and nanofluidics technology. Furthermore, a central goal for developing next generation biomaterials is to attach well-defined, biomolecule recognition sites to surfaces. The hypothesis is that the presence of properly designed surface recognition sites will actively induce normal healing of biomaterials in the body. X-PEEM would provide superior spatial and chemical characterization of regularly

patterned surfaces. To make these substrates, two types of patterning are proposed: ion beam patterning and photolithography.

8.2.3.1 TOF-SIMS lithographic patterning

Prof. David Castner's research group at the University in Washington in Seattle, US, has developed a lithographic patterning system using an ion beam from a time of flight secondary ion mass spectrometry system (TOF-SIMS). Firstly, a self assembled monolayer is adsorbed onto a gold surface. Next, the ion beam is used to damage a pattern onto the monolayer. When the surface is exposed to a different type of thiol, the damaged areas are replaced by the new thiol, forming a patterned surface.

As a model system, an ion beam was used to remove a benzene ring pattern from a C12 alkane SAM which was then backfilled with azobenzene. Using X-PEEM, the surface was characterized. Figure 8.2 shows the component maps of azobenzene and C12 alkane SAMs with the color composite showing the pattern with azobenzene color coded in red and the C12 alkane color coded as green.

While this shows the capability to pattern with ion beams, the azobenzene-C12 alkane system is not biologically relevant. The Castner group is currently developing a C11 alcohol terminated SAM, which is protein resistant at low protein concentrations, patterned with an array of circles via the ion beam and backfilled with a C12 carboxlyate SAM, which should attract the positively charged residues of a peptide molecule. We are interested specifically in the LKα14 peptide, which forms a perfect α-helix. Preliminary

TOF-SIMS analysis suggests that these peptides adsorb end-on on the carboxylate-terminated SAM.

Two X-PEEM experiments are envisaged: (1) investigate if the LKα14 peptide adsorbs selectively to the carboxlyate-terminated SAM, and (2) gain insight into the orientation of the peptide by probing the N 1s → π* transition of the peptide bond. Previously, NEXAFS spectroscopy showed that oriented RNA molecules self assembled to a silver surface revealed an 18% polarization dependence at the N 1s edge that was not observed for randomly oriented RNA molecules [172]. Thus, one could probe the orientation of LKα14 peptide on a SAM surface at an undulator-based X-PEEM microscope such as PEEM-3 at the ALS or the Elmitec PEEM (CaPeRs) at the CLS, where the polarization of the X-ray beam can be varied from -90° to +90°.

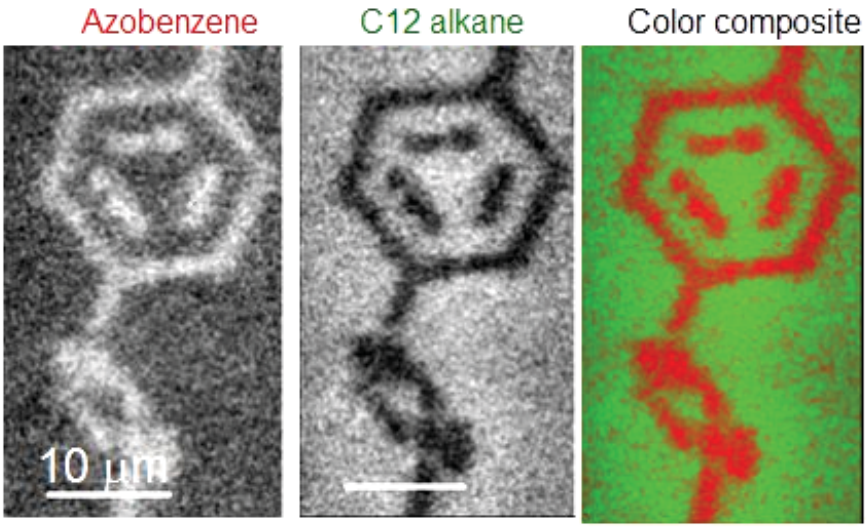

Figure 8.2: Composite maps for an ion beam patterned azobenzene and C12 alkane self assembled monolayer (SAM) surface. Azobenzene is color coded as red, C12 alkane is color coded as green.

8.2.3.2 Photolithography

The photolytic reaction of thiols with alkenes in the presence of an initiator has been cited as a promising, outstandingly efficient "click" reaction (ie. thiol-ene click chemistry) [173]. Moreover, these reactions can be carried out in the presence of oxygen under solvent-free conditions. Cysteamine is the simplest amine-thiol, although in principle, any protected cysteine terminated peptide could also be coupled to the surface (Figure 8.3).

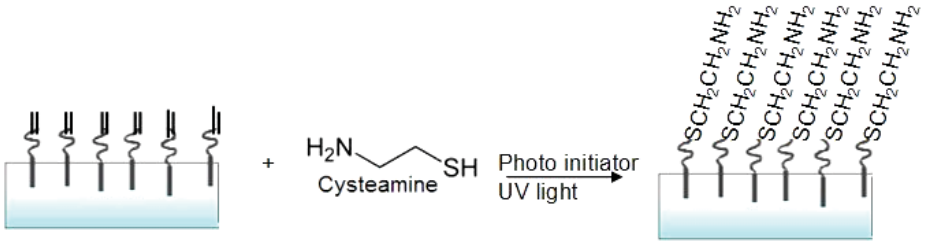

Figure 8.3: Proposed thio-lene click reaction between 1,2 polybutadiene and cysteamine.

The thiol-ene click reaction holds potential as a novel method for patterning a variety of molecules to a surface using a photoresist, with a simple patterning device being a TEM grid. One test sample would be to spin coat a solution of 1,2-polybutadiene and photoinitiator onto Si(111) followed by spin coating a film of cysteine to the surface. Next a TEM grid would be placed on top of the silicon and then UV irradiated. Theoretically, only areas that are exposed to UV light should form covalent bonds. Next, the silicon chip is sonicated in water to remove the free cysteine molecules. If this reaction works, then the surface can be functionalized with two different thiols by reacting a second thiol (thiol B) to the free double bonds that were originally protected by the photoresist (Figure 8.4).

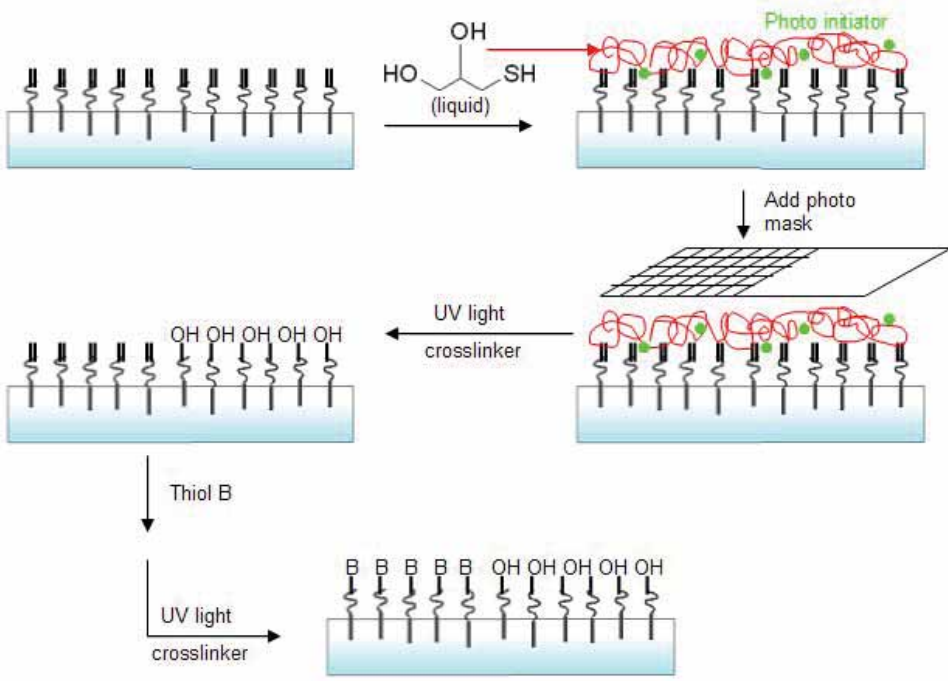

Figure 8.4: UV photolithography. 1,2 polybutadiene is exposed to thioglycerol and a photoinitiator. The surface is covered by a mask and exposed to UV light. The free thioglycerol is removed and a second thiol (B) is spun cast to the surface and exposed to UV light. Following washing, the surface is patterned by two different thiols.

8.2.4 Imaging single protein molecules with PEEM-3

While quantitative analyses of protein adsorption remains an important area of biomaterials research, studies have ascertained that the conformation of the adsorbed protein plays a vital role in the subsequent cellular processes leading to a foreign body response. Thus, techniques capable of interrogating single proteins offer significant advances for understanding the bio-fouling of a material. Although several types of microscopy (ie. TEM, SEM, AFM) have outstanding spatial resolution capable of imaging single proteins, they lack the chemical and potential conformational information obtained with NEXAFS spectroscopy. Currently, PEEM-2 has a spatial resolution of ~ 80 nm and

results show that patches of protein at a sub-monolayer coverage level are easily visible. However, when the aberration compensation optics is installed on the PEEM-3 system at the ALS (expected within the next few years), a 10-fold improvement in sensitivity and spatial resolution (below 10 nm) is predicted. If this is acheived it will easily allow for the detection of a single protein. For example, among the proteins used in our studies in the past, the blood-clotting protein fibrinogen (Fg) has dimensions of 46 x 14 nm and would be easily imaged.

8.2.5 Long range blue sky proposals

8.2.5.1 Stem cells and biomaterials

In 1998, Hench stated a message for the next millennium: "We need to shift the emphasis of biomaterials research towards assisting or enhancing the body's own reparative capacity. A working hypothesis should be 'Long-term survivability of [a] prosthesis will be increased by the use of biomaterials that enhance the regeneration of natural tissues [174].'"

Certainly, stem cells are projected to play a key role in realizing Hench's message. In adults, stem cells function as a repair system, forming specialized cells when needed. However, current research is still hampered by the inability to find reproducible conditions that can maintain the pluripotency (ability to differentiate into any cell) of human stem cells [175]. Nonetheless, it can be easily imagined that when the optimal conditions for sustaining stem cell pluripotency are found, biomaterials grafted with

functioning stem cells may easily enhance the healing process by regenerating damaged cells.

While nano-analytical studies of the materials incorporating stem cells will need to be optimized before applications in medicine, it is proposed here that soft X-ray spectromicroscopy may be able to play a role in characterizing the conditions that allow for tissue healing. One would study this by removing pluripotent stem cells grown on a model biomaterial and then analyzing the biomaterial for secreted biocomponents such as proteins, peptides, DNA, or carbohydrates.

8.2.5.2 Personalized medicine

Currently, many researchers are developing biomaterials that incorporate drugs or growth factors that can speed the healing process. For example, hyaluronic acid-based hydrogels were created as a novel biomaterial with imbedded anti-bacterial and anti-inflammatory therapeutics [176]. However, some disadvantages included obtaining predictable controlled drug release, poor encapsulation or drug instability.

However, if these challenges can be overcome then biomaterials would be a vehicle for personalized medicine. Personalized medicine is defined as the idealized medical practice of giving patients the right drugs in the right amounts at the right times [177]. Indeed, the drug dosage amount must be determined by considering each patient's drug metabolic enzymes and transporters [177]. The major advantage of personalized medicine is optimized treatment for a particular disease (or even wound healing) for a particular person.

While currently personalized medicine is being widely pursued at the genomics and proteomics level, X-ray spectromicroscopy would certainly be useful later on in the biomaterials development for characterizing the drug encapsulation material and drug release, or even possibly drug-protein interactions.

In summary, the capabilities of soft X-ray spectromicroscopy are diverse, and will likely find many more biologically relevant applications for study in the near future.

References

[1] Williams, D. F. *Progress in Biomedical Engineering: Definitions in Biomaterials.* Elsevier: Amsterdam, **1987**.

[2] Castner, D. G., Ratner, B. D. *Surface Science* **2002**, *500*, 28 – 60.

[3] Ratner, B. D., Hoffman, A. S., Schoen, F. J., Lemons, J. E., editors. *Biomaterials science: an introduction to materials in medicine*. San Diego: Academic Press, **1996**.

[4] Scott, M. *Nat News*. **1983**, *20*, 15-7.

[5] Bobbio, A., *Bull. Hist. Dent*. **1972**, *20*, 1-6.

[6] Crubezy, E., Murail, P., Girard, L., Bernadou, J.-P. *Nature*, **1998**, *391*, 29.

[7] Apple, D. J.. *Sir Harold Ridley and his fight for sight: he changed the world so that we may better see it.* Slack Inc: Thorofare, NJ, **2006**.

[8] Williams, D. *Med. Device Technol*. **2003**, *14*, 10-13.

[9] Malmsten, M. *Biopolymers at Interfaces*, 2nd Edn., Marcel Dekker: New York, **2003**.

[10] Tanford, C. *The Hydrophobic Effect: Formation of Micelles and Biological Membranes*. Wiley-Interscience: New York, **1973**.

[11] Narten, A. H., Danford, M. D., Levy, H. A. *Discuss. Faraday Soc*. **1967**, *43*, 97.

[12] Vermeer, A. W. P., Giacomelli, C. E., Norde W. *Biochimica et Biophysica Acta* **2001**, 1526, 61 – 69.

[13] Tilton, R. D., Robertson, C. R., Gast, A. P. *Langmuir*, **1991**, *7*, 2710 – 2718.

[14] Kirby, B. J., Hasselbrink, E. F. Jr. *Electrophoresis* **2004**, *25*, 203–213.

[15] Makino, K., Ohshima, H., Kondo, T. Journal of Microencapsulation, 1986, 3, 203 – 212.

[16] Van Dulm, P., Norde, W., Lyklema, J. *J. Colloid Interface Sci*. **1981**, *82*, 77 – 82.

[17] Norde, W., Lyklema, J. *J. Biomater. Sci. Polymer Edn.* **1991**, *2*, 183 – 202.

[18] Blomberg, E., Claesson, P. M., Tilton, R. D. *J. Colloid Interface Sci*. **1994**, *166*, 427 – 436.

[19] Roth, C. M., Neal, B. L., Lenhoff, A. M. *Biophysical Journal*, **1996**, *70*, 977-987.

[20] Putnam, F. W. *The Plasma Proteins*, Academic Press: London, **1960**, *Vol. I*.

[21] Peters, T. Jr. *All About Albumin: Biochemistry, Genetics, and Medical Applications*, Academic Press: New York, **1995**.

[22] He, X. M., Carter, C. D. *Nature*, **1992**, *358*, 209-215

[23] Dockal, M., Carter, D. C., Ruker, F. *J. Biological Chem.* **2000**, *275*, 3042 – 3050.

[24] Sugio, S., Kashima, A., Mochizuki, S., Noda, M., Kobayashi, K. *Protein Eng.* **1999**, *12*, 439-446.

[25] Hughes, W. L. *The Proteins*; Neurath, H., Biley, K., Eds. Academic Press: New York, **1954**, Vol. 2b, pp 663-755.

[26] Squire, P. G., Moser, P., O'Konski, C. T. *Biochemistry* **1968**, *7*, 4261-4272.

[27] Wright, A. K., Thompson, M. R. *Biophys. J.* **1975**, *15*, 137-141.

[28] Bloomfield, V. *Biochemistry* **1966**, *5*, 684-689.

[29] Ferrer, M. L., Duchowicz, R., Carrasco, B., Torre, J. G., Acuna, A. U. *Biophys. J.* **2001**, 80, 2422-2430.

[30] Foster, J. F. *Albumin Structure, Function and Uses*. Eds. V. M. Rosenoer, M. Oratz, M. A. Rothschild; Pergamon: Oxford, **1977**, 53-84.

[31] Qui, W., Zhang, L., Okobiah, O., Yang, Y., Wang, L., Zhong, D. *J. Phys. Chem. B.* **2006**, *110*, 10540 – 10549.

[32] Chittur, K. K. B*iomaterials* **1998**, *19*, 357 – 369.

[33] Green, R. J., Frazier, R. A., Shakesheff, K. M., Davies, M. C. , Roberts, C. J., Tendler, S. J. B. *Biomaterials* **2000**, *21*, 1823 – 1835.

[34] Sigal, G. B., Mrksich, M., Whitesides, G. M. *J. Am. Chem. Soc*. **1998**, *120*, 3464 – 3473.

[35] Hook, F., Kasemo, B., Nylander, T., Fant, C., Sott, K., Elwing, H. *Anal. Chem*. **2001**, *73*, 5796 – 5804.

[36] Elwing, H. *Biomaterials* **1998**, *19*, 397 – 406.

[37] Hook, F., Rodahl, M., Brzezinski, P., Kasemo, B. *Langmuir* **1998**, *14*, 729 – 734.

[38] Archambault, J. G., Brash, J. L. *Colloids Surf B: Biointerfaces* **2004**, *33*, 111 – 120.

[39] Siedlecki, C. A., Marchant, R. E. *Biomaterials* **1998**, *19*, 441 – 454.

[40] Sousa, A., Sengonul, M., Latour, R., Kohn, J., Libera, M. *Langmuir* **2006**, *22*, 6286 – 6292.

[41] Varesi, J., Majumdar, A. *Appl. Phys. Lett*. **1998**, *72*, 37-39.

[42] Sanchez, E. J., Novotny, L., Xie, X. S. *Phys. Rev. Lett*. **1999**, *82*, 4014–4017

[43] Amos, W. G., White, J. G. *Biology of the Cell*, **2003**, *95*, 335–342.

[44] Pattnaik, P., *Applied Biochemistry and Biotechnology*, **2005**, *126*, 79 – 92.

[45] Scheinfein, M. R., Unguris, J., Kelley, M. H., Pierce, D. T., Celotta, R. J. *Rev. Sci. Instrum*. **1990**, *61*, 2501 – 2527.

[46] Nygren, H., Malmberg, P., Kriegeskotte, C., Arlinghaus, H.F. *FEBS Letters*, **2004**, *566*, 291–293.

[47] Kondo, H., Tomie, T., Shimizu, H. *Appl. Phys. Lett*. **1998**, *72*, 2668 – 2670.

[48] Bauer, E. *J. Electron Spectrosc. Relat. Phenom.* **2001**, *114-116*, 975.

[49] Bauer, E. *J. Phys. Condens. Matter* **2001**, *13*, 11391.

[50] Ade, H., Hitchcock, A.P. *Polymer* **2008**, *49* 643-675

[51] Kirz, J., Jacobson, C., Howells, M. Q. *Rev. Biophys.* **1995**, *28*, 33.

[52] Ade, H. in *Experimental Methods in the Physical Sciences.* Eds J. A. R. Samson, D. L. Ederer. Academic Press: San Diego, CA, **1998**, Vol. 32, 225.

[53] Urquhart, S. G., Ade, H. *Chemical Applications of Synchrotron Radiation.* Ed. T. K. Sham. World Scientific: Singapore, **2002**, 285.

[54] Morin, C. M. Ph.D Thesis, McMaster University, Department of Chemistry, 2004.

[55] Li, L. Ph.D Thesis, McMaster University, Department of Chemistry, 2006.

[56] Campbell, I. M. *Introduction to synthetic polymers*, Oxford University Press: New York, **1994**.

[57] Wu, S. *Phys. Chem*. **1970**, *74*, 632-638.

[58] Morin, C., Ikeura-Sekiguchi, H., Tyliszczak, T., Cornelius, R., Brash, J. L., Hitchcock, A. P., Scholl, A., Nolting, F., Appel, G., Winesett, D. A., Kaznacheyev, K., Ade. H. *J. Electron Spec.* **2001**, *121*, 203-224.

[59] Li, L., Hitchcock, A. P., Cornelius, R., Brash, J. L., Scholl, A., Doran. A. *J. Phys. Chem. B* **2008**, *112*, 2150 – 2158.

[60] Morin, C., Hitchcock, A. P., Cornelius, R. M., Brash, J. L., Scholl, A., Doran, A. *J. Electron Spectroscopy*, **2004,** *137-140*, 785-794.

[61] L. Li, A. P. Hitchcock, N. Robar, R. Cornelius, J. L. Brash, A. Scholl, A. Doran. *J. Phys. Chem. B* **2006**, *110*, 16763 – 16773.

[62] Gros, G., Forster, R. E., Lin, L. *J. Biol. Chem.* **1976**, *251*, 4398-4407.

[63] Liu, Y., Messmer, M. C. *J. Phys. Chem. B* **2003**, *107*, 9774 – 9779.

[64] Winick, H. *Synchrotron Radiation Sources, A primer*. World Scientific: New Jersey, **1994**, Ch 1.

[65] Winick, H. *X-ray Data Booklet, Section 2.3: Operating and planned facilities*. Retrieved February 21, **2010**, from http://xdb.lbl.gov/Section2/Sec_2-3.html.

[66] The Advanced Light Source. Retrieved March 2010 from http://www.lbl.gov/MicroWorlds/ALSTool/

[67] *RF Systems*. Retrieved February 21, **2010** from http://www.lbl.gov/MicroWorlds/ALSTool/ALS_Components/RFSystem/

[68] Winick, H., Doniach, S. *Synchrotron Radiation Research*. Plenum Press: New York, **1980**, 1 – 58.

[69] ESRF, GILDA beamline. Retreived February 21, **2010** from http://www.esrf.fr/exp_facilities/BM8/handbook/BM8.html

[70] Farrel W., Lytle *J. Synchrotron Rad*. **1999**, *6*, 123-134

[71] Rehr, J. J., Albers, R. C. *Rev. Mod. Phys*. **2000**, *72*, 621 – 654.

[72] Stern, E. A. *X-ray absorption : principles, applications, techniques of EXAFS, SEXAFS, and XANES.* Ed. Koningsberger, D. C., Prins, R. Wiley: New York, **1988**, Ch.1.

[73] Stohr, J. *NEXAFS Spectroscopy*, Springer: Santa Clara, **1996**.

[74] CXRO database. Retrieved March 1, 2010 from http://www-cxro.lbl.gov/

[75] Wang, J., Morin, C., Li, L., Hitchcock, a. P., Zhang, X., Araki, T., Doran A., Scholl, A. *J. Electron Spectrosc. Rel. Phenom.*, **2009**, *170*, 25-36.

[76] Frazer, B.H., Gilbert, B., Sonderegger, B.R., De Stasio, G. *Surf. Sci.* **2003**, *537*, 161.

[77] Urquhart S.G., Ade H. *J Phys Chem B* **2002**, *106*, 8531.

[78] J. Kikuma, B. P. Tonner, *J. Electron Spectrosc. Rel. Phenom.*, **1996**, *82*, 53-60.

[79] C. M. Schneider. *Neutron and X-ray Spectroscopy*. Eds Hippert, F., Geissler, E., Hodeau, J. L., Lelièvre-Berna, E., Regnard, J. R. Springer: Netherlands, **2006**.

[80] Photoemission electron microscope for the study of magnetic materials. Retrieved March 1, 2010 from http://www.als.lbl.gov/als/compendium/AbstractManager/uploads/anders3.pdf

[81] Anders, S., Padmore, H. A., Duarte, R. M., Renner, T., Stammler, T., Scholl, A., Scheinfeld, M. R., Stöhr, J., Seve, L., and Sinkovic, B. *Rev. Sci. Instrum*. **1999**, *70*, 3973.

[82] Suez, I., Rolandi, M., Backer, S. A., Scholl, A., Doran, A., Okawa, D., Zettl, A., Frechet, J. M. M. *Adv. Mater*. **2007**, *19*, 3570-3573.

[83] aXis2000 is free for non-commercial use. It is written in Interactive Data Language (IDL) and available from http://unicorn.mcmaster.ca/aXis2000.html

[84] Drelich, J., and Mittal, K. L. *Atomic Force Microscopy in Adhesion Studies*. Extenza Turpin: Utrecht, 2005, 1-20.

[85] Chard, T. *Laboratory Techniques in Biochemistry and Molecular Biology. An Introduction to radioimmunoassay and related techniques.* V30, part 2. Elsevier: New York. **1987**, 40-67.

[86] The Radiation Hazards of ^{125}I and ^{131}I. Retrieved March 1, 2010 from *www.gla.ac.uk/services/radiationprotection/iodineinfo.doc*.

[87] Anfinsen, C. B., Edsall, J. T., Richards, F. M. *Advances in protein chemistry*, Volume 30, Academic Press: New York, **1995**.

[88] Jahangir, A. The Importance of Protein Adsorption in the Blood Compatibility and Biostability Evaluation of Poly Etherurethanes (PEU)s Containing Surface Modifying Macromolecules (SMMs). A thesis submitted to the University of Toronto, Department of Biomedical Engineering. **1999**.

[89] Merrill, E. W., Dennison, K. A., Sung, C. *Biomaterials* **1993**, *14*, 1117-1126.

[90] Quinn, C. P., Patha, C. P., Heller, A., Hubbell, J. A. *Biomaterials*, **1995**, *16*, 389-396.

[91] Kjellander, R., Florin, E. *J. Chem. Soc. Faraday Trans I*, **1981**, *77*, 2023.

[92] Andrade, J. (Ed.) *Surface and Interfacie Aspects of Biomedical Polymers*. Ch 1, Plenum: New York, **1985**.

[93] Klein, J., Luckham, P. *Nature*, **1982**, *300*, 429.

[94] Luckham, P., Klein, J. *Macromolecues* **1985**, *18*, 721.

[95] Leon, S. I., Lee, J. H., Andrade, J. D., de Gennes, P. G. *J. Colloid and Interface Science*, **1991**, *142*,149-158.

[96] Unsworth, L. D., Tun, Z., Sheardown, H., Brash, J. L. *J. Colloid and Interface Sci* **2006**, 296, 520-526.

[97] Malmsten, M., Emoto, K., Van Alstine, J. M. *J. Colloid Interface Sci*. **1998**, *202*, 507-517.

[98] Tosatti, S., De Paul, S. M., Askendal, A., Vandevondele, S., Hubbell, J. A., Tengvall, P., Textor, M. *Biomaterials* **200,** *24*, 4949-4958.

[99] Vogler, E. A. *J. Biomater. Sci., Polym. Ed.* **1999**, *10*, 1015.

[100] Stringer, J. L., Peppas, N. A. *Journal of Controlled Release* **1996**, *42*, 195-202.

[101] Doycheva, M., Stamenova, R., Zvetkov, V., Tsvetanov, C. B. *Polymer*, **1998**, *39*, 6715-6721.

[102] Mellott, M. B., Searcy, K., Pishko, M. V. *Biomaterials* **2001**, *22*, 929-941.

[103] Kofinas, P., Athanassiou, V., Merrill, E. W. *Biomaterials* **1996**, *17*, 1547 – 1550.

[104] Doytcheva, M., Dotcheva, D., Stamenova, R., Orahovats, A., Tsvetanov, C. H., Leder, J. *Journal of Applied Polymer Science* **1998**, *64*, 2299 – 2307.

[105] Doycheva, M., Petrova, E., Stamenova, R., Tsvetanov, C., Riess, G. *Macromol. Mater. Eng*. **2004**, *289*, 676-680.

[106] Doytcheva, M., Dotcheva, D., Stamenova, R., Tsvetanov, C. *Macrmol. Mater. Eng.* **2001**, *286*, 30-33.

[107] Dimitrov, M., Dotcheva, D., Lambov, N. *Acta Pharmaceutica Turcica* **2004**, *46*, 49-54.

[108] Petrov, P., Bozukov, M., Burkhardt, M., Muthukrishnan, S., Müller A. H. E., and Tsvetanov, C. B. *J. Mater. Chem.*, **2006**, *16*, 2192 – 2199.

[109] Lensen, M. C., Mela, P., Mourran, A., Groll, J., Heuts, J., Rong, H., and Möller, M. *Langmuir* **2007,** *23*, 7841-7846.

[110] Leung, B. O., Hitchcock, A. P., Cornelius, R. M., Brash, J. L., Scholl, A., Doran, A. *Biomacromol.* **2009**, *10*, 1838-1845.

[111] Leung, B. O., Hitchcock, A. P., Brash, J. L., Scholl, A., Doran, A., Henklein, P., Overhage, J., Hilpert, K., Hale, J. D., Hancock, R. E. W. *Biointerphases* **2008**, *3*, F27-F35.

[112] Leung, B. O., Hitchcock, A. P., Brash, J. L., Scholl, A., Doran, A. *Macromol.* **2009,** *42*, 1679 – 1684.

[113] Warwick, T., Ade, H., Kilcoyne, A. L. D., Kritscher, M., Tylisczcak, T., Fakra, S., Hitchcock, A. P., Hitchcock, P., Padmore, H. A. *J. Synch. Rad.* **2002,** *9*, 254.

[114] Kilcoyne, A. L. D., Tylisczak, T., Steele, W. F., Fakra, S., Hitchcock, P., Franck, K., Anderson, E., Harteneck, B., Rightor, E. G., Mitchell, G. E., Hitchcock, A. P., Yang, L., Warwick, T., Ade, H. *J. Synch. Rad.* **2003,** *10*, 125.

[115] Jacobsen, C. J., Zimba, C., Flynn, G., Wirick, S. *J. Microscopy* **2000,** *19***,** 173-184.

[116] Strang, G. *Linear Algebra and Its Applications*. Harcourt Bracourt, Jovanovich: San Diego, **1988**.

[117] Koprinarov, I. N., Hitchcock, A. P., McCrory, C. T., Childs, R. F. *J. Phys. Chem. B* **2002,** *106*, 5358-5364.

[118] Petrov, P., Bozukov, M. and Tsvetanov, C. B. *J. Mater. Chem*., **2005**, *15*, 1481.

[119] Ton-That, C., Shard, A. G., Teare, D. O. H., Bradley, R. H. *Polymer* **2001**, *42*, 1121-1129

[120] Lim, S. C., Kim, S. H., Lee, J. H., Kim, M. K., Kim, D. J., Zyung, T. *Synthetic Metals* **2005**, *148*, 75–79**.**

[121] Russel, T. P. *Science*, **2002**, *297*, 964-967.

[122] Schaub, T. F., Kellogg, G. J., Mayes, A. M., Kulasekere, R., Ankner, J. F., and Kaiser, H. *Macromolecules* **1996**, *29,* 3982-3990

[123] Zemla, J., Lekka, M., Wiltowska-Zuber, J., Budkowski, A., Rysz, J., Raczkowska, J. *Langmuir*, **2008**, *24*, 10243-10258.

[124] Kingshott, P.; Griesser, H. J. *Current Opionion in Solid State and Materials Science* **1999**, *4*, 403-412.

[125] Wedler, F. C.; Riedhammer, T. M. *Biocompatibility in Clinical Practice* **1982**, *11*, 1-12.

[126] Park, J. H.; Park, K. D.; Bae, Y. H. *Biomaterials* **1999**, *20*, 943.

[127] Bergstrom, K.; Holmberg, K.; Safranj, A.; Hoffman, A. S. *J. Biomed. Mater. Res*. **1992**, *26*, 779.

[128] Prime, K. L.; Whitesides, G. M. *Science* **1991**, *252*, 1164-1167.

[129] Park, J. Y.; Acar, M. H.; Akthakul, A.; Kuhlman, W.; Mayes, A. M.; *Biomaterials* **2006**, *27*, 856–865

[130] Yang, Z., Galloway, J. A., Yu, H. *Langmuir*, **1999**, 15, 8405–8411.

[131] Lee, J. H., Lee, H. B., Andrade, J. D. *Prog. Polym. Sci.* **1995**, *20*, 1043-1079.

[132] Ahmed, F., Discher, D. E. *Journal of Controlled Release* **2004**, *96*, 37-53.

[133] Matthews, J. A., Simpson, D. G., Wnek, G. E., Bowlin G. L. *Biomacromolecules* **2002**, *3*, 232-238.

[134] Jin, H. J., Fridrikh, S. V., Rutledge, G. C., Kaplan, D. L. *Biomacromolecules* **2002,** *3, 1233-1239.*

[135] Christie, R. J., Findley, D. J., Dunfee, M., Hansen, R. D., Olsen, S.C., Grainger, D. W. *Vaccine*, **2006**, *24*, 1462 – 1469.

[136] Grainger, D., Okano, T., Kim, S. W. *Advances in Biomedical Polymers*. Ed. Gebelein, C. G. Plenum Publishing Corporation. **1987**.

[137] Grainger, D. W., Okano, T., Kim, S. W. J. Colloid Int. Sci. **1989**, *132*, 161 – 175.

[138] George, P. A., Donose, B. C., Cooper-White, J. J. *Biomaterials* **2009**, *30*, 2449-2456.

[139] Wang, P., and Koberstein, J. T. *Macromolecules* **2004,** *37,* 5671-5681

[140] Walheim, S., Ramstein, M., and Steiner, U. *Langmuir* **1999,** *15,* 4828-4836

[141] Virgilio, N., Favis, B. D., Pepin, M.-F., Desjardins, P., L'Esperance, G. *Macromolecules* **2005,** *38,* 2368-2375

[142] Miles, I. S., Zurek, A. *Polymer* **1988**, *28*, 796-805.

[143] Ton-That, C., Shard, A. G., Daley, R., Bradley, R. H. *Macromolecules* **2000,** *33*, 8453-8459

[144] Nishio, Y., Hirose, N., Takahashi, T. *Polymer Journal*, **1989**, *21*, 347 – 351.

[145] Davies, M. C., Shakesheff, K. M., Shard, A. G., Domb, A., Roberts, C. J., Tendler, S. J. B., Williams, P. M. *Macromolecules* **1996**, *29*, 2205-2212.

[146] Guo, S., Shen, L., Feng, L. *Polymer* **2001**, *42*, 1017-1022.

[147] Thomas, H. R., O'Malley, J. J. *Macromolecules* **1979**, *12*, 323-329.

[148] O'Malley, J. J., Thomas, H. R., Lee, G. M. *Macromolecules* **1979**, *12*, 996-1001.

[149] Amiji, M. M. *Biomaterials* **1995**, *16*, 593-599.

[150] Leung, B. O., Hitchcock, A. P., Brash, J. L., Scholl, A., Doran, A. *Advanced Biomaterials* **2010** *in press*.

[151] Lucker, A.; Teβmar, J.; Schnell, E.; Schmeer, G.; Gopferich, A. *Biomaterials* **2000**, *21*, 2361-2370.

[152] Anderson, J. M., Rodriguez, A., Chang, D. T. *Seminars in Immunology*, **2008**, *20*, 86-100.

[153] Veiseh, M., Zareie, M. H., Zhang, M. *Langmuir* **2002,** *18*, 6671-6678

[154] Frey, B. L., Jordan, C. E., Komguth, S., Com, R. M. *Anal Chem*. **1995**, *67*, 4452 – 4457.

[155] Roach, L. S., Song, H., Ismagilov, R. F. *Anal. Chem*. **2005,** *77*, 785-796

[156] Wadu-Mesthrige, K., Xu, S., Amro, N. A., Liu, G.-Y. *Langmuir* **1999,** *15*, 8580-8583

[157] Rezwan, K., Meier, L. P., Gauckler, L. J. *Biomaterials* **2005**, *26*, 4351–4357.

[158] Haynes, C. A., Norde, W. *Colloids Surf., B* **1994**, *2*, 517-603.

[159] Ta, T. C., McDermott. M. T. *Anal Chem.* **2000**, *72*, 2627 – 2634.

[160] Stewart-Ornstein, J., Hitchcock, A. P., Hernàndez-Cruz, D., Henklein, P., Overhage, J., Hilpert, K., Hale, J., Hancock, R. E. W. *J. Phys. Chem. B* **2007**, 111, 7691-7699.

[161] Pashe, S., Voros, J., Griesser, H. J., Spencer, N. D., Textor, M. *J. Phys. Chem. B*. **2005**, *109*, 17545 – 17552.

[162] Arai, T., Norde, W. *Colloids Surf.* **1990**, *51*, 1-15.

[163] Fogh-Andersen, N., Bjerrum, P. J., Siggaard-Andersen, O. *Clinical Chemistry*, **1993**, *39*, 48-52.

[164] Garret, Q., Milthorpe, B. K. *Investigative Ophthalmology & Visual Science*, **1996**, *37*, 2594-2602

[165] Gachon A.M., Bilbaut T, Dastugue B. *Exp Eye Res.***1985**, *40*, 105-116.

[166] Norde W, Favier J.P. *Colloids and Surfaces.* **1992**, *64*, 87-93.

[167] Lee, S.H., Ruckenstein, E. *Colloid InterfaceSci.* **1988**, *125*, 365-379

[168] Park, H., Robinson, J. R. *Pharmaceutical Research*, **1987**, *4*, 457-464.

[169] Zemla, J., Lekka, M., Raczkowska, J., Bernasik, A., Rysz, J., Budkowski, A. *Biomacromolecules* **2009**, *10*, 2101 – 2109.

[170] Thomas, J. B., Creecy, C. M., McGinty, J. W., Peppas N. A. *Polymer Bulletin*, **2006**, *57*, 11 – 20.

[171] Ferris, D. M., Moodie, G. D., Dimond, P. M., Gioranni, C. W. D., Ehrlich, M. G., Valentini, R. F. *Biomaterials* **1999**, *20*, 1999, 2323 - 2331

[172] Liu, X., Jang, C. H., Zheng, F., Jurgensen, A., Denlinger, J. D., Dickson, K. A., Raines, R. T., Abbott, N. L., Himpsel, F. J. *Langmuir* **2006,** *22*, 7719-7725

[173] Killops, K. L., Campos, L. M., Hawker, C. J. *J. Am Chem. Soc*. **2008**, *130*, 5062-5064.

[174] Hench, L. L. *Biomaterials* **1998**, *19*, 1419-1423

[175] Spradling, A., Drummond-Barbosa, D., Kai, T. *Nature*, **2001**, *414*, 98.

[176] Luo, Y., Kirker, K. R., Prestwich, G. D. J. Controlled Release 2000, 69, 169 – 184.

[177] Kaminuma, T., Nakata, K., Nakano, T., Takai-Igarashi, T. *Chem-Bio Informatics Journal*, **2001**, *1*, 1-17.